Atomistic and Multiscale Modeling of Plasticity in Irradiated Metals

A Dissertation
Presented to
The Academic Faculty

by

Sankar Narayanan

In Partial Fulfillment
of the Requirements for the Degree
Doctor of Philosophy in the
School of Mechanical Engineering

Georgia Institute of Technology
December 2014

Atomistic and Multiscale Modeling of Plasticity in Irradiated Metals

Approved by:

Dr. Ting Zhu, Advisor
School of Mechanical Engineering
Georgia Institute of Technology

Dr. Surya Kalidindi
School of Mechanical Engineering
Georgia Institute of Technology

Dr. David McDowell
School of Mechanical Engineering
Georgia Institute of Technology

Dr. Naresh Thadhani
School of Materials Science and Engineering
Georgia Institute of Technology

Dr. Chaitanya Deo
School of Mechanical Engineering
Georgia Institute of Technology

Dr. Hamid Garmestani
School of Materials Science and Engineering
Georgia Institute of Technology

Date Approved: June 4, 2014

This thesis is dedicated to my wife, Lalitha.

ACKNOWLEDGEMENTS

On the first place I would like to express my sincerest gratitude to my Ph.D thesis advisor, Dr. Ting Zhu, without whom this thesis simply would not have been possible. He gave me strong motivation, guidance and support throughout my thesis work and helped me overcome various hurdles with respect to my work. He was very patient and insightful in his mentorship and granted me the complete academic freedom to explore advanced scientific problems for research, thereby raising the standards of my thinking and output. Many a times he even got involved hands-on with my work and spent considerable time working with me to overcome logistical difficulties. Working with him has been one of the most significant and fruitful experiences in my life.

Secondly I would like to thank Dr David McDowell and Dr Chaitanya Deo, who have been our close collaborators, apart from being the members of my committee. Their suggestions and insights helped a lot and gave solid directions for my thesis work. I would want to thank the others in my Ph.D thesis committee, Dr Surya Kalidindi, Dr Naresh Thadhani and Dr Hamid Garmestani, for their valuable guidance and feedback that significantly helped enhance my work.

A portion of my work would not have been complete without the collaboration with some wonderful experimentalists and hence I would like to extend my sincere gratitude to them: Jiangwei Wang & Dr Scott X Mao (U. Pittsburg) and Dr Yong Zhu (NCSU).

TABLE OF CONTENTS

Page

ACKNOWLEDGEMENTS iv

LIST OF TABLES vii

LIST OF FIGURES viii

LIST OF SYMBOLS xii

LIST OF ABBREVIATIONS xiv

SUMMARY xv

CHAPTER

1 Introduction 1

Modeling of irradiation damage in metals 1

Necessity for a multiscale computational approach 3

Atomistically informed crystal plasticity model for BCC Iron 6

Self Interstitial atom induced hardening and softening in irradiated BCC Iron 7

Deformation induced formation of stacking fault tetrahedra under non-irradiated conditions 8

Study of interface mediated plasticity and implications for irradiation damage 8

2 Atomistically informed crystal plasticity model for BCC Iron 10

Introduction 10

Methods 13

Results 20

Discussion 38

Conclusions 42

3 Self-interstitial atom induced hardening and softening in irradiated BCC Iron 44

Introduction 44

Methods 47

Results 50

Discussion 63

Conclusions 66

4 Deformation induced formation of stacking fault tetrahedra under non-irradiated conditions 68

Introduction 68

Methods 70

Results 71

Discussion 85

Conclusions 91

5 Interface mediated plasticity and implications for irradiation damage 92

Introduction 92

Methods 95

Results and discussion 96

Conclusions 109

6 Conclusions 110

REFERENCES 113

LIST OF TABLES

Page

Table 2.1: Atomistically determined parameters for stress-dependent activation energy H and shearing rate prefactor $\dot{\gamma}_0^{\alpha}$ 33

Table 2.2: Material parameters for the crystal plasticity model 34

LIST OF FIGURES

Page

Figure 2.1: Atomistic simulation set-up 15

Figure 2.2: Differential displacement plot of the non-degenerate screw dislocation core predicted by Proville-EAM 21

Figure 2.3: Orientation dependence of the Peierls stress predicted by Proville-EAM in 2D simulations 22

Figure 2.4: 2D Peierls barriers predicted by Proville-EAM and Mendelev-EAM potentials 23

Figure 2.5: 3D NEB results of thermally activated screw dislocation motion at zero stress 24

Figure 2.6: Differential displacement plots 26

Figure 2.7: Uncorrelated kinkpair nucleation predicted by Mendelev-EAM for zero stress 27

Figure 2.8: Atomistic details of correlated kinkpair nucleation 29

Figure 2.9: Shear stress-dependent minimum energy path (MEP) and activation energy 31

Figure 2.10: Orientation dependent stress-strain behavior of BCC Fe 35

Figure 2.11: Predictions from our atomistically informed crystal plasticity model for tensile loading along the [100] orientation 36

Figure 2.12: Stress as a function of temperature for the [100] loading orientation 38

Figure 3.1: Schematics of the point defects around (a) an edge dislocation and (b) a screw dislocation 45

Figure 3.2: Atomistic simulation set-up 48

Figure 3.3: Differential displacement plots and the 3-kink dislocation structure 52

Figure 3.4: 3D NEB results of thermally activated motion of the 3-kink dislocation at 300 MPa 56

Figure 3.5: Schematics of the 3-kink dislocation motion 57

Figure 3.6: Shear stress-dependent minimum energy path (MEP) and activation energy 60

Figure 3.7: Yield stress as a function of temperature 61

Figure 3.8: 3D NEB results for the unit process of absorption of SIA into the dislocation core 64

Figure 4.1: Formation of dislocation-originated stacking fault tetrahedra (SFT) 73

Figure 4.2: Formation of dislocation-originated SFT in molecular dynamics (MD) simulation 75

Figure 4.3: Formation of a closed-SFT through the cross-slip of a trailing partial 76

Figure 4.4: Crystallographic structure of the dislocation-originated and vacancy-originated SFT 78

Figure 4.5: Migration of dislocation-originated SFT during deformation 80

Figure 4.6: Interaction of a partial dislocation with SFT and the surface step on SFT created by the interaction 81

Figure 4.7: Annihilation of dislocation-originated SFT under tensile deformation 83

Figure 4.8: Formation of multiple SFT in a larger Au nanowire 87

Figure 4.9: Stress-strain curve for an Au nanowire under uniaxial tension and the MD snapshots at various strain levels 88

Figure 4.10: Formation of SFT in MD simulation of a deformed Cu nanowire 90

Figure 5.1: Schematic showing twin-boundary engineered metallic nanowires 94

Figure 5.2: Images and results from experiments 97

Figure 5.3: Atomistic model of the five-fold twinned Ag NW 98

Figure 5.4: MD simulation results for the pristine Ag NW 99

Figure 5.5: Size-effected hardening behavior 102

Figure 5.6: Stress-strain curves 103

Figure 5.7: Deformation via multiple necking and ductile failure 106

Figure 5.8 Effect of pre-existing defects 108

LIST OF SYMBOLS

$\mathbf{F}$	Deformation gradient tensor
$\mathbf{F}^*$	Elastic deformation gradient
$\mathbf{F}_\mathrm{p}$	Plastic deformation gradient
$\mathbf{L}_\mathrm{p}$	Plastic deformation velocity gradient
$\mathbf{S}_0^\alpha$	Schmid tensor
$\mathbf{m}_0^\alpha$	Slip direction unit vector
$\mathbf{n}_0^\alpha$	Slip plane normal unit vector
$\dot{\gamma}^\alpha$	Plastic shearing rate in slip system α
b	Burgers vector
ρ	Mobile dislocation density
v^α	Dislocation velocity on slip system α
v_0	Reference dislocation velocity
H	Activation energy for unit dislocation slip
k_B	Boltzmann constant
T	Absolute temperature
τ_eff^α	Effective shear stress on slip system α
$\dot{\gamma}_0$	Reference strain rate
τ_eff^α	Effective resolved shear stress
s_a^α	Athermal slip resistance
$\mathbf{C}^*$	Right Cauchy-Green tensor
$\mathbf{T}^*$	Second Piola-Kirchhoff stress tensor
H_0	Activation energy at zero stress
p	Profiling parameter #1
q	Profiling parameter #2
s_t0	Thermal slip resistance

$q^{\alpha\beta}$	Hardening matrix
$\delta_{\alpha\beta}$	Kronecker delta
h^{β}	Self-hardening rate on slip system β
h_0	Initial self-hardening rate
$s_{\mathrm{a,s}}^{\beta}$	Saturation value of athermal slip resistance
ν_{D}	Debye frequency
l	Lateral extent of kinks at the saddle state
N	Number of atoms in a unit cell
V	Volume of a unit cell
v_s	Speed of sound
V^*	Activation volume

LIST OF ABBREVIATIONS

MD	Molecular dynamics
MC	Monte Carlo
DFT	Density functional theory
EAM	Embedded atom method
NEB	Nudged elastic band method
MEP	Minimum energy path
AFM	Atomic force microscopy
SEM	Scanning electron microscope
TEM	Transmission electron microscopy
HRTEM	High resolution transmission electron microcopy
STM	Scanning tunneling microscope
CCD	Charge-coupled device
MRSSP	Maximum resolved shear stress plane
FCC	Face-centered-cubic
BCC	Body-centered-cubic
SFT	Stacking fault tetrahedra
3D	Three-dimensional
2D	Two-dimensional
DD	Differential displacement
TB	Twin boundary
SIA	Self interstitial atom
NW	Nanowire
LAMMPS	Large-scale Atomic/Molecular Massively Parallel Simulator

SUMMARY

Irradiation induces a high concentration of defects in the structural materials of nuclear reactors, which are typically of body-centered cubic Iron (BCC Fe) and its alloys. The primary effect of irradiation is hardening which is caused by the blocking of dislocations with defects and defect clusters like point defects, self-interstitial loops, and voids. The dislocation-defect interactions are atomistic in nature due to the very small length and time scales involved, i.e., of the order of nanometers and picoseconds. To predict the effect of dislocation-defect interactions on the macroscopic mechanical and plastic behavior of the material, it is critically important to develop robust coupling schemes by which accurate atomic level physics of the rate-limiting kinetic processes can be informed into a coarse-grained model such as crystal plasticity. In this thesis we first develop an atomistically informed constitutive model. Relevant atomistic processes are identified from molecular dynamics simulations. The respective unit process studies are conducted using atomistic Nudged Elastic Band method. Stress-dependent activation energies and activation volumes are computed for various rate-liming unit processes such as thermally activated dislocation motion via kinkpair nucleation, dislocation pinning due to self interstitial atom, etc. Constitutive laws are developed based on transition state theory, that informs the atomistically determined activation parameters into a coarse-grained crystal plasticity model. The macroscopic deformation behavior predicted by the crystal plasticity model is validated with experimental results and the characteristic features explained in the light of atomistic knowledge of the constituting kinetics. The subsequent focus of this thesis is on the interaction between screw dislocations and self interstitial atoms which is supposed to be an important plasticity mechanism in irradiated

metals. Nudged elastic band method calculations are carried out to estimate the kinetics of screw dislocation-self interstitial interaction and connections are made to experimental results reporting irradiation induced hardening and softening phenomena. Following these works on irradiated BCC Iron, we investigate on unique irradiation induced defects in FCC metals such as stacking fault tetrahedra, that we discovered to be formed via dislocation interactions in gold nanocrystals under non-irradiated conditions. Our results from high resolution *in situ* TEM (HRTEM) experiments and large scale molecular dynamics simulations reveal the formation, evolution, and destruction of stacking fault tetrahedra, thus adding new knowledge to this special three-dimensional defect. Moreover, we investigate nanoscale engineered materials with internal interfaces that are capable of resisting irradiation induced damage. The mechanical behavior and work hardening exhibited by silver nanowires are studied with a specific five-fold twinned internal microstructure using tensile test experiments in SEM and large scale molecular dynamics simulations. Overall, the research presented in this thesis involves the development and implementation of novel computational paradigm that encompasses computational approaches of various length and time scales towards robust predictions of the mechanical behavior of irradiated materials.

CHAPTER 1

INTRODUCTION

1.1 Modeling of irradiation damage in metals

The significant effects of irradiation on the mechanical behavior of structural materials in nuclear reactors are primarily due to the interaction of dislocations with irradiation induced defects of various dimensionalities [1]. Irradiation induced defects mainly include zero-dimensional point defects like vacancies and self-interstitials, two dimensional defects like self-interstitial loops, and three dimensional defects like voids and stacking fault tetrahedra. The point defects are formed due to the localized shuffling of the lattice due to the incident, high energy, knock-on atoms, called the radiation cascade induced defect nucleation [2]. These point defects clusters grow to form clustered defects like self interstitial loops, voids and stacking fault tetrahedra. Voids are known to be very strong obstacles to dislocation motion [3] and can also contribute to irradiation induced swelling [4] along with gaseous atoms like that of Helium. Stacking fault tetrahedra are the primary three dimensional defects formed in face centered cubic (FCC) metals like Cu [5]. In irradiated BCC metals, self-interstitial loops are the most commonly found defects [6]. Complex dislocation networks, cavities and precipitates are also observed in irradiated metals [7]. All these defects can interact with dislocations resulting in their strong pinning onto the lattice. These microscopic pinning mechanisms manifest as irradiation induced hardening and subsequently lead to dislocation channeling and flow localization. Dislocation channels are formed due to large irradiation doses and they are essentially channels depleted of irradiation induced defects [8]. Stress induced

unpinning of dislocations from the obstacles help them to sweep through and annihilate the barriers, leading to flow softening and localized deformation along these channels.

Another important irradiation induced phenomenon is creep. Irradiation creep rates are usually higher than the thermal creep rates in virgin materials and occur at relatively lower temperatures. In contrast to thermal creep that is dictated by diffusion-controlled processes, irradiation induced creep is mostly due to the large number of irradiation induced point defects that cluster to promote the growth of and migration defect loops and voids by stress-assisted mechanisms. A number of irradiation creep mechanisms have been proposed and a widely accepted one among them is the stress induced preferential absorption (SIPA). SIPA involves the climb of edge dislocations perpendicular to their glide plane, by the absorption of interstitials that drift preferentially towards planes perpendicular to the direction of applied stress [9]. Embrittlement or the increase in the ductile-brittle transition temperature (DBTT) is another consequence of irradiation. The embrittlement has been proved to be a direct consequence of irradiation induced hardening and not due to the lowering of cohesive strength by irradiation [10].

Apart from the extrinsic pinning due to irradiation induced defects, the screw dislocations in BCC metals themselves are intrinsically pinned to the lattice, because of their compact, three-fold core structure [11]. Hence they have a high intrinsic lattice resistance which is otherwise known as the Peierls stress. The edge dislocations have lower Peierls stress and higher mobilities and hence the motion of screw dislocation is the rate-limiting physical mechanism, governing the plasticity of BCC metals. This property also applies to irradiated BCC metals, since a fairly high density of dislocations can be generated by irradiation. Hence dislocation motion is the primary mode of plasticity in

irradiated metals and forms the preliminary focus of our research in this thesis. Since irradiation induced defects are strong obstacles for the dislocation motion, they consequently modify the dislocation kinetics in the irradiated BCC metals, which will also be investigated here. Also since dislocations have stronger sink strengths for point defects than the grain boundaries, the dislocation-defect interactions become highly unavoidable. These defect-dislocation interaction events are hence central to the understanding of plasticity in irradiated metals. This thesis also studies the topic of dislocation-defect interaction in BCC Fe, so as to improve the continuum level predictions of the mechanical behavior of the same. The subsequent portions of this thesis deals with the study of irradiation induced defect in FCC metals like gold. As described earlier, stacking fault tetrahedra are the most important irradiation induced defect in FCC metals and have not generally been reported in non-irradiated metals. Our work reports the discovery of stacking fault tetrahedra in non-irradiated gold nanocrystals. We also study irradiation resistant materials with specific five-fold internal twin boundary structure that can act as strong sinks for irradiation induced point defects in FCC metals.

1.1.1 Necessity for a multiscale computational approach

Although various dislocation-defect interaction phenomena have been known for many years [1], the underlying fundamental mechanisms and their relation to the macroscopic deformation behavior have not been clearly demonstrated. Inelastic deformation of irradiated materials is essentially a multiscale study, since the constituting unit processes span length scales of over more than 15 orders of magnitude and time scales of over 21 orders of magnitude [12], thus spanning the entire atomistic-to-continuum length and time scale regimes. Hence a robust computational approach to

study the irradiation damage in materials should account for the atomistic level physics of the deformation processes involved, that can be coupled with continuum level models so as to achieve accurate predictions of the realistic mechanical behavior of the irradiated material. But most models of irradiation induced deformation and mechanical behavior still rely on empirical parameters fit to experimental data. The current state of modeling is hence mostly phenomenological and does not directly account for the accurate physics of the microscopic deformation mechanisms. However, with improvements in computational techniques and algorithms, it is now possible to probe the structure-property relationships through the detailed elucidation of fundamental atomic mechanisms. This thesis concentrates on the electronic structure, nanoscale mechanics and mesoscale evolution and transport, of the state-of-the-art multi-scale computational paradigm for the reasons discussed below.

One of the main goals of this thesis is to obtain a fundamental understanding of the unit processes driving inelastic deformation at ambient and high temperatures in irradiated BCC metals, specifically BCC Fe. Towards this purpose we employ a multiscale scheme of computational research that directly couples atomistic level research with macroscopic continuum level modeling [13], so as to make accurate predictions of the continuum level mechanical behavior of irradiated materials. Our multiscale research paradigm includes such efficient computational tools and techniques spanning broad length and time scales as Molecular Dynamics method (MD) , Nudged Elastic Band method, and coarse-grained Crystal Plasticity modeling.

In our research, brute force molecular dynamics simulations are conducted to obtain a preliminary understanding of the atomistic processes governing the dislocation motion

and dislocation-defect interaction events in BCC Fe. Since molecular dynamics calculations are limited to the unrealistically high stress regime (due to their inherently high strain rate) they are highly inefficient to study the kinetics of dislocation motion at low stress levels, relevant to laboratory experiments. Also due to the inherently short simulation times of MD (of the order of a few nanoseconds), such processes as the diffusion of point defects are beyond the timescale prowess of MD. Hence we develop and employ Nudged Elastic Band method (NEB) which is a transition state-theory based method [14] and a highly efficient tool to study the transition pathways of such rare events as defect motion and interactions. NEB results ultimately helps us understand the atomistic simulation results from the perspective of experimental length and time scales.

Our implementation of NEB method enables us with the capability of calculating the activation barriers of relevant unit processes that control the macroscopic plasticity in pure and irradiated BCC Fe. NEB also enables us to compute the activation energy as a function of stress, that in turn helps us compute the activation volume of the unit process. The stress-dependent activation volume is regarded as the kinetic signature of the deformation process [15] and hence yields significant physical information about the microscopic aspects of deformation and helps us identify the rate and strength limiting ones among the competing physical mechanisms. The stress dependant activation energy and activation volumes can further be used as material parameters for coarse-grained models like crystal plasticity, dislocation dynamics and so on [16]. In this work we develop a transition-state theory based, continuum level constitutive law which is implemented in a crystal plasticity framework. Apart from this approach and as

mentioned earlier, we also conduct large scale molecular dynamics simulations to investigate on irradiation induced defects like stacking fault tetrahedra and irradiation-resistant interfacial materials. Each among the aforementioned works is described briefly in the sections to follow.

1.1.2 Atomistically informed crystal plasticity model for BCC Iron

The mobility of dislocation in body-centered cubic (BCC) metals is controlled by the thermally activated nucleation of kinks along the dislocation core. Since plasticity in both pristine and irradiated BCC Fe is controlled by the motion of screw dislocation, we focus our study in Chapter 2 of this thesis, on deriving its kinetics through atomistic simulations and development of an atomistically informed crystal plasticity model. We employ a recent interatomic potential and the Nudged Elastic Band method, to predict the atomistic saddle-point state of $1/2\langle 111\rangle$ screw dislocation motion in BCC iron that involves the nucleation of *correlated* kinkpairs and the resulting double superkinks. This unique process leads to a single-humped minimum energy path that governs the one-step activation of a screw dislocation to move into the adjacent $\{110\}$ Peierls valley, which contrasts with the double-humped energy path and the two-step transition predicted by other interatomic potentials. Based on transition state theory, we use the atomistically computed, stress-dependent kinkpair activation parameters to inform a coarse-grained crystal plasticity flow rule. Our atomistically-informed crystal plasticity model quantitatively predicts the orientation dependent stress-strain behavior of BCC iron single crystals in a manner that is consistent with experimental results. The predicted temperature and strain-rate dependencies of the yield stress agree with experimental

results in the 200K-350K temperature regime, and are rationalized by the small activation volumes associated with the kinkpair mediated motion of screw dislocations.

1.1.3 Self Interstitial atom induced hardening and softening in irradiated BCC Iron

Plasticity in irradiated metals is strongly influenced by the hindrance to dislocation motion by irradiation induced crystalline defects like points defects, interstitial loops, voids and stacking fault tetrahedra. These defects are considered to contribute significantly to the macroscopic hardening response of the crystal. In Chapter 3, we investigate the interaction between self-interstitial atom and screw dislocation in irradiated BCC Fe using molecular dynamics and nudged elastic band calculations, in order to understand the dislocation motion in irradiated atmospheres. We find that the self-interstitial atom is absorbed into the screw dislocation core thereby forming a unique three-kink structure. These kinks are structural kinks and are different from the thermally nucleated kinks that normally aid the dislocation motion at finite temperatures. The reaction pathway for the motion of the dislocation with the three-kink structure is found to be comprised of two energy barriers corresponding to kink nucleation and depinning via kink collision, respectively. This two-step reaction pathway is atypical and different from that of the single-humped pathway for the motion of a pure screw dislocation. At high/room temperature regime, the three-kink structure results in a hardening response of the crystal, while at low temperature it can undergoes stress-assisted depinning and motion that manifests as a softening response of the crystal. This specific kinetics of the three kinked dislocation is attributed to be the microscopic reason for the experimentally reported softening behavior of irradiated metals at low temperatures.

1.1.4 Deformation induced formation of stacking fault tetrahedra under non-irradiated conditions

Stacking fault tetrahedra, which are three-dimensional crystalline defects bounded by stacking faults and stair-rod dislocations, are often observed in quenched or irradiated face-centred cubic metals and alloys. The stacking fault tetrahedra experimentally observed to date are usually supposed to originate from vacancies. In contrast to the classical vacancy-originated ones, we discover a new kind of stacking fault tetrahedra formed via the interaction and cross-slip of partial dislocations in Au nanocrystals. The complete atomic-scale processes of nucleation, migration and annihilation of the dislocation-originated stacking fault tetrahedra are revealed by *in situ* high resolution observations and molecular dynamics simulations and this forms the study of Chapter 4. The dislocation-originated stacking fault tetrahedra can undergo migration and annihilation due to mechanical loading in a manner that is not expected in bulk samples. These results uncover a unique deformation mechanism via dislocation interaction inside the confined volume of nanocrystals, and have important implications regarding the size effect on the mechanical behaviour of small-volume materials.

1.1.5 Study of the interface mediated plasticity and implications for irradiation damage

Microscale and nanoscale engineered materials with internal interfaces like twin boundaries or grain boundaries have been found to be very effective in resisting irradiation damage. In Chapter 5, we perform molecular dynamics simulations on silver nanowires with a special five-fold twinned internal interfacial microstructure, so as to study the hardening behavior exhibited by these nanowires. Metallic nanowires usually

exhibit ultra-high strength, but low tensile ductility owing to their limited strain hardening capability. We study the unique strain hardening behavior of five-fold twinned Ag nanowires by nanomechanical testing and atomistic modeling. *In situ* tensile tests, conducted inside scanning electron microscope (SEM), revealed strong strain hardening behavior of the five-fold twinned Ag nanowires, otherwise not pronouncedly exhibited by single crystalline nanowires. Molecular dynamics simulations captured such hardening in Ag nanowires containing twin boundaries and pre-existing defects. Strain hardening was found to be size dependent: thinner nanowires achieved more hardening and higher ductility. The size-dependent strain hardening was shown to be caused by the obstruction of surface nucleated dislocations by twin boundaries. Our work in this chapter provides mechanistic insights into enhancing the tensile ductility of metallic nanostructures by engineering the internal interfaces. The knowledge gained can be applied to further study the interactions of twin boundaries with irradiation-induced point and line defects.

CHAPTER 2

ATOMISTICALLY INFORMED CRYSTAL PLASTICITY MODEL FOR BCC IRON

2.1 Introduction

Plastic flow in body-centered cubic (BCC) metals is controlled by the motion of screw dislocations due to their high intrinsic lattice resistance [11, 17, 18]. The resolved shear stress required to move a screw dislocation at 0K (i.e., Peierls stress) is much higher than that for the edge dislocation, owing to the three-fold compact core of the former. However, this inherent difficulty to move a screw dislocation at finite temperatures can be mitigated by the thermal activation of kinks, which are essentially local perturbations on the straight dislocation line arising from the thermal fluctuation of atoms at the dislocation core. Hence, at finite temperatures (and low stresses) thermal activation of kinks is the rate-limiting step for the motion of screw dislocations in BCC metals [19].

Thermally activated dislocation motion and its influence on the macroscopic plasticity of BCC crystals comprise a multiscale problem due to the extremely fine length and time scales of atomic vibration and the coarse scales of dislocation motion and interaction during plastic flow. Regarding the atomistic aspect of this problem, molecular statics studies have considered the Peierls stress for dislocation motion based on two-dimensional (2D) simulations [20-24]. They also evaluated the material parameters quantifying the so-called non-Schmid effects on the Peierls Stress, i.e., the effect of (non-glide) stresses other than the maximum resolved shear stress [25]. However, these

studies were limited to the 2D mode of dislocation motion at 0K and could not account for the three-dimensional (3D) nature of the kinetics of dislocation motion via kink formation in the finite temperature regime.

Molecular dynamics (MD) studies have also been performed in the past with the aim of understanding the motion of screw dislocations for example in BCC Fe at finite temperatures [20, 26, 27]. However, direct MD is limited in simulation of the kinetic dislocation motion owing to the rare event nature of thermally activated kink nucleation. Also, the stress levels predicted using MD are elevated due to the high strain rates, and it is implausible to use MD to predict the stress-strain behavior of typical laboratory experiments at low strain rates. These limitations of MD underscore the need for a coarse-grained approach that can predict mechanical behavior at longer time scales without sacrificing the richness of atomistic information to inform the rate-controlling mechanisms of dislocation motion.

One coarse-grained modeling approach involves computing activation parameters of unit processes of thermally activated dislocation motion and then using them to inform a crystal plasticity model by invoking transition state theory [13]. In this scheme, the Nudged Elastic Band (NEB) method [14, 28, 29] has been used to compute the activation parameters of kink nucleation along a screw dislocation in BCC metals [30-33]. For example, Groger and Vitek [30] employed a periodically varying analytical Peierls potential for NEB studies of BCC Mo. Ngan and Wen [31] used the NEB method and Embedded Atom Method (EAM) potential to study kink nucleation along the core of a screw dislocation in BCC Fe. They predicted a degenerate dislocation core that is inconsistent with the non-degenerate core predicted by newer EAM potentials [34, 35],

Bond Order potential [21] and Density Functional Theory (DFT) [36]. The EAM potential for Fe used in [32] yielded the metastable dislocation core and associated double-humped minimum energy path which are likely artifacts of the potential, based on comparison with more accurate DFT studies [36, 37]. Recently, Proville *et al.* developed an EAM potential (hereafter referred to as Proville-EAM) [33] that predicted a single-humped 2D energy barrier, which agrees with the DFT results.

In this work, we employ the Proville-EAM potential and NEB method to compute the stress-dependent activation parameters for the 3D mode of thermally activated screw dislocation motion. We find a single-humped reaction pathway (i.e., minimum energy path) that is physically manifested as a correlated process of nucleation of leading and trailing kinkpairs, each of which consists of two atomically discrete kinks. Such a composite kink structure arises from the discrete 3D nature of the saddle-point state of screw motion, in contrast to the conventional line tension model of kink nucleation [19]. The corresponding atomistic material parameters are used to inform a plastic flow rule by invoking transition state theory. This atomistically informed crystal plasticity model predicted the deformation behavior of BCC Fe single crystals, specifically for the experimentally relevant low stress and finite temperature regime, where kink activation is the rate-limiting step in the kinetics of screw dislocation motion. This departs from other atomistically informed crystal plasticity models for BCC crystals [23, 38, 39] and other coarse-grained models [40, 41] that adopt an empirical relation [42] for describing the energetics of kink nucleation as a function of stress. The predictions of the orientation dependent tensile stress-strain relation from our model are in good agreement with experimental results for a BCC Fe single crystal [38, 43], thus providing some measure of

validation. Our model also predicts the temperature dependence of the yield stress, in quantitative agreement with the experimental results for BCC Fe [44]. The details of our atomistic methods and the crystal plasticity model are described in Section 2.2. The results and their implications are discussed in Section 2.3 and 2.4, respectively. Concluding remarks are given in Section 2.5.

2.2 Methods

The atomistic Nudged Elastic Band method and the atomistically informed crystal plasticity model are described in detail in the following two subsections, respectively.

2.2.1 Atomistic modeling

The Nudged Elastic Band (NEB) method is capable of effectively determining the reaction pathway and activation parameters of a stress-driven, thermally activated process to enable application of transition state theory for dislocation kinetics [45-48]. In this work, we used the NEB method to compute the minimum energy path and associated activation energy of a unit process of dislocation slip via kink nucleation in BCC Fe single crystals. As briefly discussed in the Introduction, the widely-used EAM potential developed by Mendelev *et al*. [34] is a favorable candidate for the atomistic simulations, since it well predicts the properties and also predicts a non-degenerate core for the screw dislocation, unlike its predecessors which had predicted a degenerate core structure [49, 50]. However, this potential predicts a double-humped 2D Peierls barrier with a metastable minimum, which is inconsistent with the single-humped Peierls barrier predicted by DFT [36, 37]. The most recent version of the Mendelev-EAM potential [35]

also predicts a double-humped barrier, although the depth of the metastable valley is less pronounced than its earlier one. Recently, Proville *et al*. [33] developed an EAM potential that predicted a single-humped Peierls barrier with an activation energy close to that predicted by DFT. Hence, we use the Proville-EAM potential for carrying out the atomistic simulations aimed at obtaining the mechanistically-based material parameters for the crystal plasticity model.

Figure 2.1(a) shows the 3D simulation supercell embedded with a screw dislocation at its ground state. The *x*, *y* and *z* axes are respectively oriented along the $[11\bar{1}]$, $[\bar{1}01]$ and $[\bar{1}2\bar{1}]$ directions. The simulation supercell is 54 nm long along its out-of-plane $[11\bar{1}]$ direction and its in-plane dimensions are 25nm and 25nm, respectively. For the 2D molecular statics calculations of the Peierls stress, we used the same setup but with a reduced out-of-plane dimension of 12.5 nm. The 1/2[111] screw dislocation is created at the center of the supercell by superimposing its elastic displacement field and subsequently relaxing the supercell with conjugate gradient method to obtain the minimum energy state. The outermost $(\bar{1}01)$ and $(\bar{1}2\bar{1})$ planes constituting the in-plane boundaries are traction free and hence fully relaxed so as to avoid the effect of stresses perpendicular to the glide direction. The shear stress required to move the dislocation is exerted by imposing a displacement-controlled boundary condition on a thin boundary layer of $(\bar{1}01)$ face, while the bottom boundary layer is held fixed. The dislocation glides on the maximum resolved shear stress plane (MRSSP), which is the $(\bar{1}01)$ plane for our setup. In this chapter, all the atomic configurations are colored by the centro-symmetry parameter [51] for showing the core structure of the screw dislocation.

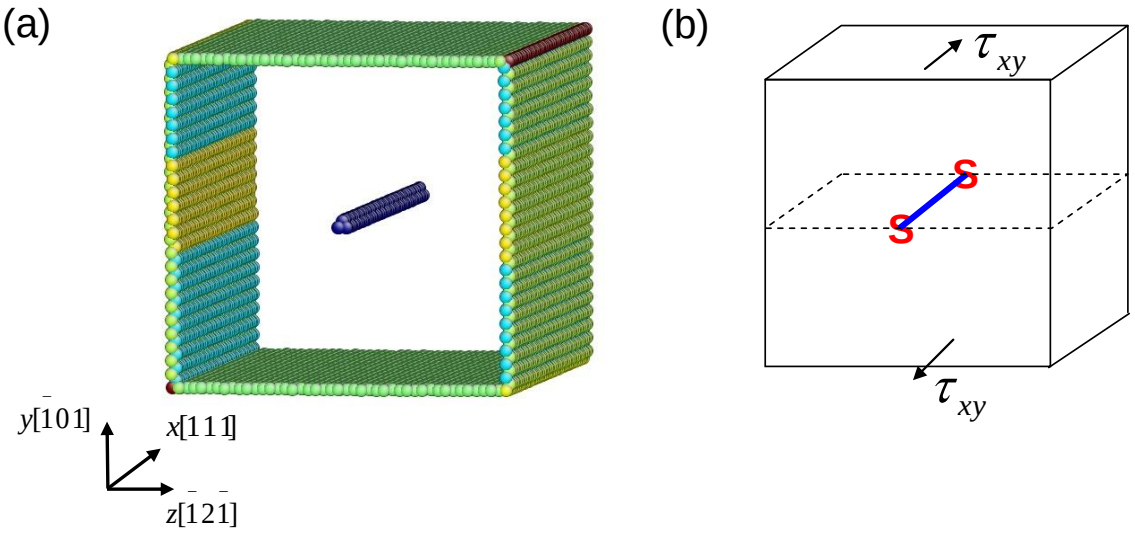

Fig. 2.1 Atomistic simulation set-up. (a) 3D perspective view of the supercell and the dislocation at its initial energy minimum state colored by centro-symmetry parameter [51]. **(**b**)** Schematic of the supercell showing details of the loading scheme.

NEB calculations were performed using the parallel molecular dynamics simulator LAMMPS [52]. Results were verified using an in-house NEB code. The initial state of the screw dislocation in the NEB simulation is shown in Fig. 2.1(a), and the final state is the energy minimum state of the same dislocation moved by one atomic distance from its initial state into the adjacent {1$\bar{1}$0} Peierls valley. The intermediate replicas are generated by linearly interpolating between atomic coordinates of the initial and final states. All the replicas are interconnected with springs that exert inter-replica forces, so as to rearrange replicas equi-distantly along the minimum energy path. The climbing image algorithm [53] is used to locate the saddle point of the energy barrier. The results were found to be insensitive to the value of the spring constant. A force tolerance of 0.05 eV/$\mathring{A}$ is employed to check the convergence of the NEB simulation.

2.2.2 Atomistically informed crystal plasticity modeling

We employ the crystal plasticity model structure of Asaro and Needleman [54] and Kalidindi *et al*. [55] to study the elastic-viscoplastic behavior of BCC Fe single crystals. In the continuum mechanics framework of finite deformation, the deformation gradient tensor $\mathbf{F}$ is decomposed as $\mathbf{F}=\mathbf{F}^{*}\mathbf{F}_{\mathrm{p}}$, where $\mathbf{F}^{*}$ and $\mathbf{F}_{\mathrm{p}}$ are the elastic and plastic deformation gradients, respectively. The time rate of the plastic deformation gradient is given by

$$\dot{\mathbf{F}}_{\mathrm{p}}=\mathbf{L}_{\mathrm{p}}\mathbf{F}_{\mathrm{p}} \tag{1}$$

where

$$\mathbf{L}_{\mathrm{p}}=\sum_{\alpha}\dot{\gamma}^{\alpha}\mathbf{S}_{0}^{\alpha} \tag{2}$$

is the plastic deformation velocity gradient and $\mathbf{S}_{0}^{\alpha}=\mathbf{m}_{0}^{\alpha}\otimes\mathbf{n}_{0}^{\alpha}$, where $\mathbf{m}_{0}^{\alpha}$ and $\mathbf{n}_{0}^{\alpha}$ are fixed orthonormal unit vectors, defining respectively the slip direction and slip plane normal of the $\{110\}\langle 111\rangle$ slip system α in the reference configuration. Here, $\dot{\gamma}^{\alpha}$ is the plastic shearing rate on slip system α, given by Orowan's relation $\dot{\gamma}^{\alpha}=b\rho v^{\alpha}$, where b is the Burgers vector length of the screw dislocation, ρ is the mobile dislocation density, and v^{α} is the dislocation velocity on slip system α. Using transition state theory, the flow rule for $\dot{\gamma}^{\alpha}$ is related to the stress-biased activation energy for dislocation motion, i.e.,

$$v^{\alpha}=v_{0}\exp\left(-\frac{H(\tau_{\mathrm{eff}}^{\alpha})}{k_{\mathrm{B}}T}\right) \tag{3}$$

where v_0 is the reference dislocation velocity, H is the activation energy for unit dislocation slip, k_{B} is the Boltzmann constant, T is the absolute temperature, and $\tau_{\mathrm{eff}}^{\alpha}$ is the effective shear stress that drives dislocation motion on slip system α. Since kink nucleation is the rate-limiting step for screw dislocation motion, it controls the kinetics in Eq. (3) via dependence on the associated activation energy H, as discussed later.

Combining the Orowan relation with Eq. (3) leads to

$$\dot{\gamma}^{\alpha} = \begin{cases} 0, & \text{if} \quad \tau_{\mathrm{eff}}^{\alpha} \le 0 \\ \dot{\gamma}_0 \exp\left(-\dfrac{H(\tau_{\mathrm{eff}}^{\alpha})}{k_{\mathrm{B}}T}\right)\mathrm{sign}(\tau^{\alpha}), & \text{if} \quad \tau_{\mathrm{eff}}^{\alpha} > 0 \end{cases} \tag{4}$$

where the pre-factor $\dot{\gamma}_0$ is the reference strain rate. The effective resolved shear stress $\tau_{\mathrm{eff}}^{\alpha}$ on slip system α is expressed as the difference between the applied resolved shear stress and the athermal slip resistance s_{a}^{α} due to the long-range barriers, i.e.,

$$\tau_{\mathrm{eff}}^{\alpha} = \left|\tau^{\alpha}\right| - s_{\mathrm{a}}^{\alpha} \tag{5}$$

Based on the assumption that elastic stretch is infinitesimal for metals, τ^{α} can be expressed as

$$\tau^{\alpha} = (\mathbf{C}^{*}\mathbf{T}^{*}) : \mathbf{S}_0^{\alpha} \approx \mathbf{T}^{*} : \mathbf{S}_0^{\alpha} \tag{6}$$

where $\mathbf{C}^{*}$ is the right Cauchy-Green tensor given by $\mathbf{C}^{*} = \mathbf{F}^{*\mathrm{T}}\mathbf{F}^{*}$ and $\mathbf{T}^{*}$ is the second Piola-Kirchhoff stress tensor [55].

The stress-dependant kink activation energy H in Eq. (4) can be written in the Kocks form [42] as

$$H = H_0\left[1 - \left(\frac{\tau_{\mathrm{eff}}^{\alpha}}{s_{\mathrm{t0}}}\right)^{p}\right]^{q} \tag{7}$$

where H_0 is the activation energy for dislocation motion when the effective shear stress $\tau_{\text{eff}}^{\alpha}$ is zero, p and q are the profiling parameters, and s_{t0} is the thermal slip resistance at 0K (Peierls stress), assuming the same value for all the slip systems $s_{\text{t0}}^{\alpha} \approx s_{\text{t0}}$ [56]. Since the thermal part of the slip resistance in BCC metals is primarily due to the lattice resistance that does not evolve with deformation, we treat s_{t0} as a constant. Thus, the part of the total slip resistance that evolves is the athermal slip resistance s_{a}^{α} due to the long-range barriers. The evolution of s_{a}^{α}, with the same initial value for all the slip systems $s_{\text{a0}}^{\alpha} \approx s_{\text{a0}}$ [56], is prescribed as

$$\dot{s}_{\text{a}}^{\alpha} = \sum_{\beta} q^{\alpha\beta} h^{\beta} \left| \dot{\gamma}^{\beta} \right| \tag{8}$$

where $q^{\alpha\beta}$ is the hardening matrix [54] given by $q^{\alpha\beta} = Q + (1-Q)\delta_{\alpha\beta}$ (Q is the latent hardening coefficient and $\delta_{\alpha\beta}$ is the Kronecker delta), and h^{β} is the self-hardening rate of slip system β given as

$$h^{\beta} = h_0 \left(1 - \frac{s_{\text{a}}^{\beta}}{s_{\text{a,s}}^{\beta}} \right)^{r} \text{sign}\left(1 - \frac{s_{\text{a}}^{\beta}}{s_{\text{a,s}}^{\beta}} \right) \tag{9}$$

where h_0 is the initial self-hardening rate, r is a material parameter and $s_{\text{a,s}}^{\beta}$ is the saturation value of the athermal slip resistance.

The crystal plasticity model illustrated to this point is the standard approach. We next explain how information regarding the unit process of kink nucleation from the atomistic model is bridged with the crystal plasticity model. The atomistic NEB calculation

(as explained in Section 2.2.1) enables the quantification of kinkpair activation energy H as a function of the effective applied shear stress $\tau_{\text{eff}}^{\alpha}$. The atomistically computed data for H versus $\tau_{\text{eff}}^{\alpha}$ are then fit to the Kocks form as in Eq. (7). Thus, the values of the parameters H_0, p, q and s_{t0} in Eq. (7) are determined from our atomistic results.

The pre-exponential factor $\dot{\gamma}_0$ in Eq. (4) is also atomistically informed and estimated as follows. Assuming that the Debye frequency ν_{D} for BCC Fe can be used as a quantitative measure for the attempt frequency of nucleation of thermal kinks, $\dot{\gamma}_0$ can be approximately written as [30]

$$\dot{\gamma}_0 = \frac{b^2 a \rho \nu_{\text{D}}}{l} \tag{10}$$

where l is the lateral extent of kinks at the saddle-point state and a is the distance that the dislocation moves in one activation step, equal to the lattice constant in the $[\bar{1}2\bar{1}]$ direction. The value of l can be estimated from our atomistic results and thus $\dot{\gamma}_0$ becomes an atomistically informed property for a given mobile dislocation density.

We choose to consider only the twelve $\{110\}\langle 111\rangle$ slip systems in our crystal plasticity model [16] and exclude the twelve $\{112\}\langle 111\rangle$ slip systems. This is because we have found in our atomistic studies that each unit process of slip in a $\{112\}$ plane proceeds by two individual slip steps on the non-parallel $\{110\}$ planes. As a result, the rate-limiting step for slip on a $\{112\}\langle 111\rangle$ slip system is still the formation of kinks on the $\{110\}\langle 111\rangle$ slip system that is studied in this work. However, in the case of the MRSSP close to $\{112\}$ (wavy slip on $\{112\}$ has been often observed at finite temperatures in

BCC metals [57]), our viscoplastic formulation can effectively approximate the kinematic effect of plastic shear on the $\{112\}\langle 111\rangle$ slip system through simultaneous activation of the most highly stressed primary slip system of $\{110\}\langle 111\rangle$ and other less stressed ones. In addition, experimentally observed finite temperature cross slip into any crystallographic plane between the primary and secondary $\{110\}\langle 111\rangle$ slip systems can also be activated depending on the ratio of the number of elementary steps on the primary and the secondary $\{110\}\langle 111\rangle$ planes. The simultaneous activation of multiple $\{110\}\langle 111\rangle$ systems is facilitated by the relatively small activation volume of screw dislocation motion in BCC metals and accordingly large strain rate sensitivity, to be detailed later.

2.3 Results

2.3.1 Molecular statics and 2D NEB

We performed several benchmark calculations to verify that the Proville-EAM predicts the correct features of the BCC Fe apart from the basic crystalline properties verified in [33]. Figure 2.2 shows the differential displacement plot of a screw dislocation core [58] as predicted by Proville-EAM based on a conjugate gradient energy minimization calculation. The core spreads onto the three $\{110\}$ planes of the [111] zone and is non-degenerate, as it does not exhibit dyadic asymmetry.

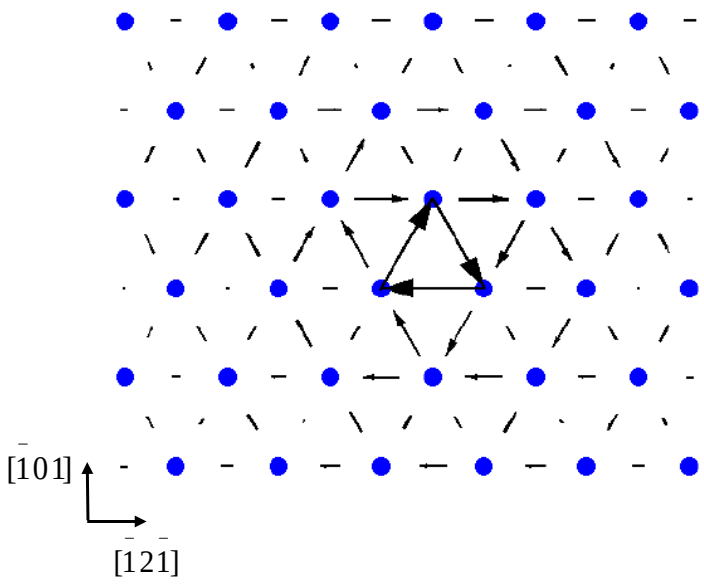

Fig. 2.2 Differential displacement plot of the non-degenerate screw dislocation core predicted by Proville-EAM.

The non-degeneracy of the core is in accordance with the DFT results [36, 37]. We also evaluated the 0K Peierls stress as a function of the orientation of the MRSSP, using a conjugate gradient energy minimization loading scheme. Anti-plane shear was applied onto a 2D simulation cell, which corresponds to the 3D simulation cell in Fig. 2.1 with reduced thickness. The incremental displacement was imposed on a boundary layer of the $(\bar{1}01)$ plane, with energy minimization carried out after each increment. The magnitude of the incremental displacement was controlled to limit the build-up of stress to $0.001C_{44}$, where C_{44} is the elastic constant of BCC Fe. To evaluate the orientation effect on MRSSP, new configurations were created by rotating the simulation cell about the [111] axis in Fig. 2.1 by an angle χ, whose magnitude is between -30° and +30° owing to the symmetry of the BCC lattice. As shown in Fig. 2.3, the orientation dependent Peierls stress does not follow Schmid's law and instead exhibits an asymmetry which is due to the twinning-antitwinning asymmetry intrinsic to the BCC lattice [20, 21].

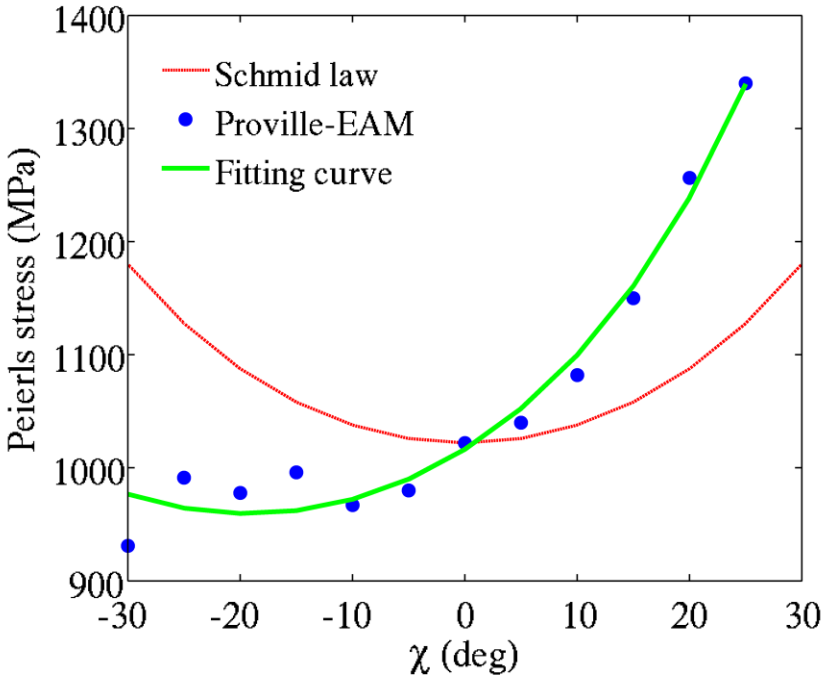

Fig. 2.3 Orientation dependence of the Peierls stress predicted by Proville-EAM in 2D simulations. The results are fit to an equation of the form [21] $\mathrm{CRSS}(\chi)=\tau_{\mathrm{cr}}^{*}\Big/\left[\cos\chi+a_1\cos(\chi+\frac{\pi}{3})\right]$ and the values of the fitting parameters are $a_1=0.50$ and $\tau_{\mathrm{cr}}^{*}=1.27$ GPa.

We also conducted 2D NEB calculations of the energy barrier for the screw dislocation motion, in order to compare different EAM potentials. While the physically meaningful energy barriers require 3D NEB calculations, the 2D NEB study can be readily compared with the computationally intensive DFT results, thereby providing a quick check regarding the quality of EAM potentials. The 2D NEB result from Proville-EAM is compared with that predicted by Mendelev-EAM in Fig. 2.4. The Proville-EAM predicts a single-humped curve, while the Mendelev-EAM predicts a double-humped one with a metastable intermediate state, as discussed earlier. The saddle-point energy of 0.028 eV per *b* from Proville-EAM is comparable to that from DFT [33].

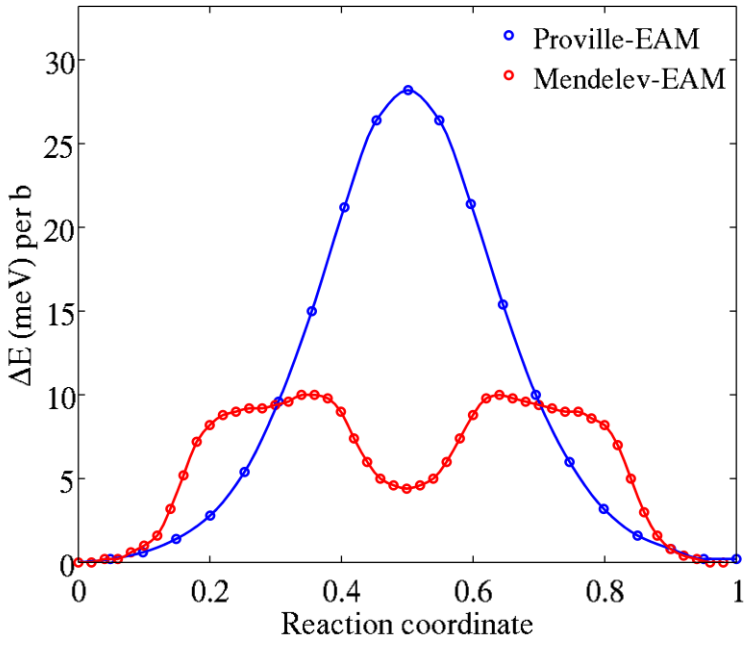

Fig. 2.4. 2D Peierls barriers predicted by Proville-EAM and Mendelev-EAM potentials.

These results show that the Proville-EAM can effectively describe dislocations in BCC Fe. However, since these 2D calculations cannot capture the 3D localized mode of kink nucleation as the rate-limiting step of screw dislocation motion, we proceed next with 3D NEB simulations.

2.3.2 Correlated kinkpair nucleation

3D NEB simulations were carried out with the simulation setup in Fig. 2.1 to study the mechanism of kink nucleation and obtain the stress-dependent activation parameters. Figure 2.5(a) shows a converged minimum energy path for the unit process of thermally activated screw dislocation glide under zero applied stress, in which the energy of replicas is plotted against the reaction coordinate defined as the normalized path length of minimum energy path.

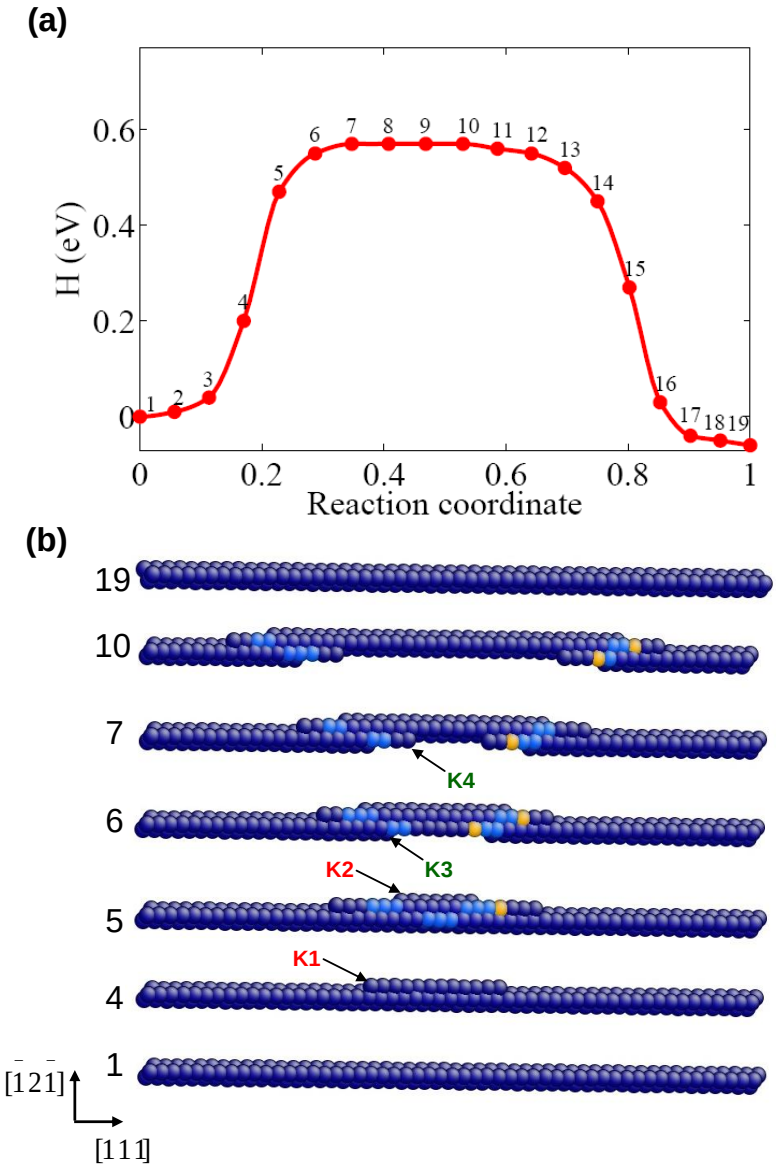

Fig. 2.5 3D NEB results of thermally activated screw dislocation motion at zero stress. (a) Minimum energy path for the correlated kinkpair nucleation. (b) Atomistic configurations of the corresponding replicas along the minimum energy path.

The atomistic configurations of replicas are shown in Fig. 2.5(b). Replicas 1 and 19 are respectively the initial and the final states of the unit process, where the core of the screw dislocation moves by one atomic distance on the $(\bar{1}01)$ plane, along the $[\bar{1}2\bar{1}]$ direction. The rest of the configurations are those of intermediate replicas on the minimum energy path. The saddle-point state is replica 7 and it has an energy of 0.57 eV, assuming the

initial state has zero energy. It can be seen that the dislocation moves one atomic distance by the nucleation of four different kinks, K1, K2, K3 and K4, as marked in the replicas of Fig. 2.5(b). K1 and K2 are hereby defined as the *leading kinks* and together form the *leading kinkpair*, while K3 and K4 are defined as the *trailing kinks* and together form the *trailing kinkpair*, the reasons for which are discussed below.

To understand the crystallographic details of the kinkpair nucleation, it is important to first understand the structural changes to the dislocation core due to the nucleation of the kinkpairs. For that purpose, we plot the differential displacement (DD) maps of various points along the dislocation line at its saddle state (replica #7 of Fig. 2.5(b)). The results are shown in Fig. 2.6. Figures 2.6(b-f) are the DD plots of the cross-sections (with $[1\bar{1}1]$ as their normals) as marked on the saddle state of Fig. 2.6(a). The four individual kinks are also marked. The three $\{1\bar{1}0\}$ planes of the $[1\bar{1}1]$ zone are marked in the DD plot in Fig. 2.6(b). Figure 2.6(b) shows the non-degenerate compact core of the part of the dislocation in the initial Peierls valley, P1, marked as point (b). As can be noted, the core is compact and spread equally into the three $\{1\bar{1}0\}$ planes.

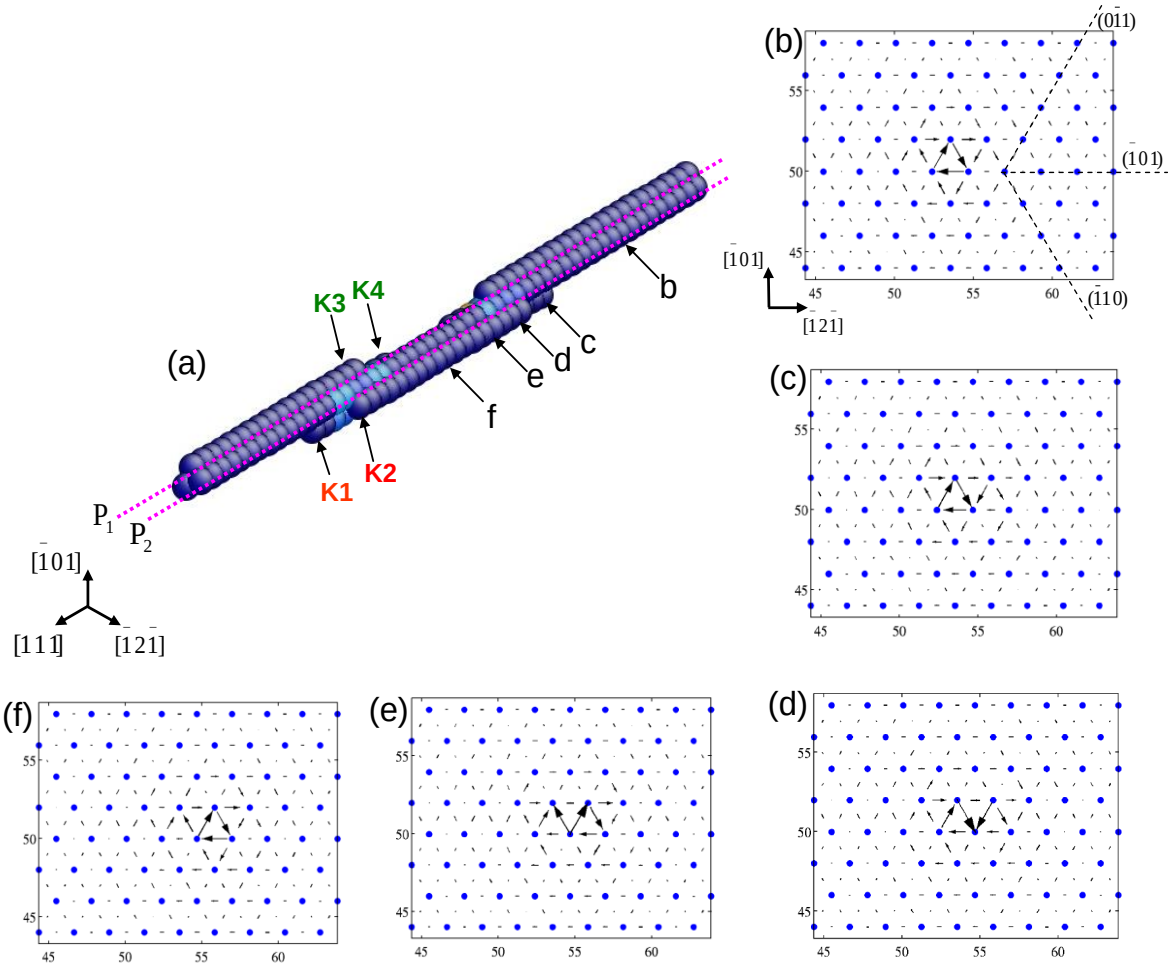

Fig. 2.6 Differential displacement plots. (a) Saddle point state (replica #7 of Fig. 2.5(b)). (b-d) DD plots of the dislocation core at various points along the dislocation line, as marked in Fig. 2.6(a).

Point (c) on the dislocation line denotes the local core spreading due to the first leading kink, K1. The corresponding DD plot shows that the core is spread along the $(\bar{1}01)$ plane. Figure 2.6(f) shows the compact core state of the part of the dislocation line in the new Peierls valley, P2; and Figs. 2.6(d-e) show the rest of the split core states between the two compact core states. Thus, the compact core states in the adjacent Peierls valleys (points (b) and (f)) are progressively bridged by the split-core states of points (c), (d) and (e) which in total involve the four atomistically discrete kinks; K1-K2 (leading kinkpair) and

K3-K4 (trailing kinkpair). Meanwhile, the saddle state predicted by Mendelev-EAM has a split-core state that is uniformly the same along the dislocation line, as can be seen in the replica #11 in Fig. 2.7(b). The DD plot of its core structure is as in Fig. 2.7(c) and is comparable to the short split-core segment represented by point (d) in the saddle state of Fig. 2.6(a).

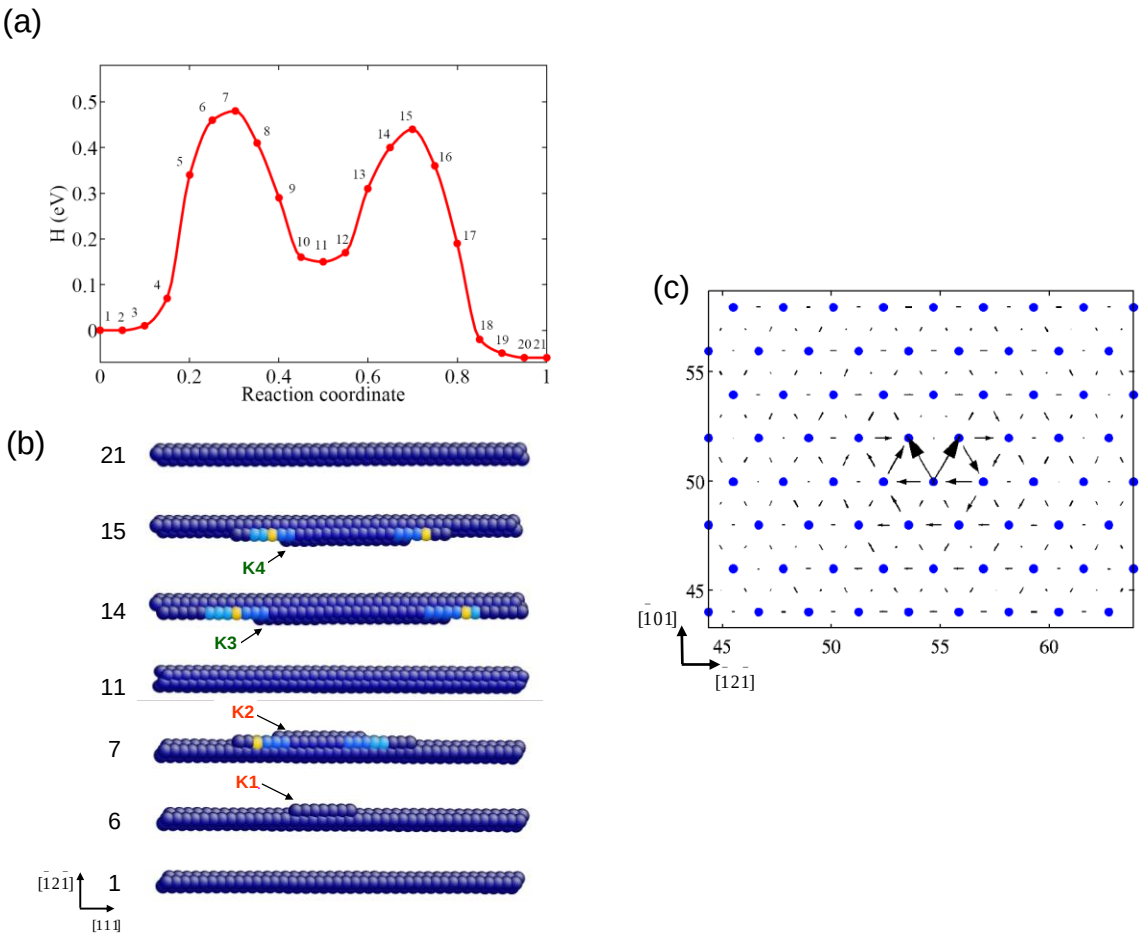

Fig. 2.7. Uncorrelated kinkpair nucleation predicted by Mendelev-EAM for zero stress. (a) Double-humped minimum energy path. (b) Atomistic configurations of the corresponding replicas along the minimum energy path. (c) DD plot of the split-core state of the saddle state (replica #11) in (b).

The salient feature of our 3D NEB result is the activation mechanism of *correlated* kinkpair nucleation, which results in a single-humped minimum energy path unlike the

Mendelev-EAM that predicts a double-humped one [32], as shown in Fig. 2.7(a). Figure 2.8(a) shows a perspective view of the saddle-point state (replica 7 in Fig. 2.5(b)) colored based on centro-symmetry parameter and its crystallographic details, as understood from Fig. 2.6 and Fig. 2.8(a) are shown in the schematic of Fig. 2.8(b). The kinks K1 and K2 (leading kinkpair) nucleate first and are colored in red, while the kinks K3 and K4 (trailing kinkpair) nucleate subsequently, and are colored in green. Thus the saddle-point state is composed of both the leading and the trailing kinkpairs, unlike the split-core saddle state predicted by Mendelev-EAM (see Fig. 2.7(b)). Such a nucleation event, in which both the leading kinkpair and the trailing kinkpair nucleate simultaneously, can be considered as a correlated mode [32] and is the reason for the usage of the term 'correlated kinkpair nucleation'.

It can be observed that the correlated kinkpair nucleation involves two adjacent $(\bar{1}01)$ planes. In Fig. 2.8(b), the top $(\bar{1}01)$ plane and the kinks contained in it are represented by solid lines, while the bottom plane and its kinks are represented by dotted lines. The leading kink K2 and the trailing kink K3, lie on the top $(\bar{1}01)$ plane and shift the two atomic columns on the top $(\bar{1}01)$ plane by one lattice distance, while the leading kink K1 and the trailing kink K4 lie on the bottom $(\bar{1}01)$ plane and shift the bottom column by one lattice distance, which together translate the dislocation line into the new Peierls valley, P2. Hence, a single event of correlated kinkpair nucleation involves the coordinated movement of kinks on two $(\bar{1}01)$ planes of the $[11\bar{1}]$ zone.

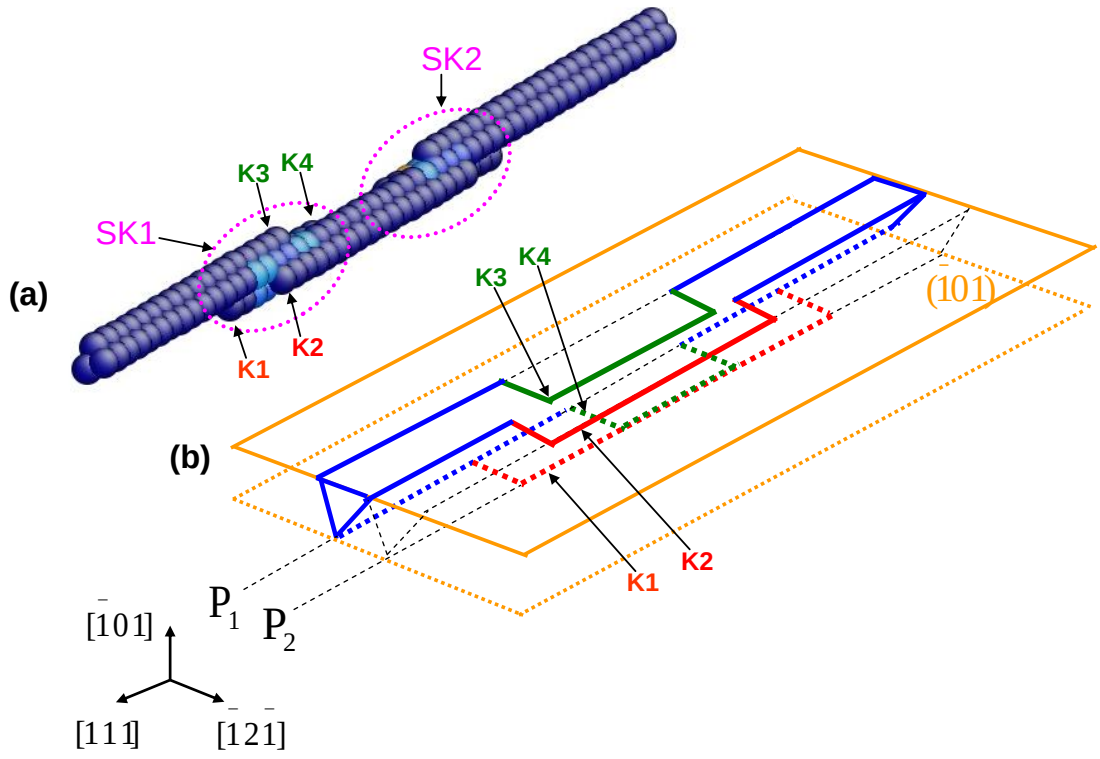

Fig 2.8 Atomistic details of correlated kinkpair nucleation. (a) Perspective view of the saddle point state showing the double superkink, SK1 and SK2, as well as the constitutive individual kinks, K1 to K4. (b) Schematic showing the crystallographic details of the saddle-point configuration. P_1 and P_2 indicate the adjacent Peierls valleys. Note that the top $(\bar{1}0\bar{1})$ plane and the kinks within this plane are represented by solid lines, while the bottom plane and its kinks are represented by dotted lines.

The leading and trailing kinkpairs are collectively defined as one *superkink*, marked as SK1 in Fig. 2.8(a). The prefix 'super' emphasizes the composite nature of each superkink, composed of four constituting kinks. Incidentally, the superkink should not be confused for a kink traversing several lattice valleys, which has been termed as a 'macro-kink' [59]. Note that the nucleation event of an opposite superkink occurs simultaneously and is marked as SK2 in Fig. 2.8(a). As a result, the saddle-point configuration involves a *double superkink* containing two superkinks of opposite signs, and each superkink consists of leading and trailing kinkpairs.

The formation of *double superkinks* produces a localized displacement of the screw dislocation from the Peierls valley P1 to P2 on the $(\bar{1}01)$ plane via a one-step transition, as shown in Fig. 2.8(b). This unique one-step transition and its single-humped activation pathway contrast with the two-step transition and the associated double-humped activation pathway predicted by other interatomic potentials, e.g., Fig. 2.7(a). This will be further addressed in the Discussion section. The distance between the leading kinks K1 in the double-superkink structure at the saddle point corresponds to the value for l in Eq. (10) for determining the pre-factor $\dot{\gamma}_0$ and is characteristically around $25b$.

2.3.3 Stress-dependent kinkpair activation energy and activation volume

We repeated NEB calculations for varying levels of applied shear stress to characterize the stress dependence of the activation energy for correlated nucleation of kinkpairs (i.e. double superkinks of opposite signs). The initial and final states for the NEB calculation were maintained at similar shear-stress levels by holding constant the finite-displacement of the surface layer. Figure 2.9(a) shows the minimum energy paths for various applied shear stresses.

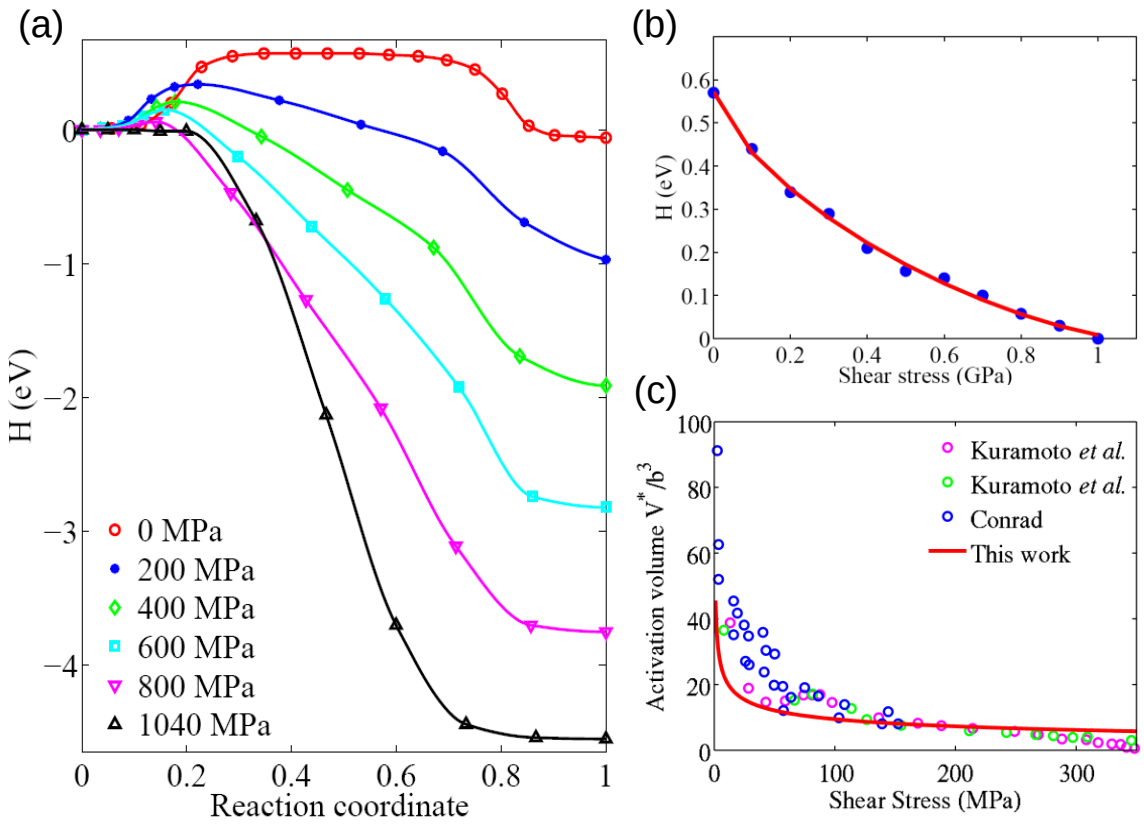

Fig. 2.9 Shear stress-dependent minimum energy path (MEP) and activation energy. (a) MEPs for correlated kinkpair nucleation at finite shear stresses. (b) Data points of calculated activation energy versus shear stress, fit to a curve of the Kocks form as in Eq. (7). (c) Calculated activation volume as a function of shear stress, compared with experimental measurements by [44] and [60].

As the shear stress is increased, the minimum energy path is tilted and the saddle-point energy is reduced accordingly. At an applied shear stress around 1.04 GPa, the energy barrier vanishes, which implies that the kinkpair nucleation occurs spontaneously at this stress level without the need for overcoming a barrier by thermal activation. This stress value should thus correspond to the classical Peierls stress at 0K, which is conventionally used as a quantitative measure for the intrinsic lattice resistance to dislocation motion. Our 2D simulation results shown in Fig. 2.2 also predicted the same magnitude for the Peierls stress (for $\chi = 0$), which thus serves as a check for the 3D NEB implementation

and results. Incidentally, the minimum energy paths in Fig. 2.9(a) are similar to those reported by Proville *et al*. [33]. However, they did not study the atomic details of the activation mode and did not consider their implications for crystal plasticity modeling.

Figure 2.9(b) shows the activation energy H as a function of the applied shear stress, which is denoted as $\tau_{\text{eff}}^{\alpha}$ in our crystal plasticity model. The data points in the plot of H versus $\tau_{\text{eff}}^{\alpha}$ can be fit to Eq. (7) to obtain the material parameters for quantifying the kinkpair nucleation kinetics. The activation energy for dislocation motion at zero stress, H_0, is the intercept of the H versus $\tau_{\text{eff}}^{\alpha}$ curve on the *y*-axis, given by 0.57 eV. The thermal slip resistance at 0K, s_{t0}, is the intercept on the *x*-axis, given by 1.04 GPa. They will be further discussed later. The dimensionless profiling parameters, p and q, are 0.667 and 1.18, respectively. These atomistically determined values are numerically close to $p = 0.748$ and $q = 1.172$, derived by Tang *et al*. [40] by fitting to the experimental results for BCC Ta. But our values of p and q differ significantly from the ones customarily assumed in crystal plasticity models, e.g., $p = 1$ and $q = 2$ as in [23], $p = 1$ and $q = 1$ as in [38]. To evaluate $\dot{\gamma}_0$ in Eq. (10), we first estimate the Debye frequency for Fe according to [61]

$$\nu_{\text{D}} = \left(\frac{3N}{4\pi V} \right)^{1/3} \nu_s \tag{11}$$

where N/V is the number density of the BCC lattice (0.0846Å^{-3}) and ν_s is the speed of sound, which is equal to 5130 m/s in Fe. The value of ν_{D} is thus estimated to be 1.39×10^{13} /s. The dislocation density is assigned as 10^{15} /m^2, which is a reasonable value for plastically deformed crystals at moderate levels of deformation. As discussed earlier,

the value of l is characteristically about $25b$, corresponding to the length between the two superkinks at the saddle state in NEB results. The value of a is numerically equal to the lattice constant in the $[\bar{1}2\bar{1}]$ direction, which is 2.298 Å. Given all these values, Eq. (10) yields $\dot{\gamma}_0 = 3.19\times10^7/\text{s}$. The values of the above atomistically determined material parameters are listed in Table 1.

Table 2.1 Atomistically determined parameters for stress-dependent activation energy H and shearing rate prefactor $\dot{\gamma}_0^{\alpha}$.

H_0	s_{t0}	p	q	$\dot{\gamma}_0$
0.57 eV	1.04 GPa	0.67	1.18	$3.19\times10^7/\text{s}$

The stress-dependant activation volume, V^*, for the nucleation of double superkinks can be estimated from the slope of the H versus $\tau_{\text{eff}}^{\alpha}$ curve, as it is defined as $V^* = -\frac{\partial H(\tau_{\text{eff}}^{\alpha})}{\partial \tau_{\text{eff}}^{\alpha}}$. Note that the activation volume is a function of stress, as shown in Fig. 2.9(c), and decreases as stress is increased, which correlates well with the experimental estimates from the strain-rate sensitivity measurements [44, 60]. For stresses greater than 0.2 GPa, the activation volume varies slowly between about $2b^3$ and $7b^3$. Below 0.2 GPa, the activation volume starts increasing at a faster rate, since the rate of change of the slope of the H versus $\tau_{\text{eff}}^{\alpha}$ curve is larger in this regime. Overall, the computed activation volume is small, in the range of $1\sim20b^3$. These characteristically small activation volumes are expected, since the nucleation of double superkinks is a highly localized

mode of displacement of the dislocation core, occurring over a length scale of a few nanometers. The small activation volumes could lead to significant temperature and strain rate sensitivity of the yield stress [48], as shown next.

2.3.4 Stress-strain behavior from crystal plasticity simulations

The atomistically determined material parameters in Table 1 are introduced into our crystal plasticity model, so as to enable the atomistically informed simulation of uniaxial tensile tests of BCC Fe single crystals. In this work, we focus on the orientation, temperature and strain rate dependence of the yielding and hardening behavior. The elastic constants for BCC Fe are set to C_{11} = 236 GPa, C_{12} = 134 GPa, and C_{44} = 119 GPa [23, 38]. Table 2 lists the values of all other material parameters in our model, apart from the atomistically determined ones in Table 1. Essentially, the parameters in Table 2 characterize the work hardening behavior rather than initial yield stress. Simulation results are compared with experimental results for BCC Fe single crystals [43]. The strain rate employed in our crystal plasticity simulations was $3.3\times10^{-4}/\mathrm{s}$, consistent with the strain rate used in the aforementioned experiments.

Table 2.2 Material parameters for the crystal plasticity model.

$s_{\mathrm{a0}}(=s_{\mathrm{a0}}^{\alpha})$	h_0	Q	r	$s_{\mathrm{a,s}}(=s_{\mathrm{a,s}}^{\alpha})$
18 MPa	500 MPa	1.4	1.8	160 MPa

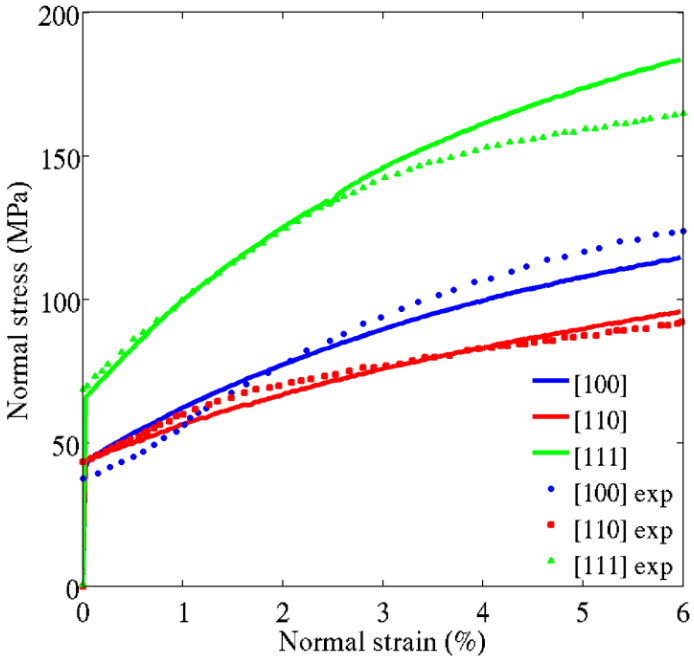

Fig. 2.10 Orientation dependent stress-strain behavior of BCC Fe predicted by our atomistically informed crystal plasticity model and compared with experimental stress-strain curves [43].

Figure 2.10 shows the stress-strain curve of uniaxial tension for three different orientations, i.e., [100],[110] and [111], compared with their corresponding experimental curves. It is noted that our atomistic results predict the temperature- and rate-dependent flow, while the work hardening is a result of correlation of the overall dataset of model parameters.

The atomistically informed crystal plasticity model exhibits a strong orientation dependence of initial yield stress and work hardening that matches the corresponding experimental data reasonably well. Such orientation dependence can be qualitatively understood in terms of the Schmid factors. Namely, the orientation difference between the applied load and the primary slip system is mainly responsible for the difference of the tensile stress at the yield point.

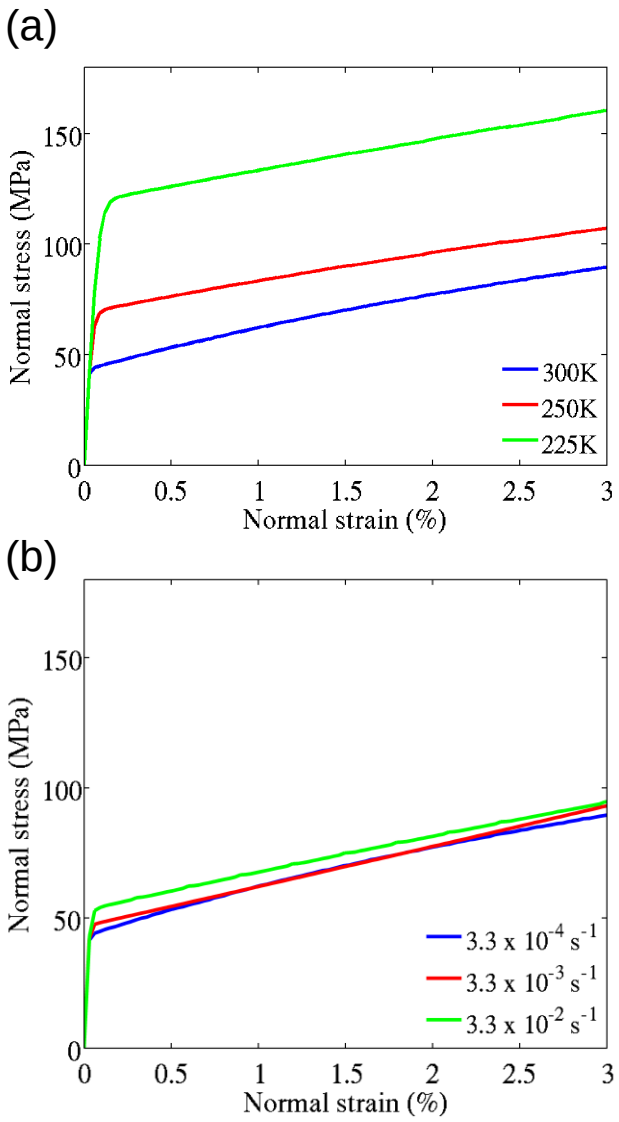

Fig. 2.11 Predictions from our atomistically informed crystal plasticity model for tensile loading along the [100] orientation. (a) Temperature dependence of stress-strain behavior at a strain rate of $3.3\times10^{-4}/\mathrm{s}$. (b) Strain rate dependence of stress-strain behavior at 300K.

Figures 2.11(a) and (b) show the tensile stress-strain curves predicted by the atomistically informed crystal plasticity model for various temperatures and strain rates, for the [100] loading orientation. The results show that the plastic behavior of BCC Fe single crystals depends strongly on temperature and strain rate, which is understandable considering the small activation volumes ($1\sim20b^3$) associated with the localized

nucleation of kinkpairs and the small distance between the two superkinks. The strain rate dependent yield stresses in Fig. 2.11(b) are used to calculate the rate sensitivity parameter m according to $m = \frac{\partial \ln \tau_{\text{eff}}^{\alpha}}{\partial \ln \dot{\gamma}^{\alpha}}$, giving $m = 0.05$. This value falls within the range of experimentally determined values for BCC Fe of various grain sizes, as reported by Wei *et al*. [62].

The yield stress from our crystal plasticity simulations is extracted as a function of temperature for the [100] loading orientation and is compared in Fig. 2.12 with the experimental results by Kuramoto *et al.* [44] and Brunner *et al.* [63]. The yield stress predictions match very well with those by experiments for the temperature range 200K-350K, which is of our interest in this work. Below 200K, we find that the yield stress predictions by our model are higher than the experimental values and lack quantitative agreement. This discrepancy is expected, considering the high values of the Peierls stress predicted by the EAM potentials in general which are around 2 to 3 times the experimentally observed yield stresses at finite temperatures, extrapolated to 0K. Such inconsistency between the atomistic and experimental predictions of yield stresses has been well discussed in the literature.

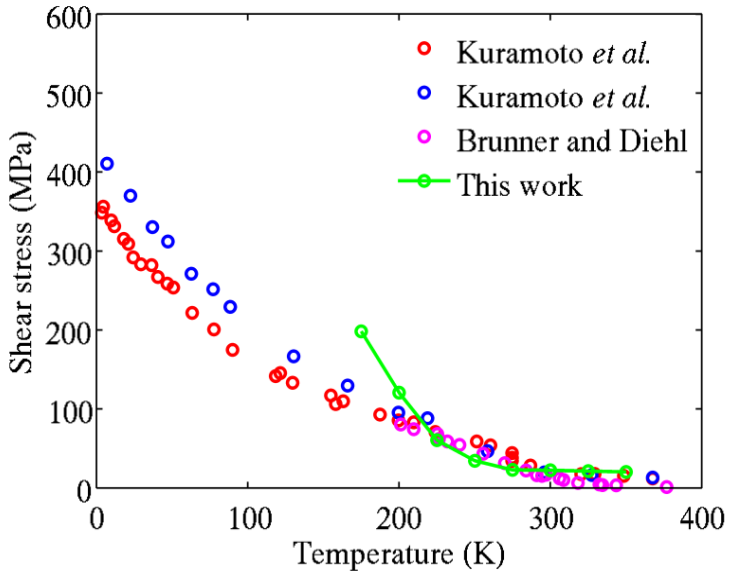

Fig. 2.12 Yield Stress as a function of temperature for the [100] loading orientation: comparing crystal plasticity results with experimental results from [44] and [63].

However, it is not fully resolved yet, even though various explanations such as the quantum effect [33, 64], effect of interaction between a group of dislocations [65], role of mixed dislocations in controlling the yield [66], etc. have been suggested in the past. Irrespective of this unresolved issue, our study proves that kinkpair activation parameters obtained from NEB calculations can be successfully incorporated into a crystal plasticity model to predict the macroscopic stress-strain behavior at low stresses in the regime around room temperature.

2.4 Discussion

In this section we discuss the implications of our atomistic results regarding kinkpair nucleation, as well as the assumptions made in our atomistic and crystal plasticity models, and their linkage. First, we emphasize that the mechanism of *correlated* kinkpair nucleation revealed in our atomistic simulations is a direct outcome of the single hump of

the energy barrier predicted by Proville-EAM. We observed that the correlated kinkpair nucleation occurred at all levels of applied shear stress (below the Peierls stress). This observation contrasts with the approach of Gordon *et al.* [32] who achieved the correlated mode (while employing the Mendelev-EAM) by tailoring the atomistic configurations of the correlated mode. However, they were able to realize the correlated mode only for very low shear stress levels; above a threshold value of 80 MPa, the correlated mode spontaneously transformed to the uncorrelated mode, due to the double-humped energy barrier predicted by the Mendelev-EAM potential.

The atomistic details illustrated in Figs. 5 , 6 and 8 clearly show the correlated kinkpair nucleation and the resulting thermal activation of screw dislocation motion by double superkinks. These results enrich the classical picture of double-kink nucleation, which is supposed to be comprised of only two separated individual kinks (of opposite signs) activated on the glide plane, an example for which is the double kinks formed in Si [67]. In the case of BCC Fe, the compact screw dislocation core is spread into the three $\{1\bar{1}0\}$ planes of the $[11\bar{1}]$ zone, involving three non-parallel $[11\bar{1}]$ columns of atoms. Hence, a unit process of dislocation motion crystallographically necessitates the formation of kinkpairs, where the two individual kinks of a kinkpair lie on two adjacent glide planes instead of being on a single glide plane.

The 3D mode of thermally activated dislocation motion by the nucleation of kinkpairs at high/room temperatures is also in contrast with the 2D picture of dislocation motion by means of split-core states as studied in previous 2D atomistic modeling [21-23]. The 2D split-core states, when extrapolated to 3D, will correspond to the entire dislocation line with a split-core state, akin to the uniformly split-core dislocation line predicted by

Mendelev-EAM (Fig. 2.7(b)). Such a dislocation line with a uniform split-core state is energetically unfavorable because the system energy increases linearly with the length of the dislocation line without limit. Hence, the concept of 2D mode of dislocation motion has less significance with respect to the kinetics of screw dislocations.

We next discuss the major assumptions that we have made in our work and their implications with respect to the results we have obtained in our atomistic and crystal plasticity simulations. First, the vibrational entropy associated with kinkpair nucleation was not directly considered in our estimate of dislocation mobility. The consequence is that the kinkpair activation free energy is approximated by the kinkpair activation energy from NEB calculations. This further means that we did not account for the contribution from the stress dependent entropy while computing the prefactor $\dot{\gamma}_0$. In other words, the Meyer-Neldel compensation law, which would have otherwise predicted a different value for $\dot{\gamma}_0$ by incorporating the stress-dependent entropic contribution into the attempt frequency, is considered negligible in our kinkpair kinetics when the loading range is relatively small [14].

Our second assumption relates to the effect of crystal zero-point vibrations that has been studied recently by Proville *et al*. [33]. They modified the classical transition state theory by including the effect of quantized crystalline vibration modes, and employed these to estimate the yield stress values of BCC Fe that was found to be significantly lower than those predicted by the classical transition state theory, at temperatures lower than 80K. They also observed that, for temperatures above half the Debye temperature (which is around 480K for BCC Fe), the quantum-corrected transition state theory approached the classical transition state theory. Since the current work considers only the

temperature regime in the vicinity of room temperature (say 200K-350K), we choose to neglect the quantum corrections in our atomistic-crystal plasticity model based on the classical transition state theory.

Third, in Eq. (7) of our crystal plasticity model for computing the resolved shear stress, we have neglected any additional terms of non-glide stress accounting for the non-Schmid behavior [25]. This assumption is expected to be physically reasonable because in the room-temperature and low-stress regime, dislocation motion proceeds via kinkpair nucleation and the non-Schmid effects are likely small [30]. The non-Schmid effects are due to both the intrinsic twinning-antitwinning asymmetry of the BCC lattice and the extrinsic effect of stresses on the dislocation core [20, 21, 23]. They were found to be relevant in these 2D molecular statics studies in which the stresses employed were very high, i.e., close to the Peierls stress value. But the thermally activated kinkpair nucleation can occur at much lower stresses that are typically employed in experiments, for which the additional resistance to the dislocation motion due to the non-Schmid effects become less significant. Groger and Vitek have recognized this implication in their study [30] that was based on two modes of dislocation motion in the two characteristic stress-temperature regimes with different saddle-point configurations, i.e., (i) double-kink mechanism in the low-stress and high-temperature regime that was independent of non-Schmid effects; (ii) bow-out mechanism in the high-stress and low-temperature regime [68] that was sensitive to non-Schmid factors. While we agree with their viewpoint on the non-Schmid effects, our NEB modeling reveals a consistent thermal activation mechanism that involves the formation of double superkinks whose distance is stress-

dependent and does not require the division into two stress-temperature regimes with different kinds of saddle-point configurations.

2.5 Conclusions

The major conclusions of this chapter are summarized below.

- We have developed an atomistically informed crystal plasticity framework for BCC Fe single crystal that is in full fidelity with the atomic mechanism of thermally activated dislocation motion via kink nucleation. The nudged elastic band method was used to capture the activation pathway and evaluate the stress dependent activation parameters of kink nucleation.
- Our atomistic results demonstrated a novel *correlated* kinkpair nucleation mechanism for the thermally activated motion of a $1/2\langle 111 \rangle$ screw dislocation, which leads to a single-humped minimum energy path and a single-step activation pathway to the neighboring $\{110\}$ Peierls valley. As a result, the thermal activation of a screw dislocation involves the nucleation of double superkinks, each of which consists of the leading and trailing kinkpairs, in contrast to the classical picture of simple double-kink nucleation. The superkink structure arises from the discrete 3D nature of the saddle-point state of screw dislocation motion in BCC crystals.
- Our constitutive model quantitatively predicted the orientation dependent stress-strain behavior and the temperature/strain-rate dependence of the yield stress, both of which agreed with the experimental results in the 200K-350K temperature

regime; the strong rate dependence was rationalized by the small activation volumes of nucleation of correlated kinkpairs and the resulting double superkinks.

We conclude by noting that our work in this chapter provides an atomistically informed crystal plasticity framework for studying a broad class of BCC metals with the strength/rate-limited mechanism controlled by thermally activated screw dislocation motion. Furthermore, the effects of dislocation-defect interactions, which are central to the topic of irradiated materials [41] and BCC alloys [69], could be incorporated into our modeling framework and thus represent future research directions. Moreover, future studies will consider the atomic mechanism of screw dislocation cross slip and non-Schmid effects in BCC crystals for bridging atomistics to crystal plasticity.

CHAPTER 3

SELF INTERSTITIAL ATOM INDUCED HARDENING AND SOFTENING IN IRRADIATED BCC IRON

3.1 Introduction

The motion of screw dislocation motion is well known to be the strength and rate-controlling process governing the yield in BCC metals [11, 17]. At finite temperatures and low stresses the screw dislocation kinetics is controlled by the thermal activation of kinks [19]. Presumably the thermal activation of kinks can be influenced by the presence of lattice defects like alloying elements and point defects due to irradiation damage, that could modify the activation kinetics of kink nucleation, thus directly affecting the yield of BCC metals. In the case of irradiated BCC metals higher order obstacles like self interstitial loops and voids can also block the dislocations thus contributing to athermal hardening. Whereas, irradiation induced point defects like self-interstitial atoms (SIA) and vacancies could either elastically interact with the dislocations or be accommodated within the dislocation core thus modifying the core structure and thereby affecting the kink nucleation kinetics.

The screw dislocation is primarily a shear induced line defect and there is very limited volumetric strain field associated with it, unlike its edge counterparts [70]. So the dislocation-defect interaction is primarily due to the short-range attractive force on the point defect very near or within the dislocation core, unlike the case of edge dislocation where long-range elastic force controls the interaction with the point defects as espoused

by the classical Cottrell drag theory [70]. This is depicted in Fig. 3.1 that shows the schematics of an edge dislocation and a screw dislocation surrounded by point defects. The edge dislocation (Fig. 3.1(a)) can accommodate the point defects in its elastic field within a long range cut-off radius r_{long}, while the screw dislocation has a short range elastic field due to which the point defects far away from it are unaffected while the ones near to it and within a short-range cutoff radius of r_{short} are attracted and accommodated within its core (assuming that the specific point-defect experiences an attractive force within the dislocation field). For distances very near the core and within the core, the elasticity theory ceases to work. Hence we need atomistic level simulations to probe into the near-the-core and within-the-core effects that could substantially affect the kink nucleation kinetics on the screw dislocation.

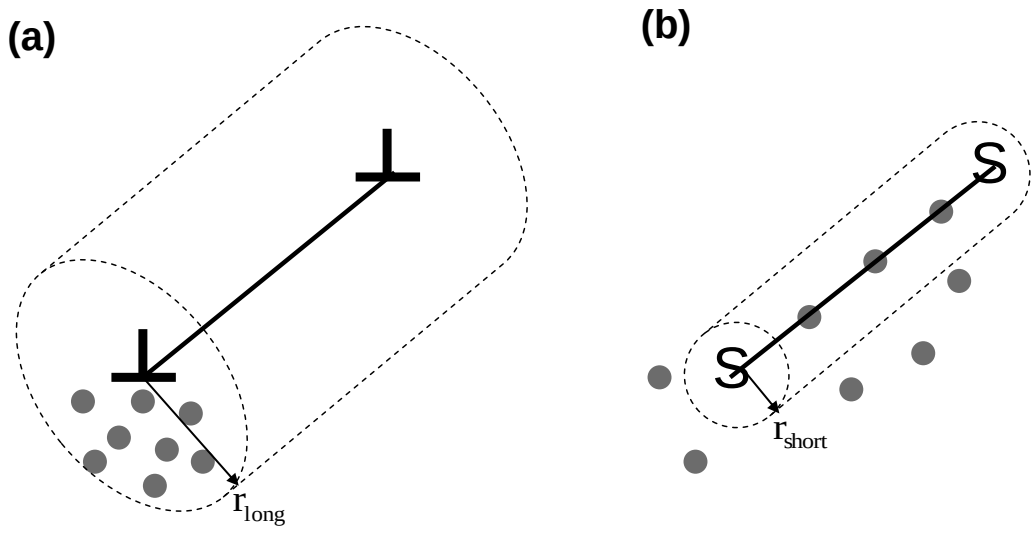

Fig. 3.1 Schematics of the point defects around (a) an edge dislocation and (b) a screw dislocation.

There has been strong evidences from several experimental works in the past, for the yield strengths of BCC metals being affected by point defects and/or alloying elements

(both of substitutional and interstitial types), thereby resulting in hardening or softening behaviors. For example, Caillard [69] reports high temperature hardening, intermediate temperature softening and low temperature hardening of BCC Fe due to carbon interstitials. Okazaki [71] reports high temperature hardening and low temperature softening binary Iron alloys, alloyed with Ni, Mn, and Si. Sato *et. al.* [72] reported the softening of electron irradiated BCC Fe single crystals at low temperatures. Caillard also reports softening in BCC Fe due to low concentrations of Ni, Si and Cr [73] and hardening due to high concentrations of Si and Cr. Though various hypotheses and analytical models have been proposed for the hardening/softening effects in the aforementioned experimental works, there has not been strong evidences from computational studies or unanimous agreements upon the origins of the hardening/softening mechanisms, as has also been acknowledged in [74]. Hence in this chapter, we conduct an atomistic level study of the kinetics of screw dislocation modified by point defects. We choose to limit our study to self-interstitial atoms (SIA) interacting with screw dislocations in BCC Fe for certain reasons. On the first place, we are interested to know the behavior of irradiated Iron, since irradiated metals have a super-saturation of SIA and vacancies that can interact or be absorbed into screw dislocations cores [75] thereby modifying the dislocation kinetics. Secondly, we would like to use the SIA-screw study as the basis for understanding the effects of interstitial and substitutional alloying elements like C, N, H, Ni, Mn and Si in BCC Fe. Thirdly, our work in this chapter is limited to SIA due to the lack of interatomic potentials for BCC Fe, that account for the interactions with the alloying elements. The lack of interatomic potential for BCC Fe, that can predict a single-humped screw dislocation activation energy barrier,

in accordance to density functional theory results [76] has been an outstanding problem in computational metallurgical studies [77]. Though single-humped empirical potentials for pure BCC Fe has been reported recently [33], the potentials accounting for cross-interactions with alloying elements have all been of the double-humped type.

We describe the details of the molecular dynamics and the nudged elastic band simulations adopted in this chapter, in the Section 3.2. It will be followed by a detailed illustration of our results in Section 3.3, followed by discussion and conclusions.

3.2 Methods

We use three-dimensional molecular dynamics (MD) simulation to study the interaction between a/2[111] screw dislocation and a single self-interstitial. The unit processes of interest is extracted from the MD output and fed into a three-dimensional nudged elastic band simulation (NEB), at appropriate stress states. The NEB simulations help us to quantify the thermodynamics and kinetics of the unit processes thus providing mechanistic understanding of the screw-SIA interaction. The details of these computational methods are discussed below.

3.2.1 Molecular dynamics simulations

The simulation set up employed in our MD simulations is as shown in Fig. 3.2 and is similar to the one employed in Chapter 2 to study the screw dislocation motion. A screw dislocation is embedded in the center of a simulation of cell of whose x, y and z axes are oriented along the $[111]$, $[\bar{1}01]$ and $[\bar{1}2\bar{1}]$ directions, respectively. The simulation

supercell is 54 nm long along its out-of-plane [11$\bar{1}$] direction and its in-plane dimensions are 25nm and 25nm, respectively. The 1/2[111] screw dislocation is created at the center of the supercell by superimposing its elastic displacement field and subsequently relaxing the supercell with conjugate gradient method to obtain the minimum energy state.

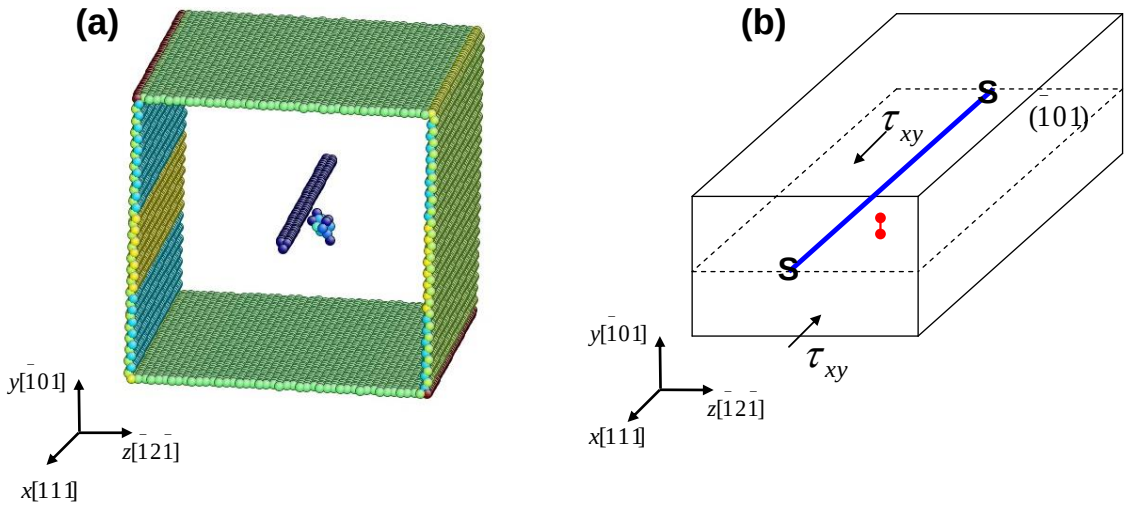

Fig. 3.2 Atomistic simulation set-up. (a) 3D perspective view of the supercell and the dislocation and the SIA near it, colored by centro-symmetry parameter [51]. **(**b**)** Schematic of the supercell showing details of the loading scheme.

The outermost $(\bar{1}01)$ and $(\bar{1}2\bar{1})$ planes constituting the in-plane boundaries are traction free and hence fully relaxed so as to avoid the effect of stresses perpendicular to the glide direction. The shear stress required to move the dislocation is exerted by imposing a displacement-controlled boundary condition on a thin boundary layer of $(\bar{1}01)$ face, while the bottom boundary layer is held fixed. The dislocation glides on the maximum resolved shear stress plane (MRSSP), which is the $(\bar{1}01)$ plane for our setup. An SIA is introduced in the $(\bar{1}01)$ glide plane so as for the dislocation to interact with it as it approaches the SIA. The SIA rests in equilibrium in a [110] dumbbell configuration

[Was, Erin]. We observe that there is an attractive field of interaction between the dislocation core and the SIA within a cutoff radius of 4-5 lattice constants. And within this cutoff distance the interaction is always attractive irrespective of the relative orientation of the dislocation-burgers vector and the dumbbell axis of the interstitial. This is in accordance with the 2D studies of screw dislocation-SIA interaction done in the past [75]. In this chapter, all the atomic configurations are colored by the centro-symmetry parameter for showing the core structure of the screw dislocation and the SIA.

3.2.2 Nudged elastic band method

As in Chapter 2, we use LAMMPS software [52] to perform the 3D NEB calculations. Results were rigorously verified using an in-house NEB code. The initial and the final states for the NEB simulations are obtained from the MD simulations. The energies of the initial and the final configurations are minimized using conjugate gradient method, so as to relax them in the local minimum states of the 3D energy landscape. The intermediate states or replicas are generated by linearly interpolating between the atomic coordinates of the initial and final states. All the replicas are interconnected with springs that exert inter-replica forces, so as to rearrange the replicas equidistantly along the minimum energy path. The climbing image algorithm [53] is used to locate the saddle point of the energy barrier. A force tolerance of 0.01 eV/$\mathring{A}$ is employed to check the convergence of the NEB simulation. For NEB simulations at finite stresses, the initial and final configurations were maintained at similar shear-stress levels by holding constant the finite-displacement of the surface layer.

3.2.3 EAM potential

In this study we employ the EAM potential for BCC Iron by Proville *et al.* [33]. This potential has the unique advantage over the other EAM potentials of the past that it predicts a single-humped activation energy barrier for screw dislocation motion via kink nucleation. The single-humped barrier results in a physically realistic correlated kinkpair nucleation process [77] unlike the physically unrealistic uncorrelated mode predicted by potentials in the past [32]. Apart from this feature this potential also predicts a non-degenerate screw dislocation core both of which are consistent with DFT results [36, 37].

3.3 Results

3.3.1 Three-Kink structure

Our MD simulations showed frequent dynamic events of the SIA getting adsorbed into the core of the screw dislocation. The adsorption events were usually followed by the removal of the SIA from the core so as for the dislocation glide to proceed under the applied load. There is a high degree of randomness in these events since depending on the resolved shear stress levels and temperature, the dislocation could 'spit out' more than one interstitials (in the form of interstitial loops) along with vacancies [78]. Since we are primarily interested in the motion of dislocation after it absorbs an SIA, we compute the minimum-energy configuration of the screw dislocation with the SIA in its core using conjugate gradient minimization scheme. It was observed that an SIA in the dumbell configuration outside the dislocation core, was adsorbed and accommodated into the core by switching itself into a $[1\bar{1}1]$ crowdion configuration. The $[1\bar{1}1]$ crowdion could be

accommodated into any of the three atomic columns forming the core of the dislocation, the details of which will be discussed in the subsequent sections.

Fig. 3.3(a) shows the pure screw dislocation line of the a/2 [111] type, with a uniformly pure core before the adsorption of the SIA and Fig. 3.3(b) shows the screw dislocation line after the adsorption of the SIA. The coloring is based on the centro-symmetry parameter. It can be observed that the post-adsorption configuration of the dislocation has several atomic size kinks on it that spread the dislocation core out of its Peierls valley and collectively impose a curvature to the dislocation line in the 3D space. To understand the details of the core-spreading due to the individual kinks and the 3D geometry of the post-adsorption dislocation line, we plot the Differential Displacement (DD) diagram of the dislocation core at various points along its line. These points are marked in Fig. 3.3(b) and the DD plot corresponding to each point is shown in Fig. 3.3(c-g). Fig. 3.3(c) shows the non-degenerate and three-fold symmetric dislocation core at point c. This core state is usually termed as the 'compact core' state. Note that the pure dislocation of Fig. 3.3(a) has this same compact core structure throughout its length. The center of the compact core is marked by a red dot. In Fig. 3.3(d) it can be seen that the core is spread onto the $(\bar{1}01)$ plane and Fig. 3.3(e) shows that the core is back in its compact state but shifted by one lattice distance along the $(\bar{1}01)$ plane.

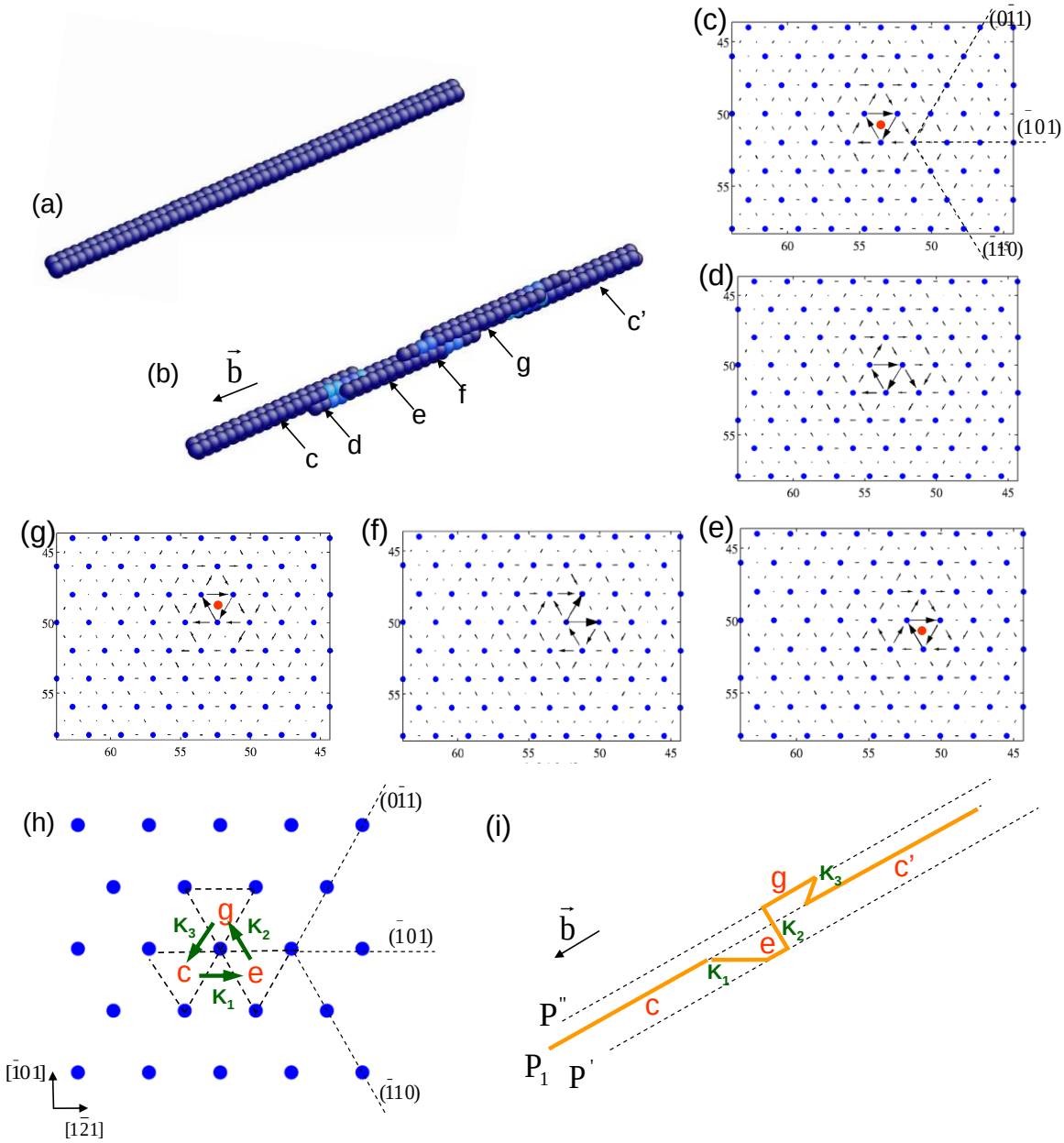

Fig. 3.3 Differential displacement plots and the 3-kink dislocation structure. (a) Pure screw dislocation at its energy minimum state. (b) Screw dislocation after the absorption of SIA, at its energy minimum state. (c-g) DD plots of the dislocation core at various points along the dislocation line, as marked in Fig. 3.3(b). (h) Schematic showing the compact core states of the 3-kink dislocation line in three different Peierls valleys. (i) A 3D schematic showing the structure of the 3-kink dislocation line.

Thus the two atomic size kinks in Fig. 3.3(b) between points c and d, denote a single kink that spreads the core along the $(\bar{1}01)$ plane. Similarly it can be seen that, between points e and g, the core is spread along the (inclined) $(\bar{1}10)$ plane, that involves a second kink along the $(\bar{1}10)$ plane. The next point along the dislocation line is c' and is in the same Peierls valley as the point c (its DD plot will be same as the for the point c). Hence that denotes the involvement of a third kink along the $(0\bar{1}1)$ plane, connecting between the compact core states at points g and c', respectively. We choose to name the post-adsorption state of the dislocation can as a '3-kink dislocation', owing to the presence of the three kinks that collectively deform the dislocation structure.

This sequential core-spreading across the three inclined $\{110\}$ planes, as induced by the presence of SIA in the dislocation core, can be better understood from the schematics in Fig. 3.3(h & i). Fig. 3.3(h) consolidates the compact core states at points c, e and g, and the intermediate spread-core states as show in Fig. 3.3(c-g) onto a single figure. The kinks connecting these three compact states are denoted as K_1, K_2 and K_3 respectively. The essential message from this schematic is that the dislocation core is spread across three neighboring Peierls valleys, connected by atomic size kinks. The schematic in Fig. 3.3(i) shows the 3D depiction of the core-spreading and the kinks associated with the 3-kink dislocation. The dislocation before the adsorption of the SIA lies in the Peierls valley denoted as P_1 and after adsorbing the SIA, spreads locally into the neighboring Peierls valleys P' and P'' and spreads back to P_1, with the help of the kinks K_1, K_2 and

K_3. It is very important to note that the kinks K_1, K_2 and K_3 are not thermally activated kinks, but are instead structurally induced ones, due to the super-position of the strain field of a [1 1 1] crowdion onto that of the [1 1 1] screw dislocation.

It can be presumed that the kinetics of the motion of a 3-kink dislocation could be significantly different from that of a pure dislocation, owing to the local differences in the core structure. It can also be conjectured that, irradiated BCC Fe could contain a high density of the 3-kink dislocations, the motion of which could then be the strength-controlling step of plastic flow, as opposed to the motion of pure dislocation lines as in non-irradiated BCC Fe. This possibility necessitates the evaluation of the activation energy for the motion of 3-kink dislocations, which we will be discussing in the section to follow.

The 3-kink dislocations have not been experimentally visualized yet. In the *in situ* TEM studies of dislocations in BCC Fe by Caillard [59, 69, 79] that track the detailed motion and line structure of the dislocations, the resolution was not sufficient enough to visualize presence of atomic size kinks on the dislocation line. Also worth noting is that the 3-kink dislocation resulting from the adsorption of SIA into the screw dislocation core was predicted by Makii *et. al.* [80] who simulated BCC Fe using a Finnis Sinclair potential. But they were not able to obtain the detailed reaction kinetics of the motion of such 3-kink dislocations and/or compare it with pure-dislocation motion. We next discuss the reaction-kinetics of the 3-kink dislocation, obtained via 3D NEB studies.

3.3.2 Reaction pathway for the motion of 3-kink dislocation

We employed 3D NEB calculations for the simulation setup show in Fig. 3.2 towards obtaining the reaction pathway for the unit step of motion of the 3-kink dislocation. Fig. 3.4(a) shows the converged minimum energy path (MEP) for the unit process of thermally activated motion of the 3-kink dislocation at an applied resolved shear stress of 300 MPa. The energy of the replicas is plotted against the reaction coordinate that is defined as the normalized path length of the minimum energy path. The atomic configurations of the replicas are shown in Fig. 3.4(b) as their $[\bar{1}01]$ projections and are numbered accordingly. Replicas 1 and 22 respectively are the initial and the final states of the unit process. It can be seen from Fig. 3.4(b) that the initial replica is the 3-kink dislocation and the final replica is a pure dislocation (without any structural kinks) and the SIA separated from the dislocation core. This shows that the unit process of 3-kink dislocation motion involves the de-pinning of the screw dislocation from the SIA. The $[\bar{1}2\bar{1}]$ projection of the atomic configuration of the final state (replica 22) is shown in Fig. 3.4(c). In the figure, the atom sizes are arbitrarily reduced so as to be able to visualize the SIA near the core. It can been that the SIA exists in the dislocation strain field in the dumbbell configuration with its dumbbell axis oriented along the $[011]$ direction.

It should be noted that the MEP shown in Fig. 3(a) is at a resolved shear stress level of 300 MPa. Below 300 MPa, the thermally activated motion of the 3-kink dislocation is not thermodynamically favorable. This implies that the SIA atom in the dislocation core has a strong pinning effect. The salient feature of the MEP for the motion of 3-kink dislocation is the presence of two energy barriers marked as E_1 (0.26 eV) and E_2 (0.58 eV) respectively, in Fig. 3.4(a&b). These two energy barriers denote two separate atomic processes involved in the motion of 3-kink dislocation.

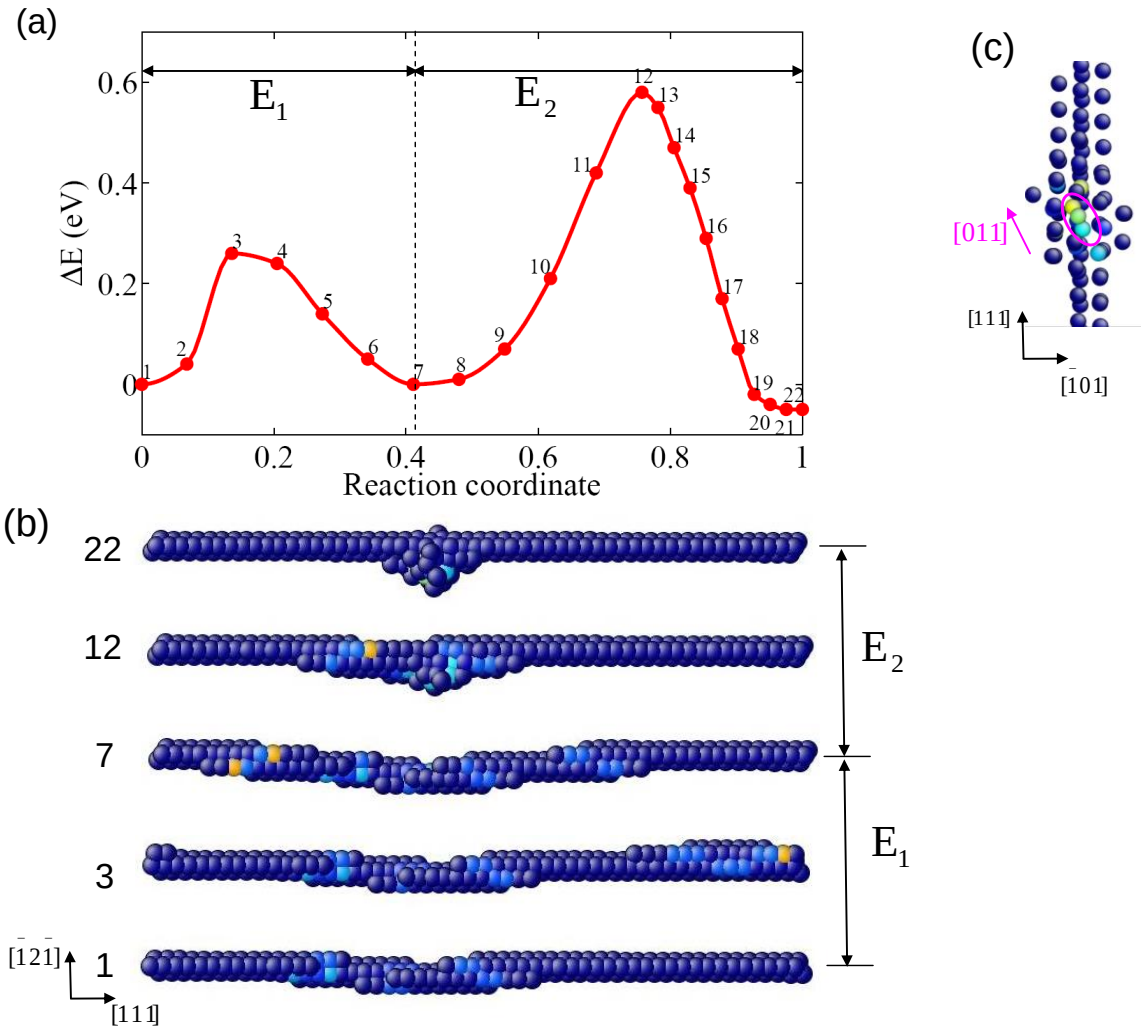

Fig. 3.4 3D NEB results of thermally activated motion of the 3-kink dislocation at 300 MPa. (a) Minimum energy path for the 3-kink dislocation motion involving kink nucleation and stress-assisted de-pining. (b) Atomistic configurations of the corresponding replicas along the minimum energy path. (c) The $[12\bar{1}]$ projection of the replica 22 of Fig. 3.4(a&b).

These can be better understood from Fig. 3.5. which shows the schematics of the atomic configurations of the NEB replicas of Fig. 3(b), in a perspective view.

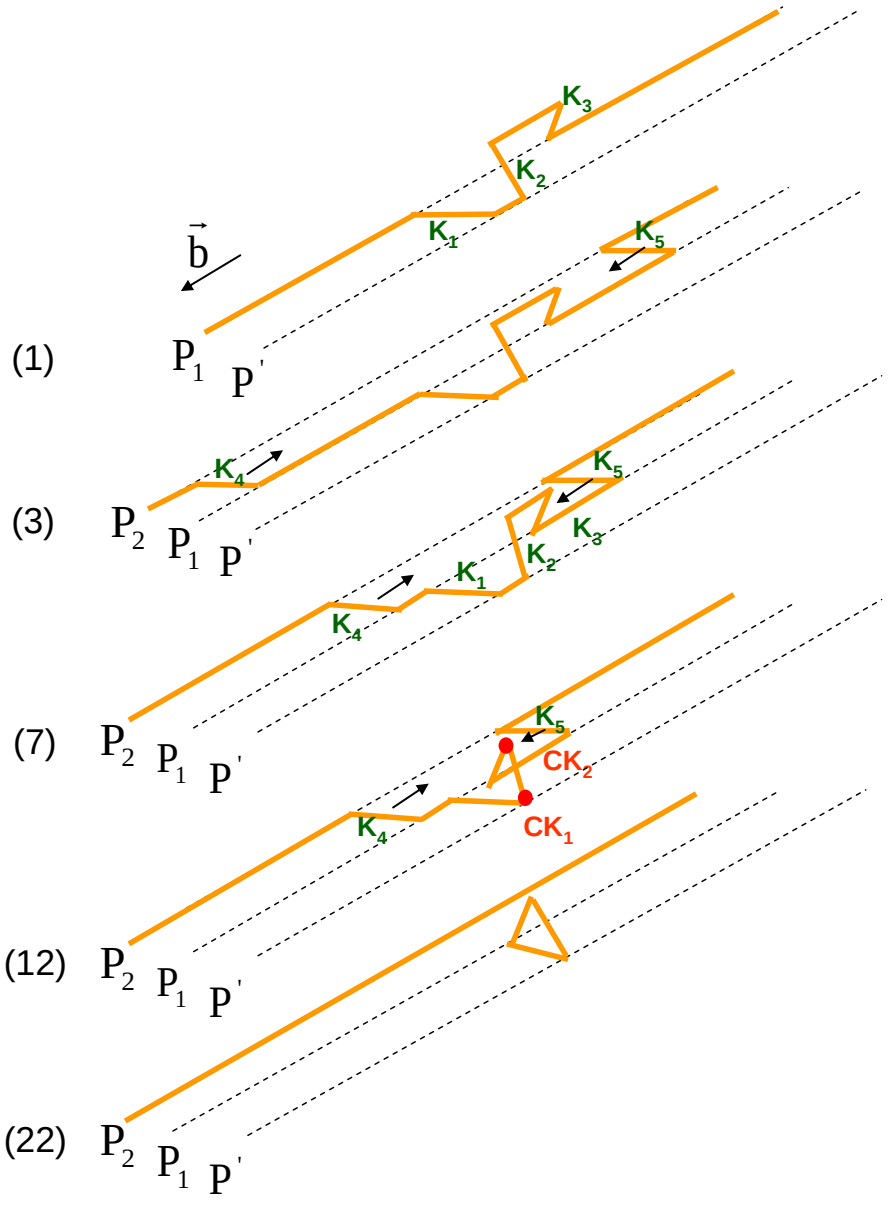

Fig. 3.5 Schematics of the 3-kink dislocation motion. The number in brackets on the left side of each schematic figure corresponds to the replica on the MEP of Fig. 3.4(a&b).

The initial state is the 3-kink dislocation, containing the three structural kinks K_1, K_2 and K_3 and occupying two Peierls valleys P_1 and P' on the $(\bar{1}01)$ plane, as already depicted in Fig. 2(i). The first activation energy barrier E_1, involves the nucleation of a thermal double-kink whose individual edge segments are denoted by K_4 and K_5 in the replica 3.

These kinks spread the core into the next Peierls valley, P_2, as marked. (It should be noted that the usage of the term 'double-kink' is for the sake of simplicity. From an atomic perspective, a single double-kink is a 'correlated double kinkpair' containing four individual kinks, due to the atomic level discreteness of the lattice and the unique core structure of the dislocations in BCC metals. This has been discussed in detail in [77]. The applied shear stress drives K_4 and K_5 towards each other. Also the short screw segments between the structural kinks K_1, K_2 and K_3 are annihilated, forcing these kinks to interact together. Since these kinks lie on three different $\{110\}$ planes they have repulsive interaction between each other and thus cannot annihilate. Thus they interact to form pinning points as marked by red dots in replica 12. These kinks on different planes interacting to form pinning points are called *cross kinks* following Louchet *et. al.* [81] and Marian *et. al.* [78]. The cross kinks observed by Marian *et. al.* were formed from the nucleation and interaction of 'thermal' kinks on different $\{110\}$ planes, while the ones in this work are structural kinks formed from the accommodation of SIA in the dislocation core. With sufficient applied stress, the three kinks forming the cross kink can be squeezed against each other to form a closed circuit and the thermal kinks K_4 and K_5 can annihilate each other. This process is what is denoted by the second energy barrier, E_2. Thus the dislocation advances fully into the new Peierls valley, P_2, while the SIA is left behind. The motion of the 3-kink dislocation, hence involves the de-pinning of the dislocation from the SIA. Understandably at 300 MPa, E_2, which is the energy required to de-pin by squeezing the kinks together, is higher than E_1, which is the energy for kink nucleation.

The alternative possibility for the dislocation and the SIA (within the core) to move together in a concerted fashion is not energetically feasible, because of the difficulty in moving the kinks K_2 and K_3 (both of which are not in the $(\bar{1}01)$ plane) conservatively in the $(\bar{1}01)$ glide plane.

3.3.3 Stress-dependant activation energy

We repeated our NEB calculations for varying levels of applied shear stress in order to explore the stress dependence of the activation energy for the motion of 3-kink dislocation. The corresponding MEPs are plotted in Fig. 3.6(a). It can be observed that, as the stress is increased the MEP gets tilted downwards and the activation energy values are reduced. The MEPs can be divided into two sets depending on the stress levels and the relative heights of the two energy barriers. For the MEPs drawn in solid lines (applied shear stress between 300 and 500 MPa) E_2 is higher in magnitude than E_1 which implies that the rate-limiting barrier for the dislocation motion is E_2, i.e., the squeezing of the kinks to produce the SIA. But for the dotted MEPs (applied shear stress between 600 and 800 MPa), there is a switching of the rate-limiting barrier into E_1, as the magnitudes of E_1 are higher than those of E_2. It means that at higher stresses the rate-limiting barrier is that for the kink nucleation.

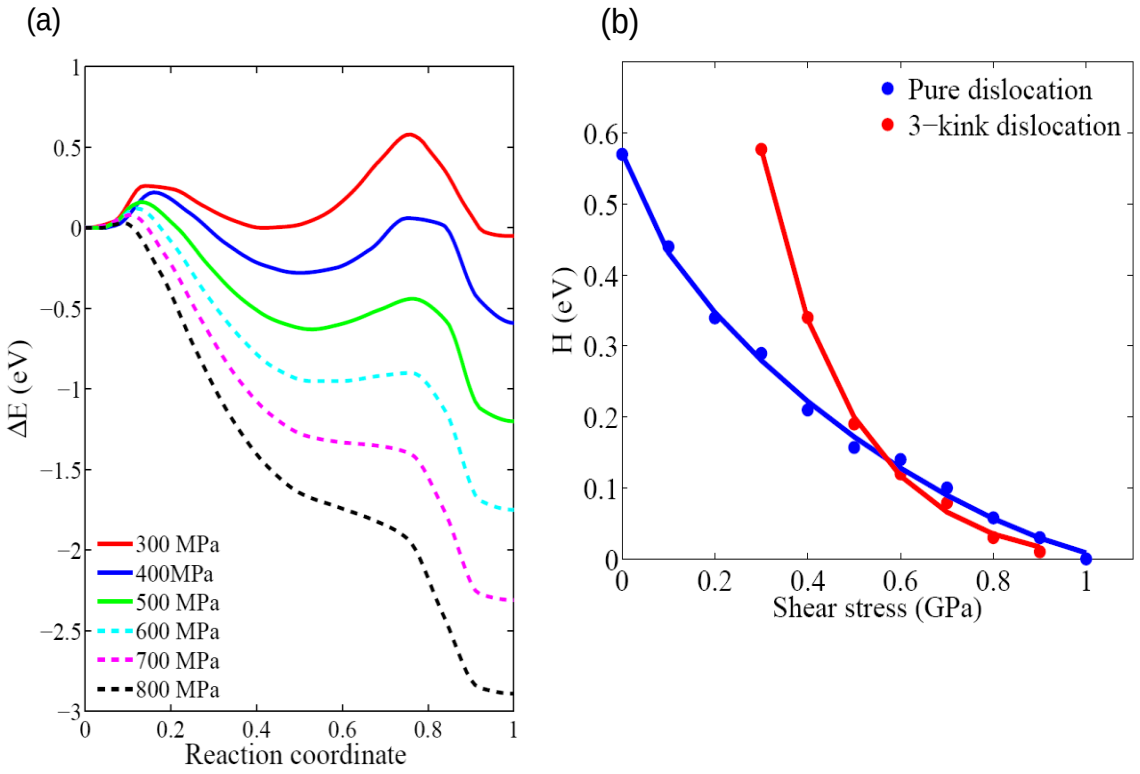

Fig. 3.6 Shear stress-dependent minimum energy path (MEP) and activation energy. (a) MEPs for the motion of 3-kink dislocation at finite shear stresses. (b) Data points of calculated activation energy versus shear stress compared with that for the pure dislocation motion, obtained from [77].

This trend can be better understood from Fig. 3.6(b) in which the rate-limiting activation energy values (or the saddle point values), are plotted against the applied shear stresses and compared with the corresponding curve for a pure dislocation [77]. As discussed before, it can be assumed that in irradiated BCC Fe specimens, the screw dislocations in their ground state must have localized 3-kink structures due to the absorption of SIA into the cores. Hence the strength and rate controlling mechanism of plastic deformation in irradiated specimens should be the movement of 3-kink dislocations rather than pure screw dislocations. In other words, the reaction kinetics of the 3-kink dislocation can be assumed to reflect the yield of irradiated specimens and that of the pure screw dislocation

should reflect the yield of un-irradiated specimens. Fig. 3.6(b) shows that for the low stress regime $(300\text{MPa} \le \tau \le 500\text{MPa})$ the activation energy values for the 3-kink dislocation is higher than those for the pure dislocation, denoting hardening of irradiated specimen with respect to the un-irradiated specimen. For the high stress regime $(600\text{MPa} \le \tau \le 900\text{MPa})$ the activation energy values are smaller than those for the pure dislocation, denoting a softening effect. The transition from hardening to softening that occurs at around a shear stress of 580 MPa, is due to the switching of the rate-limiting atomistic mechanism from de-pinning via kink collisions to kink nucleation.

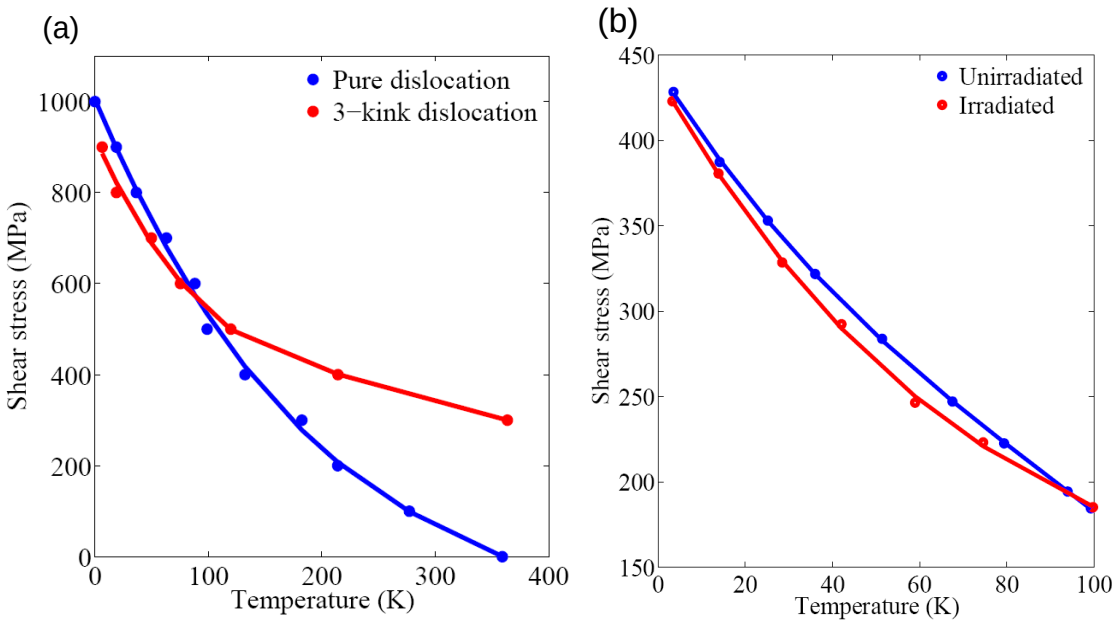

Fig. 3.7 Yield stress as a function of temperature. (a) Comparison of pure dislocation motion with that of the 3-kink dislocation motion. (b) Comparison of un-irradiated samples with irradiated samples, as obtained from [79].

The activation energy Vs shear stress relationships can be analytically converted to shear stress Vs temperature relationships as described in [77] so as to compare with experimental results for the same. The result is as shown in Fig. 3.7(a). It can be observed that, in the high temperature (and low stress) regime the effect of irradiation is hardening

and at low temperature (and high stress) regime, the effect is softening. The transition temperature at which softening disappears and hardening sets in is around 90 K. Irradiation induced softening at low temperatures has been reported in experimental works of the past [72, 76, 82, 83]. The low-temperature softening observed by Sato *et. al.* is depicted in Fig. 3.7(b). They observed that the electron-irradiated samples exhibited lower yield strengths than the un-irradiated samples, in the low temperature regime of 4-90K.

3.3.4 Reaction pathway for the absorption of SIA into the screw dislocation core

It has been illustrated in Section 3.3.1 that the SIA is absorbed into core of the screw dislocation to form the 3-kink dislocation. It is important to estimate the reaction pathway for this absorption process so as to estimate the probability for the formation of 3-kink dislocation structures in irradiated metals. Towards this purpose, we isolated the initial and the final states of the unit process of the SIA-absorption event from our MD simulations and employed these configurations in our nudged elastic band simulations. The reaction pathway obtained for zero stress is shown in Fig. 3.8(a). Figure 3.8(b) shows the initial and the final states. The initial state (replica 1) is the screw dislocation with the SIA in its strain field, positioned at one lattice distance away from the core and the final state is the 3-kink dislocation. Fig. 3.8(c) shows the details of the SIA in the initial state. It can be seen that the SIA exists in the dumbbell configuration with its axis oriented along the $[0\bar{1}1]$ direction. It can be intuitively observed that the initial and the final states of this SIA absorption unit process are in fact respectively equivalent to the final and the initial states of the 3-kink dislocation glide unit process (as in Fig. 3.4). The activation energy for the absorption process is 0.30 eV which is the energy expended in squeezing

in the SIA into the dislocation core, resulting in the formation of the 3-kink structure. This activation energy is smaller than that for the glide of a screw dislocation by kinkpair nucleation at zero stress which is equal to 0.57 eV from Fig. 3.6(b).

This means that there is high probability for the SIA to get absorbed into the screw dislocation core, forming the 3-kink dislocation structure and hence the strength-controlling process in irradiated metals could be the motion of 3-kink dislocation and not the pure screw dislocation. Also the energies of the initial and final states for the absorption process differ by around 1.8 eV (for zero applied stress), which denotes that the SIA-absorption process leading to the 3-kink structure is strongly favorable thermodynamically, though there is a kinetic barrier to be overcome.

3.4 Discussion

In this section we will discuss the implications of the major results of the work in this chapter.

One of the key results of this work is the prediction of the 3-kink dislocation structure. The plastic deformation of BCC metals is considered to be controlled by the motion of screw dislocations and most of the computational studies in the past have concentrated on the motion of pure dislocations [31, 33, 77, 78]. In this work we show that the intrinsic core structure of the dislocation can be heavily modified by point defects or alloying elements.

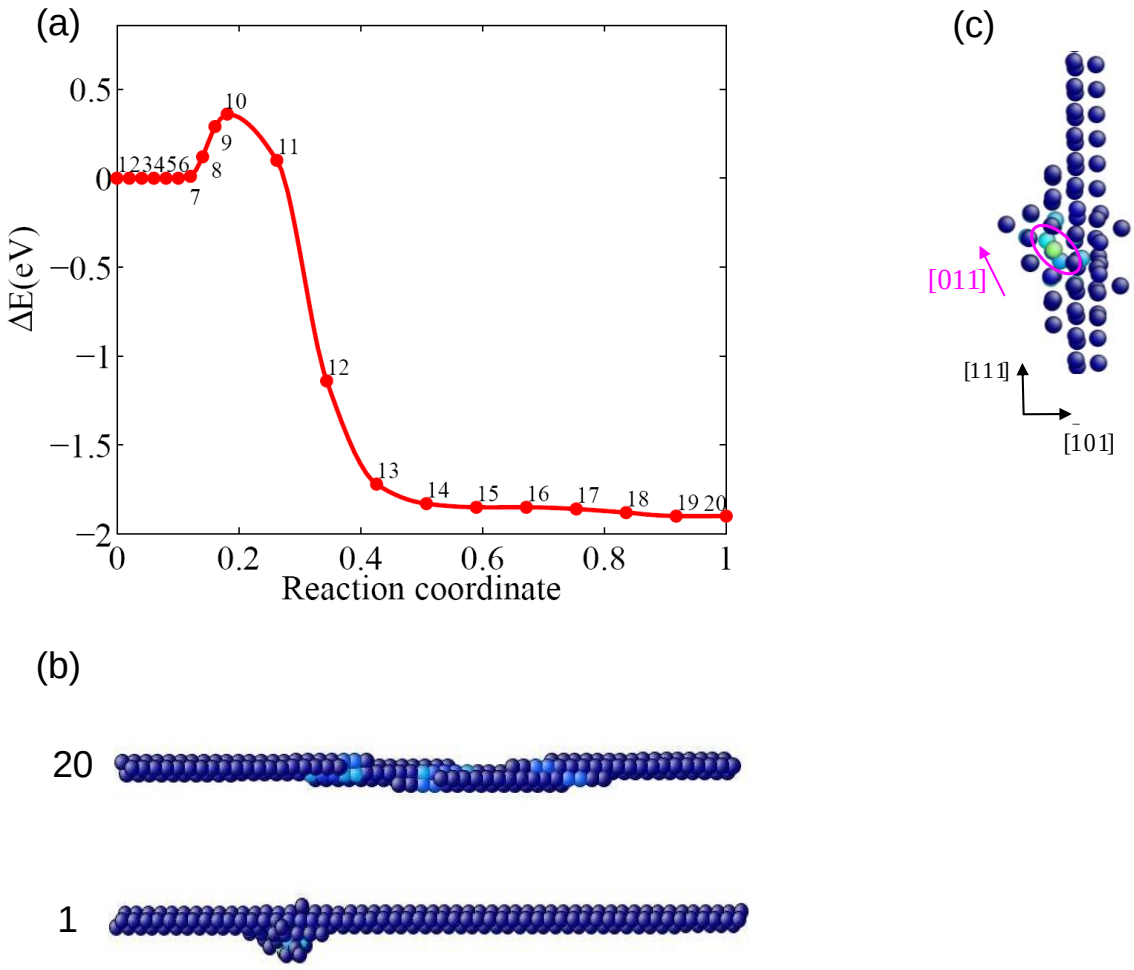

Fig. 3.8 3D NEB results for the unit process of absorption of SIA into the dislocation core. (a) Minimum energy path. (b) Atomistic configurations of the initial and the final replicas on the minimum energy path. (c) The $[1\bar{2}1]$projection of the final replica of Fig. 8(a).

And the dislocation with the modified core structure can have significantly different kinetics than the pure dislocation. Hence any study of dislocations in non-pristine metals should take into account the effect of the impurities on the dislocation kinetics.

The results of our work have strong implications with respect to the hardening and softening effects due to alloying elements in BCC Fe. Our results show that point defects and hence alloying elements with attractive interaction with he screw dislocation (due to

both elastic and chemical effects) can in general pin the dislocation to the lattice thus contributing to hardening at low stresses (i.e. at high/room temperatures). At higher applied stresses (low temperatures) the dislocation can de-pin from the point defect or alloying element, which manifests as softening in the low temperature regime. This stress-assisted de-pinning and softening can not only explain the softening due to irradiation [72] but also can provide a very sound physical reason for the low temperature softening observed in binary Iron alloys [71].

At the same time we would like to note that, the unit process studies in this work is limited to the case of a single SIA interacting with the screw dislocation. A more detailed set of simulations and analysis will be required to estimate the effect of a field of SIA distribution on the dislocation kinetics. The magnitudes of hardening and softening due to a single SIA will presumably be quite different from those due to a field of SIA atoms. This can found to be true from the concentration dependent solid solution hardening of BCC Fe due to Si, as reported in [74]. Even though the magnitudes could be different, the fundamental stress-dependant kink nucleation and de-pinning mechanisms should be the same, irrespective of the concentration of the point defects or alloying elements. Also the effects of other irradiation induced hardening obstacles like self-interstitial loops and voids need to be accounted while explaining irradiation hardening by comparing the kinetics of pure screw dislocation and the 3-kink dislocations. In the current work, we have not taken the effects of these higher order obstacles into account as it is beyond the scope of this work.

Also, the SIA is the biggest interstitial atom possible in BCC Fe and hence forms the upper limit for the size of interstitial atoms that can be accommodated within the screw dislocation core. All other interstitial atoms like C and N, are smaller than the SIA and we conjecture that their pinning effects and hence the subsequent stress-dependent hardening/softening effects, could be lesser in magnitude than that due to SIA. At the same time the chemical effects due to the interaction between the host lattice atoms and the foreign interstitial (or substitutional) atoms could also modify the hardening/softening effects due to the latter. These conjectures can be verified with the availability of appropriate empirical potentials in future that can accurately account for the interactions between the foreign interstitial atoms and the host lattice atoms (BCC Fe, in our case).

3.5. Conclusions

The major conclusions of this chapter are summarized as below.

- We have demonstrated that a screw dislocation in BCC Fe can accommodate a SIA within its core, resulting in the formation of a specific dislocation structure called 3-kink dislocation structure that is locally spread into three Peierls valleys.
- The kinetics of the 3-kink dislocation is computed by 3D nudged elastic band calculations and comprises of two energy barriers each respectively denoting kink nucleation process and stress-assisted de-pinning process. This is in contrast to the single energy barrier for the motion of a pure screw dislocation.
- The comparison of the stress-dependent activation energy curves for the pure screw dislocation and the 3-kink dislocation reveal high temperature hardening and stress-assisted low temperature softening of the single crystal, that is in accordance to experimental results.

As a final note we would like to mention that our study provides a solid framework for analyzing thermally activated crystal plasticity mechanisms involving point defects and dislocations and can be easily applied to the study of a broad class of problems involving the interaction of dislocations with alloying elements and other impurities, which has been of significant practical interest in metallurgical research. The applicability of our study to newer problems of interest is nonetheless pivoted strongly on the development of accurate inter-atomic potentials, which will be the direction of our future research.

CHAPTER 4

DEFORMATION INDUCED FORMATION OF STACKING FAULT TETRAHEDRA UNDER NON-IRRADIATED CONDITIONS

4.1 Introduction

Plastic deformation in metals and alloys is governed by the generation and evolution of defects of point, line, plane and volume types [84, 85]. Among these defects, stacking fault tetrahedra (SFT), bounded by stacking faults (SFs) and stair-rod dislocations, are a peculiar type of volume defect typically found in face-centred cubic (FCC) crystals with low stacking fault energy [84, 86]. Generally, SFT can be introduced by three methods, *i.e.* quenching, high-energy particle irradiation and plastic deformation [86-91]. In 1959, Silcox and Hirsch [87] first observed SFT in quenched gold (Au). They proposed that SFT were formed from the Frank dislocation loops generated by collapsed vacancy clusters, which further dissociated through the Silcox-Hirsch mechanism [84, 87] to produce the three-dimensional (3D) SFT. Since then, extensive studies have been conducted on the vacancy-originated SFT in quenched, irradiated, or plastically deformed bulk FCC crystals [86-107]. However, whether the SFT can be possibly initiated by dislocations without the aid of vacancies remain largely unexplored. If possible, how do SFT form, migrate and annihilate, particularly at the nanoscale regime?

It is well known that the smaller tends to be stronger [108, 109] and the free surface in nano-sized crystals acts as an effective source of dislocations [110-112]. However, surface nucleation only leads to a weak size effect on the strength of

nanocrystals [110, 113], e.g., the predicted logarithmic scaling of strength versus nanopillar/nanowire diameter, as opposed to the measured power law scaling. Hence, the widely-observed size effect is generally believed to arise from dislocation interactions inside nanocrystals. Moreover, the study of plasticity in nanocrystals has until now been focused on one-dimensional (dislocation) and two-dimensional (grain boundary) defects [29, 110-112, 114, 115]. It remains unclear if higher order defects, such as the 3D volume defect of SFT, can be generated inside the confined volume of nanocrystals by pure mechanical deformation. Furthermore, since the sources of partial dislocation are abundant at the surface [110-112], they might facilitate the interactions between partials and SFT in the small volume of nanocrystals. It is thus expected that the dynamic evolution of the SFT might be uniquely mediated by SFs in the nanoscale regime. However, due to technical difficulties in controlling the samples at the nanoscale, it has been a challenge to directly explore the dislocation interaction, as well as the formation and evolution of higher order defects, in small-volume nanocrystals.

In this chapter, we report the first direct visualization of the formation and evolution of the deformation induced SFT via dislocation interactions during *in-situ* tensile testing of Au nanocrystals with high resolution transmission electron microscopy (HRTEM). Aided by large scale molecular dynamics (MD) simulations, we show that the SFT can be produced in nanocrystals directly through dislocation interactions. The presence of vacancies that is critical for the initiation of SFT in the bulk is no longer a pre-requisite for the SFT formation in the nanoscale. We hence term the SFT formed in the nanocrystals as 'dislocation-originated' SFT, specifically due to its origin being solely controlled by dislocation interaction events. Our finding, to our knowledge, is the first

ever instance of SFT formation reported in the nanoscale regime. Moreover, we observe the migration and annihilation of the dislocation-originated SFT, which are proved to be a direct outcome of dislocation-SFT interactions.

4.2 Methods

4.2.1 Sample Preparation and *In-Situ* Tensile Deformation

The Au nanowires were synthesized by the method reported in a recent publication [116]. The growth direction of as-synthesized Au nanowires is along the [111] direction, with few TBs parallel to the cross section of nanowires. The tensile experiments were performed inside a FEI Tecnai F30 field emission gun TEM equipped with a Nanofactory TEM-scanning tunnelling microscope (STM) system. A charge-coupled device (CCD) camera was used to record the images and videos at 2 frames per second. The Au nanowires were attached to an Au rod with silver paint, serving as one end of the Nanofactory TEM-STM platform. A piezo-controlled Au STM probe was used as the other end of the platform. During experiments, the Au nanowires were tilted into the $[1\bar{1}0]$ zone axis and loaded along the [111] direction. Before tensile testing, the Au probe was connected with an Au nanowire by amorphous carbon deposition at the contact area to form a strong contact. Moreover, several samples with [111] or other loading directions were made by cold-welding, same as the method used in by Zheng *et al*. [111]. During the cold-welding process, the forward speed of the piezo-controlled Au STM probe is about 1~2 nm/s, while the linear size of the deformation-affected volume by cold-welding is about 10 nm, thus the strain rate of the cold-welding process is estimated to be on the order of 0.1 s^{-1}. Subsequently, the tensile deformation was conducted by

retracting the Au probes with the estimated strain rate of 10^{-3} s^{-1}. The method for determining the dislocation types in HRTEM images has been discussed by Zheng *et al.* [111].

4.2.2 MD Simulations

Three-dimensional MD simulations were carried out using LAMMPS [117]. We use the Embedded Atom Method (EAM) potential developed by Grochola *et al*. [118] to account for the many-body interactions between Au atoms. The Au nanowires simulated are aligned along the [111] direction, along which periodic boundary condition is applied. The nanowires are geometrically cut in double conical shape of length 28.26 nm instead of perfectly cylindrical ones; the diameters of the largest and smallest cross sections are 6 nm and 4 nm, respectively. This is done with the motivation of utilizing the stress concentration at the neck to promote sequential dislocation nucleation events instead of a large number of simultaneous nucleation events as would otherwise be observed in perfectly cylindrical single-crystal specimens. The nanowires are simulated with temperature T = 1K and loaded at a constant strain rate of 10^{7} s^{-1}. The SFs are visualized by coloring the atoms based on the centro-symmetry parameters [51]. To study the size effect, MD simulations are also carried out on a larger Au nanowire with the diameters of the largest and smallest cross sections being 10 nm and 6 nm, respectively. The generality of the SFT formation mechanism is verified by MD simulations of Cu nanowire. The simulation methodology and the geometry of the Cu nanowire are similar to those of Au nanowires. A recent EAM potential is used for Cu [119].

4.3 Results

4.3.1 Formation of Dislocation-originated SFT by Dislocation Interactions

Figure 4.1 shows the formation of a dislocation-originated SFT through the interactions of partial dislocations in an Au nanowire. The Au nanowire is 16 nm in diameter and contains a growth twin boundary (TB). It is loaded along the $[111]$ direction and viewed along the $[1\bar{1}0]$ direction (Fig. 4.1(a)). During tensile deformation, the partial dislocation typically nucleates from the free surface and moves into the Au nanowire (Fig. 4.1(b)), which is consistent with our previous experimental observations [111, 112]. It is observed that several SFs nucleate sequentially at different sites of the free surface. They glide on the equivalent, inclined $\{111\}$ planes (denoted as SF_1, SF_2 and SF_3, respectively) and interact with each other inside the Au nanowire, forming a wedge and then a zigzag dislocation structure (Fig. 4.1(c-d)). Such interactions between the SFs are the first step of the formation of dislocation-originated SFT. As the tensile load increases, SF_3 starts to move and eventually annihilates at the free surface, leaving behind a wedge structure between SF_1 and SF_2 (Fig. 4.1(e)). This wedge structure involves both SF_1 and SF_2 with a 1/6<110>-type stair-rod dislocation at the intersection between the two SFs (inset in Fig. 4.1(e)).

It further evolves under the applied load, resulting in a 2-3 nm sized triangular defect (as indicated by the yellow triangle in the inset of Fig. 4.1(f)). Such triangular defect is identical to the projected view of SFT along the $[1\bar{1}0]$ direction, in both its shape and geometric angles. Moreover, the morphology of this triangular defect appears to be the same as that of the vacancy-originated SFT reported in the literature [89, 95, 120].

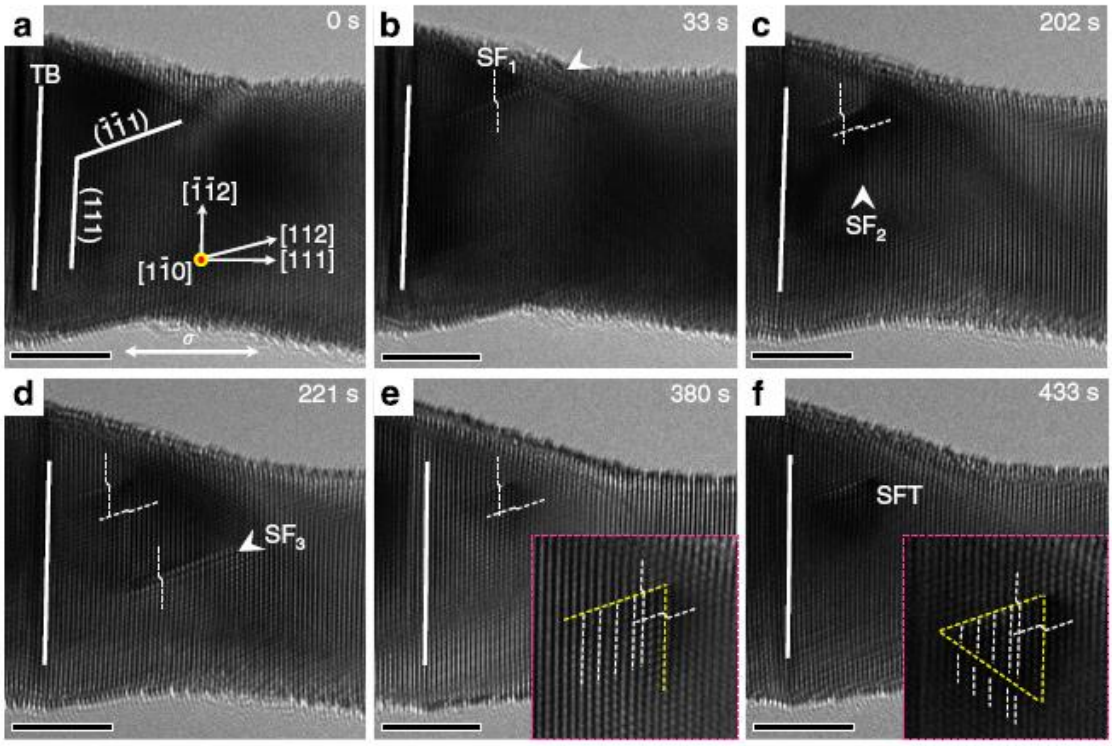

Fig. 4.1 Formation of dislocation-originated stacking fault tetrahedra (SFT). **(a)** Crystallographic orientation of the Au nanowire embedded with a twin boundary (TB). The nanowire diameter is about 16 nm. **(b-f)** Sequential high resolution transmission electron microscopy (HRTEM) images showing the evolution of dislocation structure and the formation of a dislocation-originated SFT via the interactions of partial dislocations under $[111]$ tensile loading. Upon tensile loading, the partial dislocations with stacking faults (SFs) nucleate sequentially from the free surface on the equivalent inclined $\{111\}$ planes and interact with each other, forming a wedge (c) and then a zigzag (d) dislocation structure. (e) At 380 s, SF_3 propagates and annihilates at the free surface, leaving behind the wedge structure. The inset shows the enlarged HRTEM image of the wedge structure (yellow dashed line). (f) The wedge dislocation structure further evolves into a triangular defect, which is identified to be an SFT. The inset marks out the SFT by a yellow triangle. Scale bar, 5 nm.

Figure 4.2 shows the formation of dislocation-originated SFT via dislocation interactions in an Au nanowire, as realized in our MD simulations. The Au nanowire is subjected to tensile loading along the $[111]$ axial direction. Similar to our experimental observation, a leading partial dislocation of 1/6<112>-type and of a Schmid factor of 0.31 (denoted as βA in Fig. 4.2(f) is seen to nucleate from the nanowire surface; and it propagates on the $(\bar{1}\bar{1}1)$ plane, leaving SF_1 behind (Fig. 4.2(a)). Subsequently, two new

partial dislocations, denoted as δA and γA (and with the same Schmid factor of 0.31) are triggered on the $(\bar{1}\bar{1}\bar{1})$ and $(1\bar{1}\bar{1})$ planes, respectively, enclosing SF_2 and SF_3 (Fig. 4.2(b,f)). Note that SF_3 is covered visually by SF_1 and SF_2 and thus cannot be seen in Fig. 4.2(b-c). Partials of δA and γA propagate into the nanowire and lock with βA, forming three 1/6<110>-type sessile stair-rod dislocations, denoted as $\beta\gamma$, $\delta\beta$ and $\gamma\delta$ in Fig. 4.2(f). These sequential dislocation nucleation and interaction events create an initial 'open-SFT' with only three completed faces (Fig. 4.2(b)).

Under further tensile loading, trailing partial dislocations βC, δB and γD, which have a Schmid factor of 0.16, nucleate as in Fig. 4.2(g), the propagation of which eliminates a part of the SFs on each of the three faces of the open-SFT (Fig. 4.2(c,g)), thus removing the trails of the initial open-SFT. A closed-SFT finally forms via the cross-slip of one of the trailing partials into the open (111) plane, producing SF_4 that constitutes the base of the closed-SFT; the three 1/6<110>-type sessile dislocations $\beta\alpha$, $\delta\alpha$ and $\gamma\alpha$ enclose the base of the closed-SFT (Fig. 4.2(d,h) and Fig. 4.3).

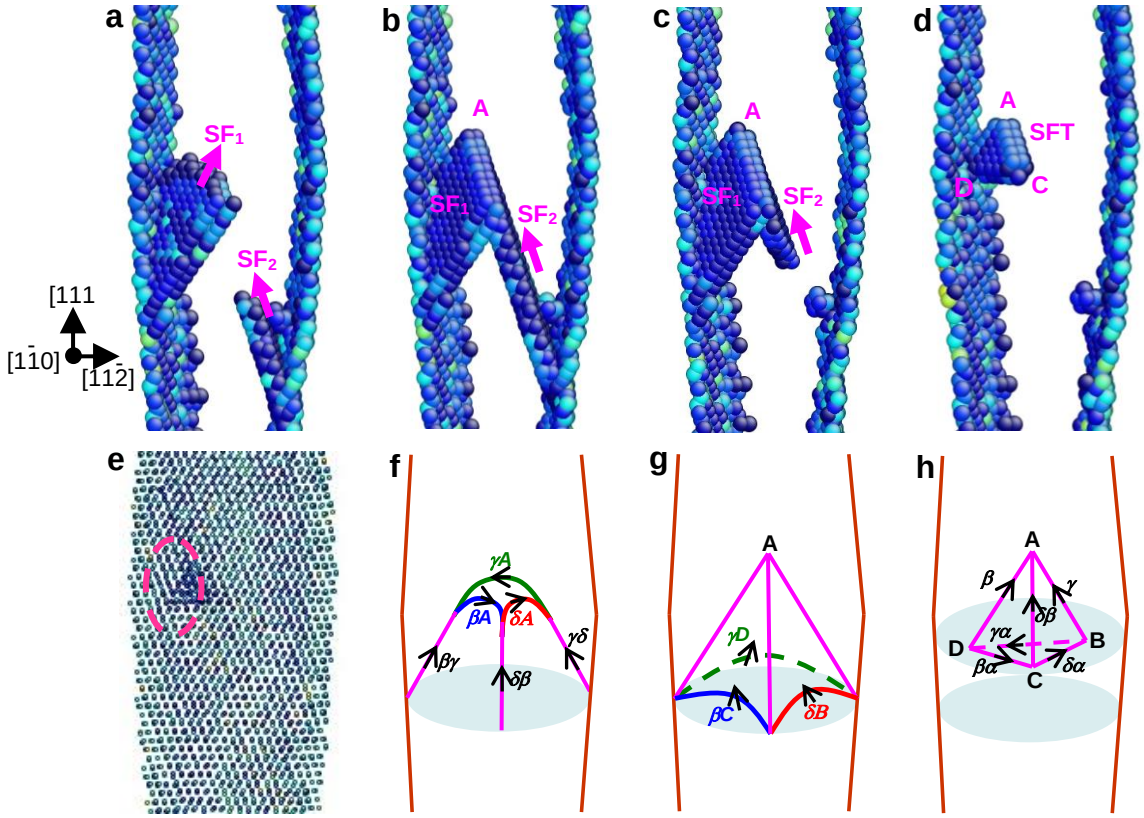

Fig. 4.2 Formation of dislocation-originated SFT in molecular dynamics (MD) simulation. The Au nanowire is loaded in the [111] direction. **(a)** A leading partial with trailing SF_1 nucleates from the free surface on the $(\bar{1}\bar{1}1)$ plane under tensile loading. **(b)** Two new SFs, SF_2 and SF_3, nucleate on the $(\bar{1}1\bar{1})$ and $(1\bar{1}\bar{1})$ plane respectively, and intersect with SF_1, forming the initial open-SFT. Note that SF_3 is covered visually by SF_1 and SF_2 and thus cannot be seen directly. **(c)** The nucleation of trailing partials sweeps out part of the SFs, thus removing the trails of the initial open-SFT. **(d)** The closed SFT finally forms by dislocation cross-slip. **(e)** Projection view of the closed SFT along the <110> direction. **(f-h)** Schematic illustration of the detailed dislocation processes during the SFT formation.

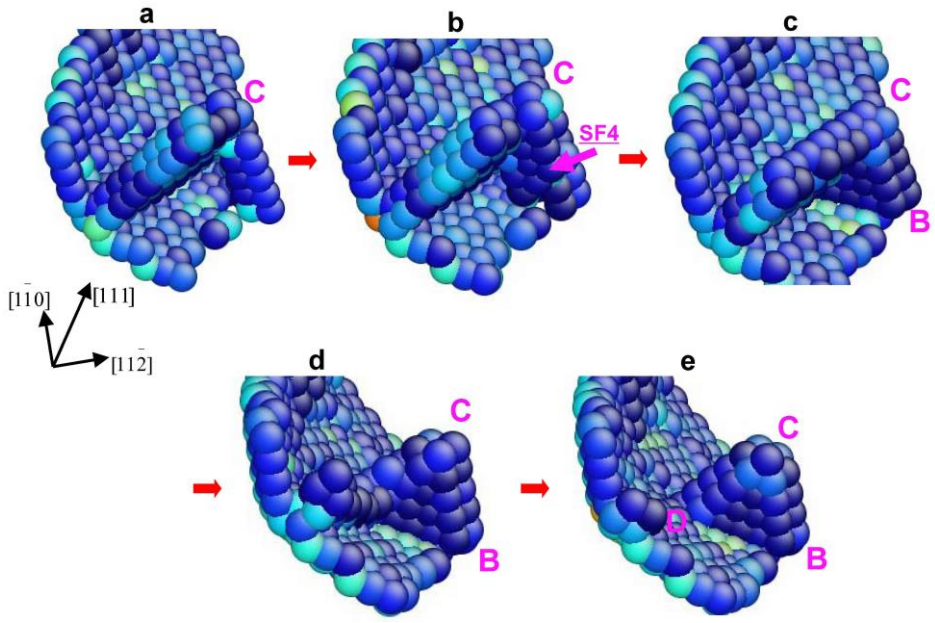

Fig. 4.3 Formation of a closed-SFT through the cross-slip of a trailing partial. (a) The initial open-SFT formed by the interactions of partial dislocations, as in Fig. 2c in the main text. (b) SF_4 propagates into the open (111) plane through the cross-slip of a trailing partial in Fig. 4.2(g) in the main text. (c-d) The propagation of SF_4 removes the trails of the initial open-SFT and produces the fourth face of the SFT. (e) The base BCD of the SFT in Fig. 4.2(d), is fully formed making it a closed-SFT.

The complete set of dislocation reactions leading to the formation of the closed-SFT, can be written as below:

1. Two Shockley partial dislocations of the 1/6<112> type react to form a sessile stair-rod dislocation of the 1/6<110> type (Fig. 4.2(f)), as follows:

$$\frac{1}{6}<\bar{1}2\bar{1}>+\frac{1}{6}<\bar{1}\bar{1}2>\rightarrow\frac{1}{6}<011>$$

$$\beta A+\gamma A\rightarrow\beta\gamma$$

$$\delta A+\beta A\rightarrow\delta\beta$$

$$\gamma A+\delta A\rightarrow\gamma\delta$$

2. One of the trailing partials δB, cross-slips into the basal plane BCD (Fig. 4.2(h)) producing three partials with equivalent burgers vectors (as they are all in the plane

orthogonal to the loading direction and hence have zero Schmid factors)

$$\delta B \xrightarrow{cross-slip\ into\ BCD} B\alpha, C\alpha, D\alpha$$

Each of the three partials in BCD react with the other trailing partials to form the three stair-rod dislocations $\beta\alpha$, $\delta\alpha$, and $\gamma\alpha$, constituting the base BCD of the SFT:

$\gamma D + D\alpha \rightarrow \gamma\alpha$ (along BD)

$\beta C + C\alpha \rightarrow \beta\alpha$ (along DC)

$\delta B + B\alpha \rightarrow \delta\alpha$ (along CB)

Figure 4.2(e) shows the projected image of the SFT in Fig. 4.2(d) as viewed along the <110> direction, which is same as the experimental observation under HRTEM. The simulation result is consistent with our experimental observation in that the SFT are produced directly by a sequence of partial dislocation nucleation and interaction events in nanocrystals, which is hence different from the vacancy-originated mechanism of SFT formation in bulk materials.

The structure of the dislocation-originated SFT is compared with the vacancy-originated SFT. Fig. 4.4(a) presents the schematics of intrinsic and extrinsic SFs by using a line of atoms with the single and double faults of stacking along the close-packed direction of <110>. With such schematics as reference, it is evident that the SFs (e.g., SF_1 and SF_2) in a dislocation-originated SFT are of the intrinsic type (Fig. 4.4(b)), each of which involves only one faulted plane of stacking. In Fig. 4.4(c), a vacancy-originated SFT is "artificially" created in a nanowire by relaxing a triangular vacancy loop (i.e., a Frank loop) [95, 100]. Each of the SFs also involves only one faulted plane of stacking, and thus is of the intrinsic type. The minor differences in colour between the two types of SFT arise owing to the fact that the former is subjected to a large tensile stress, while the

latter is stress free. Comparison between the two types of SFT proves that the dislocation-originated SFT is structurally equivalent to the vacancy-originated SFT. However, the dislocation-originated SFT can play an important role in controlling the plasticity of FCC metallic nanostructures (see the Discussion section).

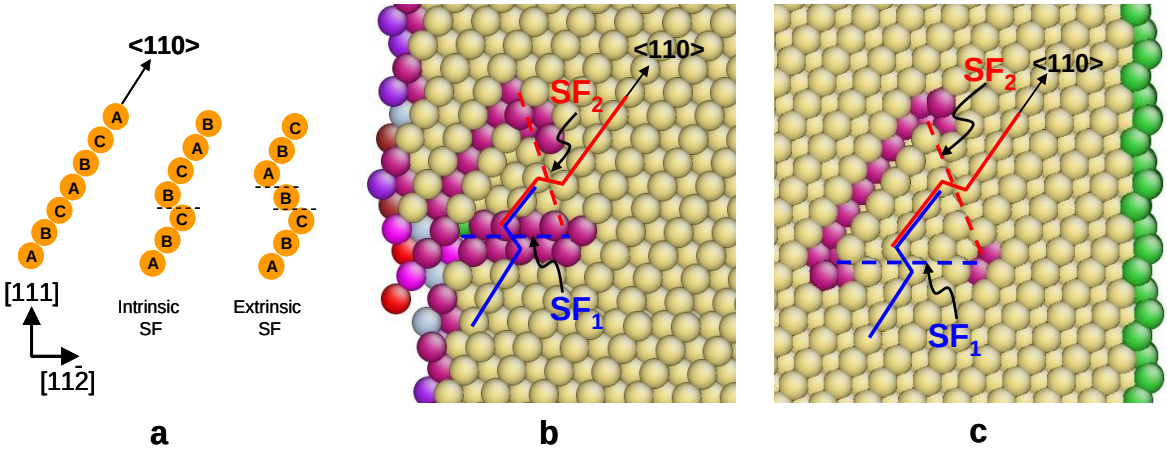

Fig. 4.4 Crystallographic structure of the dislocation-originated and vacancy-originated SFT. **(a)** Schematic representation of the intrinsic and extrinsic stacking faults in terms of the A/B/C atomic layer stacking, as well as the single and double kinking (faults) along the close-packed direction of <110>. **(b)** {110} cross section of a dislocation-originated SFT, with atoms colored by their coordination numbers. **(c)** Same as (b) except for a vacancy-originated SFT formed via the Silcox-Hirsch mechanism.

4.3.2 Migration of Dislocation-originated SFT

Similar to the Lomer-Cottrell lock, the SFT is bounded by SFs and stair-rod dislocations [84], and is usually sessile. In nanocrystals, however, the SFs are frequently nucleated from the surface and could induce migration and annihilation of the dislocation-originated SFT by dislocation-SFT interactions. Figure 4.5 shows the migration of a dislocation-originated SFT during tensile deformation of an Au nanowire. In this case, two dislocation-originated SFT (SFT_1 and SFT_2) are produced sequentially

via partial dislocation interactions (Fig. 4.5(a)). Upon further loading, a group of partial dislocations, which consists of four leading partials on adjacent $(\bar{1}\bar{1}1)$ planes (Fig. 4.5(c)), nucleates from the TB at a nucleation stress of about 2.3 GPa and interacts with SFT_2 (Fig. 4.5(b)). The dislocation group drives the migration of SFT_2 along the $[00\bar{1}]$ direction, which can be seen from the changes in the distance (or the number of atomic layers) between SFT_1 and SFT_2 (Fig. 4.5(b-f)). In the beginning, the measured distance between the two SFT on the (111) and $(\bar{1}\bar{1}1)$ planes is respectively 1.9 nm and 2.1 nm (Fig. 4.5(b)), corresponding to 7 and 8 atomic layers (inset in Fig. 4.5(b)). Subsequently, the interaction between the dislocation group and SFT_2 reduces the distance between the two SFTs (Fig. 4.5(d)). Finally, after the dislocation group is annihilated at the free surface, the distance between the two SFT decreases respectively to 1.2 nm and 1.4 nm on the (111) and $(\bar{1}\bar{1}1)$ planes (Fig. 4.5(e)), corresponding to 4 and 5 atomic layers (inset in Fig. 4.5(e)). The measured changes in the distance between the two SFT match well with the distance between the corresponding atomic layers. Interestingly, the distance between the two SFT increases after a further increase of tensile loading (Fig. 4.5(f). It is worth pointing out that the size and shape of SFT_2 remain unchanged before and after its migration.

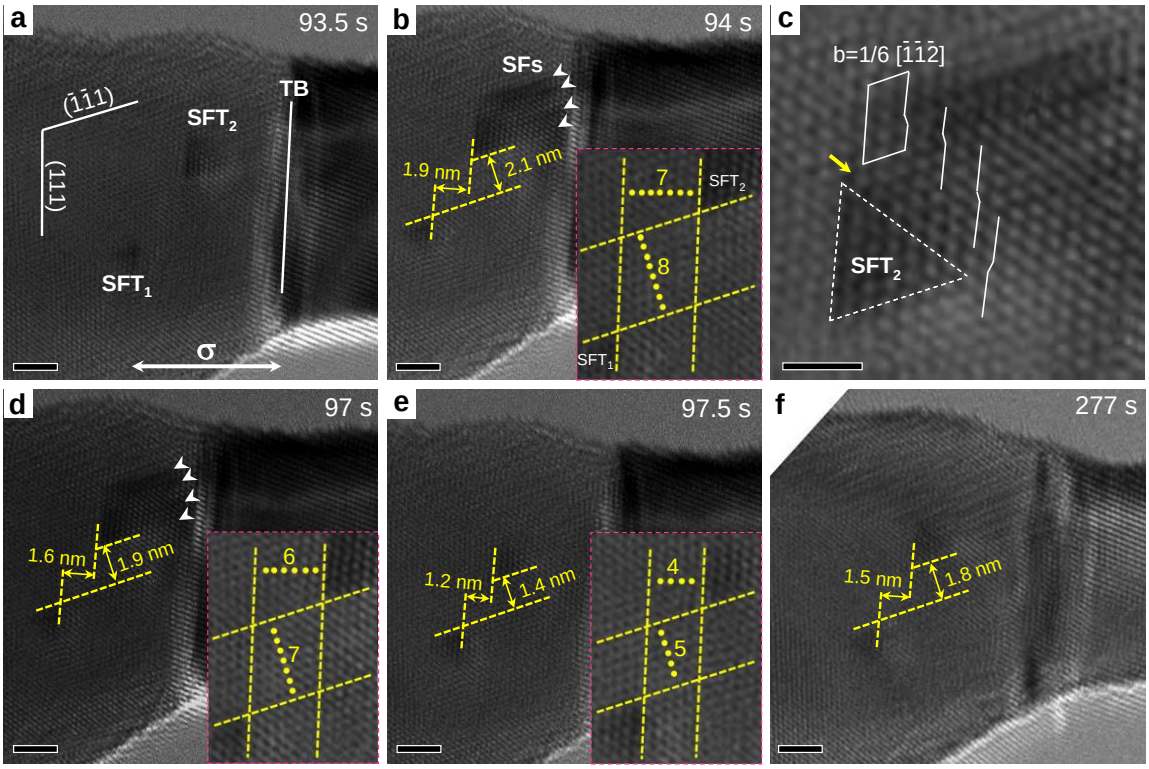

Fig. 4.5 Migration of dislocation-originated SFT during deformation. (a) Under tensile loading, two dislocation-originated SFTs (SFT_1 and SFT_2) are produced sequentially. (b) Upon further deformation, a group of partial dislocations (indicated by the white arrows) nucleate from the TB and interact with SFT_2. (c) Structure of the partial dislocations group, which consists of four parallel leading partials with SFs. The yellow arrow indicates the strain contrast induced by dislocation-SFT_2 interaction. (d-f) The dislocation group drives SFT_2 to migrate, as indicated by the changes of distance and atomic layers between SFT_1 and SFT_2 on the (111) and $(\bar{1}\bar{1}\bar{1})$ plane, respectively. Insets in (b) and (d-e) are the changes of atomic layers between SFT_1 and SFT_2 on the (111) and $(\bar{1}\bar{1}\bar{1})$ plane, respectively. Scale bar in (a-b, d-f), 2 nm; Scale bar in (c), 1 nm.

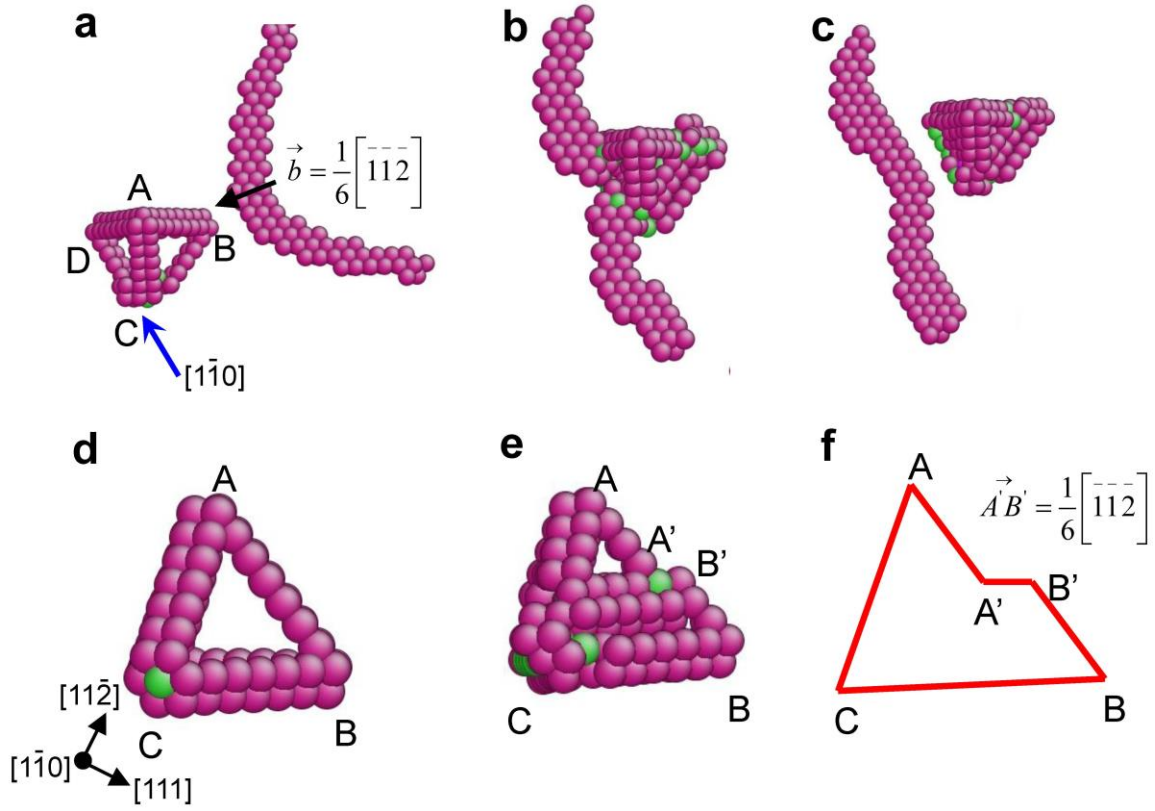

Fig. 4.6 Interaction of a partial dislocation with SFT and the surface step on SFT created by the interaction. (a-c) The dislocation-SFT interaction process. The dislocation is a partial dislocation with burgers vector of $\frac{1}{6}[\bar{1}\bar{1}2]$. (d-e) The ABC face of the SFT, before and after the dislocation-SFT interaction, clearly depicting the surface step in the direction of its burgers vector. (f) Schematic of (e).

The migration of dislocation-originated SFT can, in principle, result from thermal or mechanical activation. Migration of dislocation loop and vacancy cluster has been observed in irradiated or quenched metals [120-122], the reason for which is attributed to thermal activation [122]. In the present experiment, thermal activation is unlikely, since the migration is only observed when a group of dislocations interact with the SFT. Therefore, we attribute the migration of SFT to the activation by mechanical stress that leads to dislocation-SFT interactions. It is known that due to applied loads, the vacancy-originated SFT can be sheared or distorted by interactions with dislocations [100-103],

which could result in the movement of the apex atoms of SFT to new positions [100] and thus produce ledges on SFT [103]. The migration of these ledges by the absorption of vacancies or atoms can cause the growth or shrinkage of the vacancy-originated SFT [107, 123]. Similarly, the gliding dislocation upon interaction with the dislocation-originated SFT can produce ledges on the side of SFT for a single dislocation-SFT interaction event (Fig. 4.6). As a result, the SFT can effectively migrate via simultaneous interaction events with multiple dislocations. Moreover, the relatively large surface-to-volume ratio in nanocrystals, as opposed to their bulk counterparts, could promote the SFT migration by feeding more SFs from the fertile surface nucleation sites. Additionally, it should be noted that the movement of SFT is distinct from the climb or glide process of dislocation under mechanical loading. The dislocations can climb or glide by themselves under external loading, whereas the SFT cannot move by itself and its migration must be driven by the dislocations through dislocation-SFT interactions.

4.3.3 Annihilation of Dislocation-originated SFT

The annihilation of dislocation-originated SFT is also observed by our *in-situ* experiment (Fig. 4.7). The pristine Au nanocrystal in Fig. 4.7 is created by cold welding between two Au nanostructures [124].

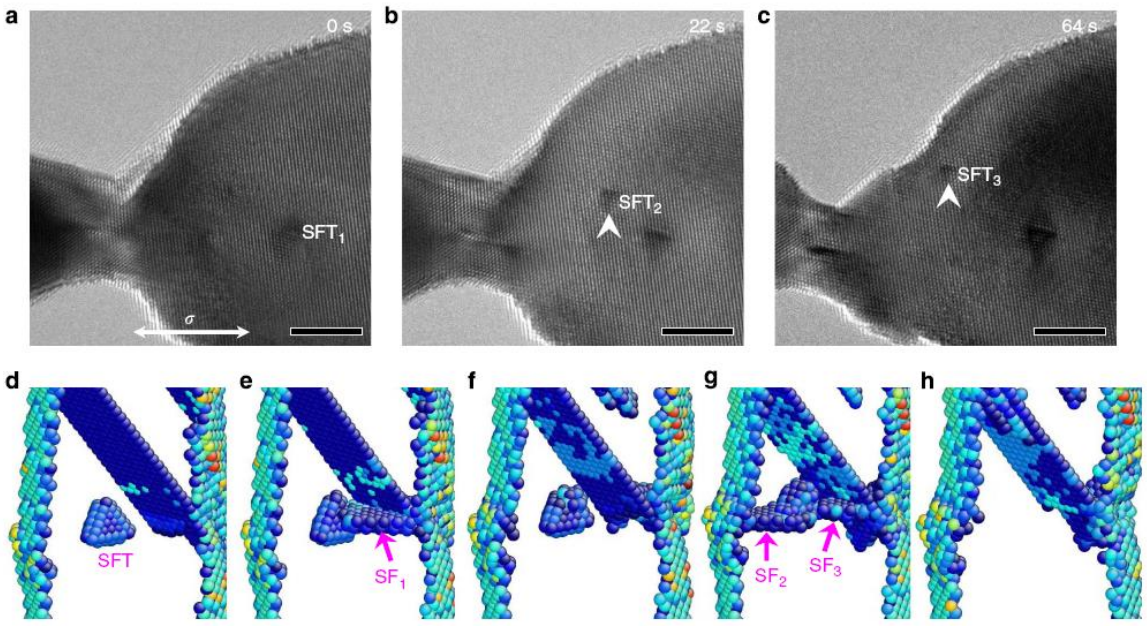

Fig. 4.7 Annihilation of dislocation-originated SFT under tensile deformation. (a-c) Sequential HRTEM images showing the annihilation of a dislocation-originated SFT induced by deformation. (a) SFT_1 is observed in the pristine nanocrystal after cold welding. (b) Upon tensile loading, SFT_2 is produced near SFT_1. (c) Further deformation leads to annihilation of SFT_2 and nucleation of SFT_3. Scale bar in (a-c), 5 nm. **(d-h)** MD snapshots showing the annihilation of a dislocation-originated SFT by dislocation-SFT interactions. (d) A closed SFT formed near a TB in the Au nanowire. (e-f) A partial dislocation with SF_1 makes an edge-on interaction with the SFT, and shears and distorts the closed SFT. (g-h) Partial dislocations with SF_2 and SF_3 nucleate subsequently, lead to the complete annihilation of the SFT.

Interestingly, SFT_1 is observed in the pristine Au nanocrystal right after cold welding (Fig. 4.7(a)), which indicates the occurrence of plastic deformation during the cold welding process. Generally, when two nanostructures come into contact, a large mechanical stress could be induced at the contact zone, owing to the mismatch of geometry and orientation, which can result in the so-called dislocation-mediated pseudoelastic deformation if the contact surface is atomically flat [125]. In our experiment, however, the surfaces of the two nanostructures are not atomically flat (Fig. 4.7(a)), resulting in the residual dislocations or SFT after contact. Moreover, due to the

relatively low strain rate of cold welding and the large image stress associated with a small sample size, supersaturation of vacancies is unlikely in the cold-welding process and hence SFT_1 should be of the dislocation-originated type.

Upon mechanical loading, a new SFT (SFT_2) is produced near SFT_1 (Fig. 4.7(b)). However, further deformation leads to the annihilation of SFT_2 and nucleation of SFT_3 (Fig. 4.7(c)). Since the SFT_2 disappears fast (in less than 0.5s), the details of annihilation are not captured during *in-situ* experiment. However, the SF trace left indicates that the annihilation of SFT is mediated by dislocation-SFT. MD simulations (Fig. 4.7(d-h)) further prove that the annihilation of dislocation-originated SFT is indeed a dislocation-mediated process, which is similar to that found for the vacancy-originated SFT in the bulk [96-102]. Figure 4.7(d) shows a closed dislocation-originated SFT near a TB inside the nanowire. Under tensile loading, a partial dislocation loop enclosing SF_1 nucleates on (111) plane and makes an edge-on interaction with the SFT at the third atomic layer of the SFT from its apex. The closed-SFT is sheared and distorted (Fig. 4.7(e-f)). This event is followed by similar events of newly nucleated partial dislocations shearing the closed-SFT (Fig. 4.7(g-h)). The Shockley partial dislocation with the trailing SF_2 nucleates and interacts with the 1/6<110>-type sessile stair-rod dislocations constituting the basal plane of the SFT. These processes lead to the formation of new 1/6<112>-type Shockley partials which would be expected to glide on the tetrahedral planes of the SFT and partially remove the SFs, as has been reported for the SFT using MD simulations [100]. But what we observe for the SFT in the nano-sized sample is its complete destruction (Fig. 4.7(h)) due to the SFs intersecting at its base and/or above (SF_2 and SF_3 in Fig. 4.7(g)), instead of only a partial destruction as in the bulk samples [98, 102]. Moreover,

since the free surface in the sub-20 nm nanocrystal serves as an efficient nucleation source of dislocations, it could thus play an important role in the annihilation of SFT by providing nucleated dislocations.

4.4 Discussion

SFT have usually been classified as a vacancy-originated volume defect in quenched or irradiated metals and alloys [84, 86-89]. However, it is unlikely that the SFT observed in the Au nanocrystals of this work are vacancy-originated. Firstly, a high density of vacancies is required to nucleate the vacancy-originated SFT, which is often present in quenched or irradiated metals[84, 86-88] but is hardly achievable in our nano-sized metallic samples. Secondly, there are two possible factors regarding the electron beam effect, i.e., knock-on displacement and beam heating. For the knock-on displacement to occur, the threshold electron energy for Au is 1320 KeV [126]. The 300 KV acceleration voltage used in our experiments is therefore insufficient to produce such kind of beam damage [111]. For the beam heating issue, the thermal conductivity of Au is high (300 W mK^{-1}) and the two ends of Au nanowires are respectively connected to an Au substrate and an Au probe with large sizes compared with the samples. Considering the low beam current applied in our experiments (80~100 A cm^{-2}) and the fact that both the Au substrate and the probe act as the effective heat sinks, the temperature rise induced by beam heating should be negligible in the sample [111, 127]. More importantly, SFT are also observed to form during deformation without any beam irradiation and beam induced temperature rise, which further supports the conclusion that the SFT observed during plastic deformation is dislocation-originated and not vacancy-originated. Therefore, the beam irradiation and heating would have little influence on the SFT

formation and dislocation-SFT interactions. Additionally, although vacancy clusters and vacancy-originated SFT can be generated by plastic deformation, high strain rates are required [93, 94]. In our experiments, the strain rate employed is relatively low and thus cannot produce sufficient vacancies by plastic deformation alone. Even if a smaller number of deformation induced vacancies may exist, they could easily escape the nanocrystal from its free surface, owing to the large image stress associated with the small crystal size and the low strain rate employed, rather than condense into vacancy clusters inside the Au nanocrystal. Therefore, the observed SFT likely result from the interactions of partial dislocations, and our large scale MD simulations lend a direct support to this mechanism. On the basis of these considerations, we believe that the formation, migration and annihilation of the dislocation-originated SFT are revealed for the first time in sub-20 nm nanocrystals.

It is generally recognized that the surface-nucleated dislocations initiate the plastic deformation in nano-sized crystals [110-112]. The partial dislocations nucleated on the equivalent, inclined $\{111\}$ planes can strongly interact with each other inside the small volume of Au nanocrystals, resulting in the stair-rod dislocations and nano-sized dislocation-originated SFT. We have frequently observed the dislocation-originated SFT during the deformation of Au nanocrystals with different sample sizes and loading conditions in both experiments and MD simulations (Fig. 4.8). Hence, the formation and evolution of SFT should be considered as an important deformation mechanism at this length scale.

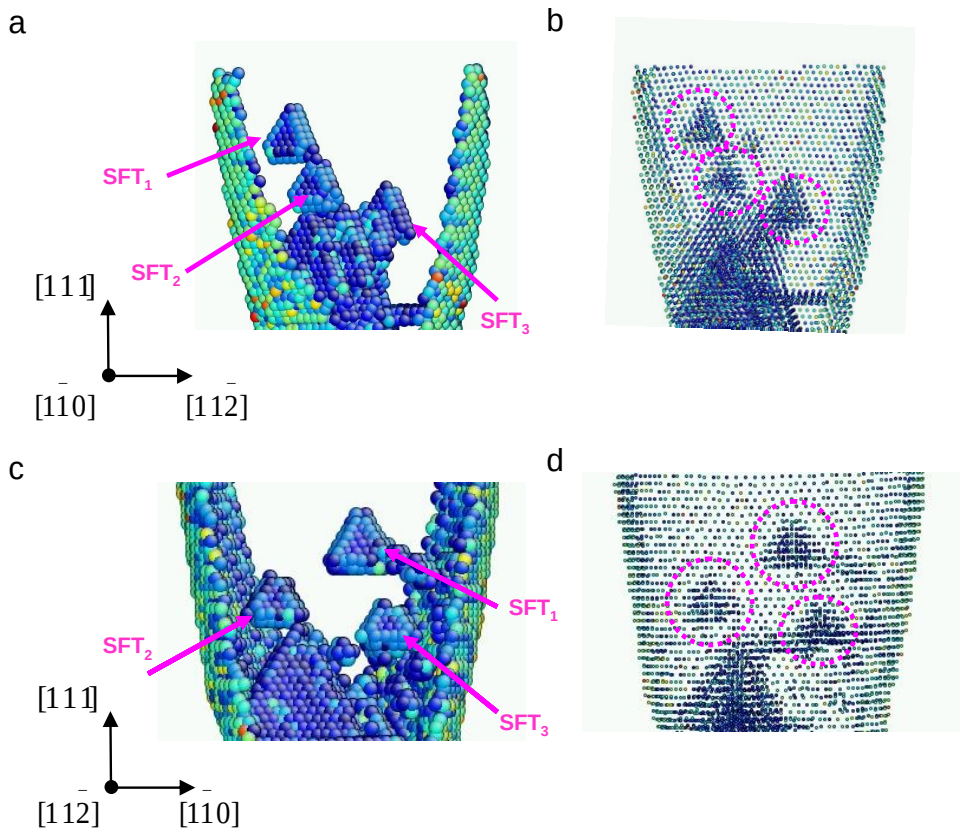

Fig. 4.8 Formation of multiple SFT in a larger Au nanowire. The Au nanowire is a double conical in shape and of 10 nm and 6 nm in diameters, respectively. In order to demonstrate that SFT are fully developed but not inter-connected, (a-b) show the atomic configurations viewed from the <110> direction, and (c-d) from the <112> direction.

Moreover, both SFT formation and dislocation-SFT interaction can contribute to the strain hardening of small-volume samples (Fig. 4.9). Nanocrystals are known to have limited strain hardening due to the lack of sufficient hardening obstacles (dislocations or other defects) as well as the easy annihilation of dislocations at the surface owing to the large image stress [111, 112, 128]. In contrast, the formation of dislocation-originated SFT is a novel mechanism by which the nanocrystal could achieve finite amounts of inherent hardening. In addition, SFT act as strong obstacles to the motion of other dislocations (as shown in Fig. 3) and contribute to further hardening.

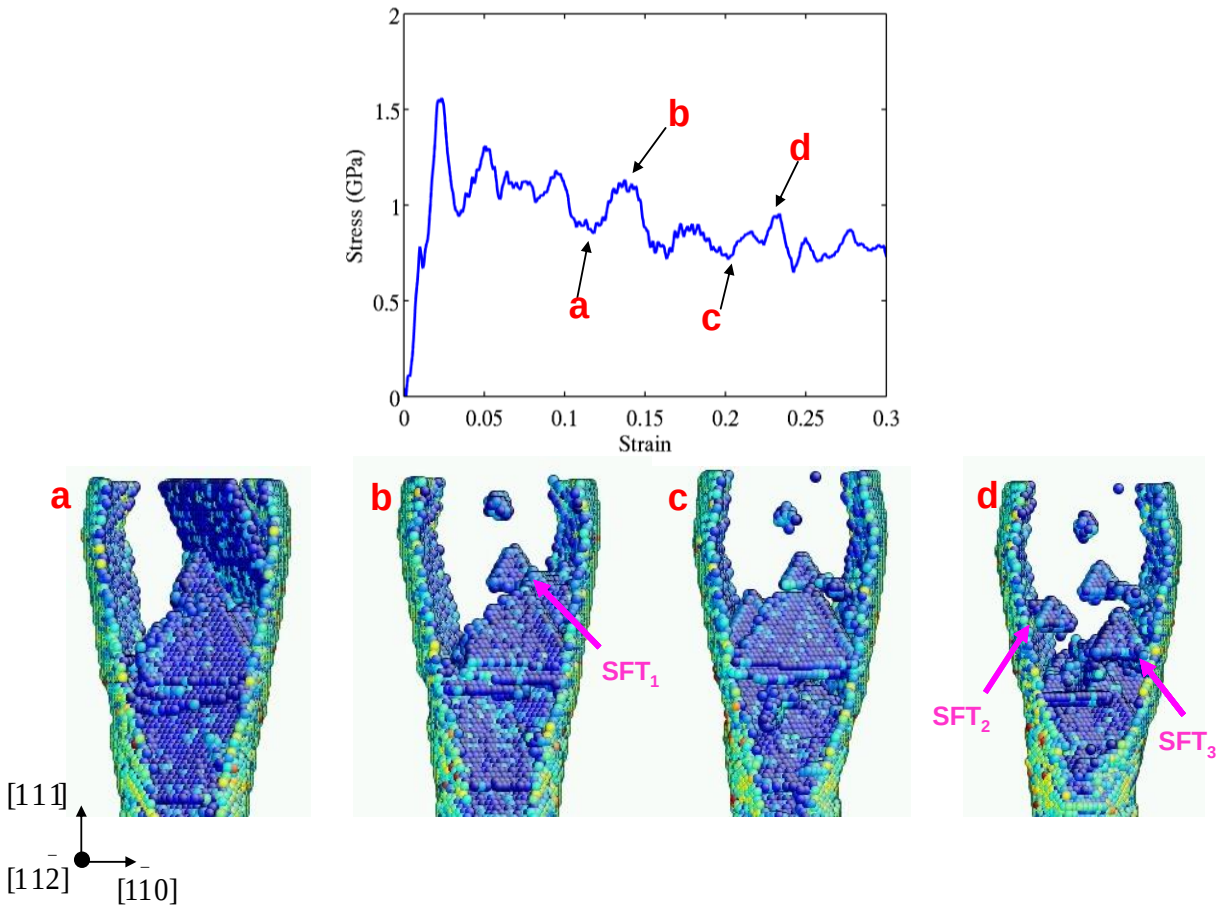

Fig. 4.9 Stress-strain curve for an Au nanowire under uniaxial tension and the MD snapshots at various strain levels. The Au nanowire is double conical in shape, 28.26 nm long, and the diameters being 10 nm and 6 nm, respectively.

In Fig. 4.9, one should ignore the first high peak, which is well-known to be caused by the high elastic stress required for nucleation of surface dislocations in a pristine nanowire. In other words, one should look into the stress-strain response beyond the first yield peak in order to understand the hardening response in MD. The several major ups and downs in the post-yield stress-strain behavior are due to hardening by dislocation interactions and SFT formation, and softening due to surface nucleation events. For example, the snapshot (a) is the beginning stage of the formation of SFT through dislocation interactions and at snapshot (b) the SFT_1 is fully formed. The corresponding points are marked in the stress-strain curve and it can be seen that the formation of SFT

involves a rise in the stress level, indicating hardening. The same sequences of events are repeated between snapshot (c) and snapshot (d) during the formation of SFT_2 and SFT_3 (as seen in snapshot d). The resultant hardening can also be seen in the stress-strain curve.

Furthermore, our results indicate that the SFT formation is not limited to the specific set of dimensions of the simulated nanowire, and the size of SFT formed depends on the sample size. Dislocation-originated SFT are also formed in a deformed Cu nanowire following the same dislocation-mediated mechanism as in the Au nanowires as shown in Fig. 4.10 below. It is observed that SFT were formed in the Cu nanowire, following the sequence of dislocation interactions, as in Au nanowires. The initial open-SFT is formed by the locking of the partial dislocations as can be seen in Fig. 4.10(a). As in Fig. 4.2(b-c) only two of the three SFs constituting the open-SFT are seen in this viewing angle. Trailing partials nucleate and sweep out a part of SF_1 and SF_2 in Fig. 4.?(b) and (c), respectively. Subsequent cross-slip of the trailing partial occurs to form the fourth (basal) face and the complete SFT is formed as shown in (d). This result indicates that the dislocation-originated formation of SFT is a general deformation mechanism applicable to a broad class of FCC metals and alloys with medium to low stacking fault energies under mechanical loading. On the basis of the above discussions, it can be concluded that SFT formation is a general plastic deformation mechanism in metallic nanocrystals, and has important consequences with respect to plastic deformation at small length scales.

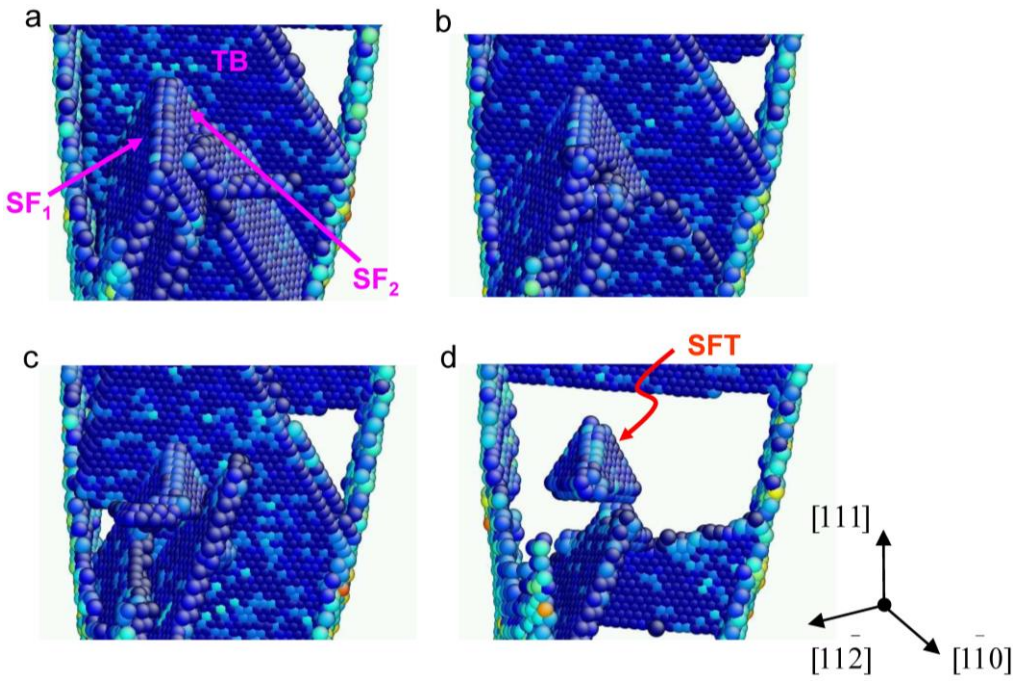

Fig. 4.10 Formation of SFT in MD simulation of a deformed Cu nanowire through the same mechanism explained in Fig. 4.2 and Fig. 4.3. The simulation methodology and the shape and the dimensions of Cu nanowires are similar to those for Au nanowires.

The deformation induced formation of 3D defects has never been reported for nanocrystals. In the conventional bulk samples, SFT form mostly due to irradiation or quenching alone [86, 87], while in the nanocrystals SFT can form directly from dislocation interactions. Moreover, the dislocation-SFT interaction is known to cause the SFT to be sheared into two defects, converted to other types of defects or structurally destroyed [96, 101-104]. However, our work also reveals that the SFT can interact with a group of dislocations nucleated from the surface, resulting in the migration of SFT in a small and confined volume without any change in its shape and size. Such migration (i.e., displacive movement) of SFT can be attributed to the active operation of surface dislocation sources that is promoted by the high stress, large image force and abundant

surface nucleation sites associated with the small crystal size, while it would be rare to achieve these conditions necessary for the SFT migration in the bulk. These unusual phenomena represent the novel deformation mechanisms at the nanoscale, and their potential effects on the strength, hardening and fracture warrant further study in the future.

4.5 Conclusions

In summary, *in-situ* HRTEM experiments are conducted to directly visualize the atomic-scale, dynamic evolution of a novel defect structure − dislocation-originated SFT − in Au nanocrystals. Our work for the first time discovers the formation and the dynamics of a 3D crystalline defect in small-volume nanocrystals, which plays an important role in the plasticity at small length scales. These results reveal a novel deformation mechanism of dislocation interaction inside the confined volume of nanocrystals. Our work has significant implications on understanding the deformation behaviours of nanocrystals, including plastic yielding, strain hardening, ductility, size effects, *etc.*, which will motivate further experimental and modelling investigations of dislocation interactions and formation of higher order defects in small-sized materials. On the other hand, our discovery also provides an example of the deformation induced and dislocation-originated formation mechanism of SFT in contrast to the conventional wisdom of vacancy-originated SFT, which thus expands the fundamental knowledge of 3D volume defects in small-sized, non-irradiated materials. A more detailed understanding of various factors affecting the formation of SFT warrants further study in the future.

CHAPTER 5

INTERFACE MEDIATED PLASTICITY AND IMPLICATIONS FOR IRRADIATION DAMAGE

5.1 Introduction

Materials with nanoscale or microscale engineered interfaces have received lot of attention as irradiation resistant materials. Specific material interfaces can be engineered and tailor-made to make interfaces that can act as inexhaustible sinks for irradiation induced defects like vacancies and interstitial atoms [129, 130]. In this chapter we investigate the mechanical behavior of silver nanowires that possess a unique five-fold twinned internal interfacial structure. Our goal is to better understand how the interfaces contribute to their basic mechanical behavior, specifically work hardening, so that they could be employed in irradiated atmospheres so as to resist the irradiation induced material damage.

Nanoscale structures like nanowires are known to exhibit ultra-high yield strength, but limited hardening, and low ductility (tensile strain to fracture) [108, 109, 131-133]. Insufficient hardening can severely affect the mechanical integrity of the constituent nanostructures in nanomechancial devices and other technological applications. This lack of hardening has been understood to be due to the absence of effective obstacles within the nanowire, that otherwise could block the movement of crystalline defects like dislocations so as to produce macroscopic hardening [132]. Hence engineering the

internal interfaces and defects of the nanoscale materials towards improving hardening has been a significant area of research in recent years [109, 133].

Many recent studies have focused on the study of single-crystalline metallic nanowires through experiment and modeling. Single crystalline nanowires of face-centered cubic (FCC) metals like silver, nickel, copper and gold (Fig. 5.1(a)) have been found to deform via dislocation-mediated plasticity [48, 134-137] or via deformation twinning and lattice reorientation [138-141], without exhibiting pronounced hardening. To promote strain hardening, nanowires with coherent internal twin boundaries (TBs) have recently received much attention owing to the capability of the TBs to contribute to hardening by acting as barriers to dislocation motion. For example, nanowires with horizontal TBs (Fig. 5.1(b)) have been studied [29, 142-146]. But effective hardening due to these horizontal TBs requires uniformly small twin spacing across the entire length of nanowires, thus imposing a challenge to the controlled nanowire synthesis. In addition, the inclined TBs in nanowires (Fig. 5.1(c)) are prone to migrate, causing the coarsening of nanotwins through detwinning [146].

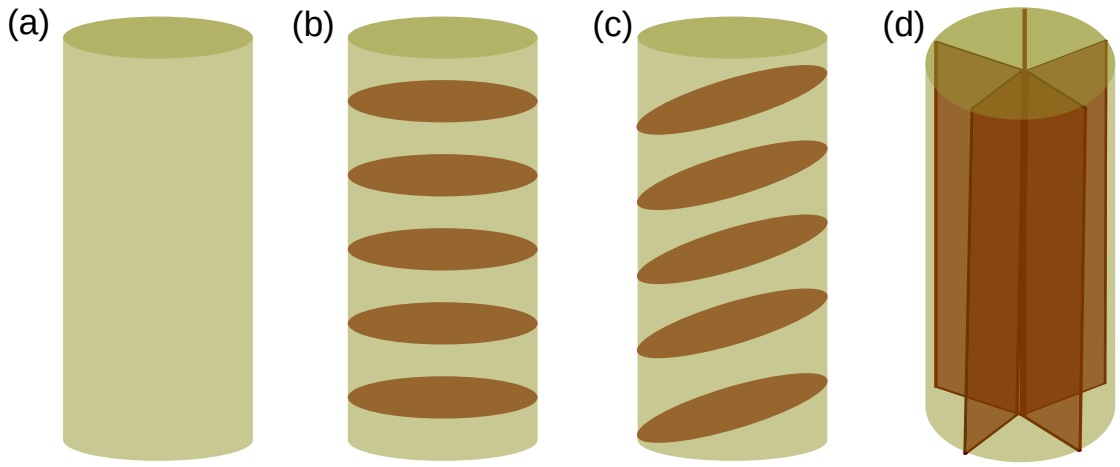

Fig. 5.1 Schematic showing twin-boundary engineered metallic nanowires. (a) Single crystal nanowire. (b) Nanowire with horizontal TBs. (c) Nanowire with inclined TBs. (d) Nanowire with five-fold vertical TB.

In contrast, nanowires with vertical twin boundaries (Fig. 5.1(d)) have shown promising results specifically with respect to strain hardening. Zhu *et al.* [147] reported pronounced strain hardening in Ag nanowires (AgNWs) with a well-defined five-fold vertical twin structure. Filleter *et al.* [148] further studied such kind of AgNWs of various diameters and found that the smaller diameter AgNWs exhibited stronger strain hardening than the larger ones. Despite these promising results, the mechanisms underlying the strain hardening and associated size effects in nanowires with vertical TBs remain unclear.

Recently, several groups have conducted molecular dynamics (MD) simulations to explore the mechanical properties and deformation behavior of the five-fold twinned AgNWs [148-152]. However, these MD works were unable to capture the hardening behavior in the stress-strain responses, which has been observed in experiments. Hence questions as to why MD simulations cannot directly supplement the experimental results or explain the mechanisms governing hardening behavior, remain unanswered.

In this chapter we report a combined experimental and modeling study that combines *in situ* tensile testing within a scanning electron microscope (SEM) and large scale MD

simulations of the five-fold twinned AgNWs. We were able to capture the strain hardening behavior of these nanowires in both experiments and modeling. The detailed hardening mechanisms were further revealed by atomistic analyses of MD results. The hardening behavior was shown to be critically dependent on the nanowire diameter, as well as the pre-existing defects. The simulated necking and fracture modes are compared with experiments. These results provide insights into enhancing the tensile ductility of metallic nanostructures by engineering the internal interfaces and defects.

5.2 Methods

5.2.1 Experiment

Tensile tests were performed using an *in situ* SEM nanomechanical testing setup [153]. An individual NW was clamped on a nanomanipulator tip and an atomic force microscopy (AFM) cantilever using electron beam induced deposition of carbonaceous materials in the SEM. The force was applied using the nanomanipulator (Klocke Nanotechnik, Germany) on one side of the freestanding NW, and was measured on the other side using the AFM cantilever. A series of SEM images were taken during the tension tests; the NW strain was measured by digital image correlation of the SEM images. Pentagonal cross-section was used in calculating the stress.

5.2.2 Modeling

Three dimensional MD simulations were carried out using the parallel simulator, LAMMPS [52]. We employed a recent Embedded Atom Method (EAM) potential by Mishin *et al.* [154] to account for the many-body interactions between Ag atoms.

Stacking faults, twin boundaries and surface atoms are visualized by coloring the atoms based on their centro-symmetry parameters [51]. Tensile tests were conducted on the model AgNWs at 10 K and a strain rate ranging from 10^7 s^{-1} to 10^9 s^{-1}. Periodic boundary conditions were engaged along the $[1\bar{1}0]$ axial direction and the lateral free surfaces were fully relaxed.

5.3 Results and Discussion

Five-fold twinned AgNWs were synthesized by a modified polyol process [155, 156]. Fig. 5.2(a&b) respectively show the transmission electron microscopy (TEM) cross-sectional and perspective images of the five-fold AgNW. Tensile tests were conducted for the AgNWs with diameters ranging from 38 to 130 nm, within an SEM. The measured stress-strain curves are plotted in Fig. 5.2(c). Interestingly, AgNWs of smaller diameters can harden more than the bigger ones. The smallest wire of 38 nm diameter hardens and achieves an ultimate tensile strength of 4.8 GPa, while the largest wire of 130 nm diameter shows limited hardening. These results are in close agreement to the experimental results by Filleter *et al*. [148].

The unique hardening behavior and its size dependence in five-fold twinned AgNWs are conceivably related to the presence of twin boundaries, as they are not typically observed in single-crystalline nanowires and also are not apparent from our experimental results alone. Hence we performed MD simulations to investigate the atomistic mechanisms controlling the size-dependent strain hardening behavior in the five-fold twinned AgNWs.

Fig. 5.3 shows the atomic model used in our MD simulations. In Fig. 5.3(a), we present the cross-sectional view of a $\langle 1\bar{1}0 \rangle$-oriented AgNW with the characteristic five-

fold twinned structure. The angle between two adjacent TBs is equal to 70.5°. Hence the total angle contributed by all the TBs is less than the geometrical total of a regular pentagon by 7.5°. This angular mismatch induces an elastic strain in the AgNW core. Fig. 5.3(b) displays a 3D view of the atomic structure of the five-fold twinned AgNW, with $\{111\}$ TBs and $\{100\}$ free surfaces.

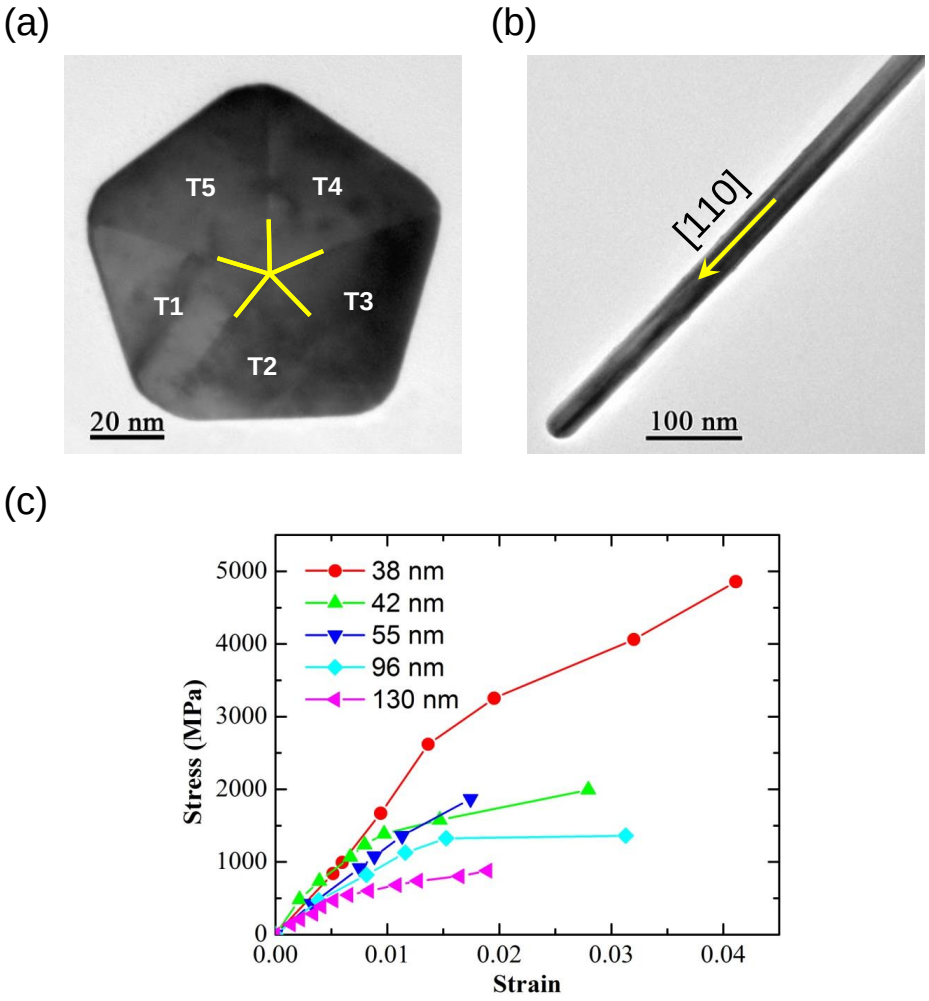

Fig. 5.2 Images and results from experiments. (a) SEM image of the Ag NW cross section. (b) SEM image of the nanowire showing the vertical twin boundary. (c) Stress-strain curve for Ag NWs of various diameters.

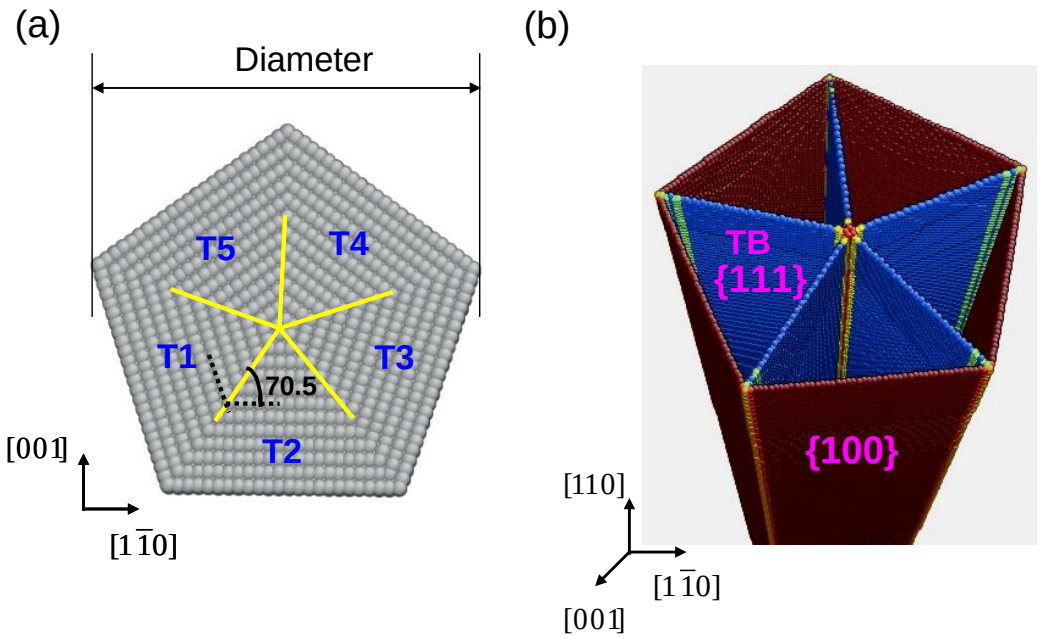

Fig. 5.3 Atomistic model of the five-fold twinned Ag NW. (a) Cross sectional image. (b) Perspective view depicting the twin boundaries and free surfaces.

5.3.1 Dislocation nucleation and interaction with TBs

Fig. 5.4(a) shows the tensile stress-strain curve of a five-fold twinned AgNW with diameter of 6.4 nm. At a strain of about 0.1, the AgNW yields by the nucleation of dislocations from the surface, resulting in an abrupt load drop.

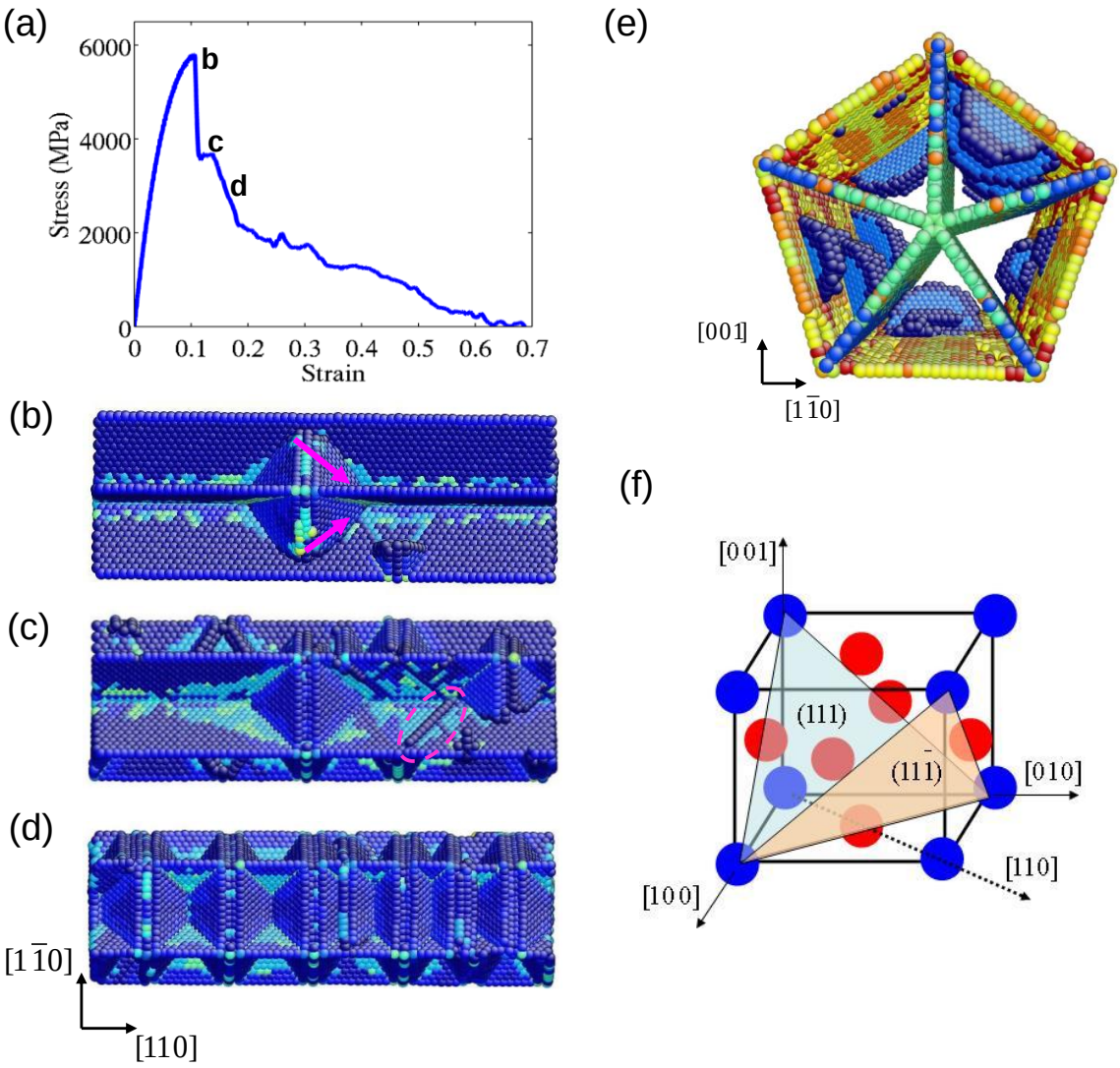

Fig. 5.4 MD simulation results for the pristine Ag NW. (a) Stress-strain curve. (b-d) Atomistic configurations of the points b, c and d as marked in the stress-strain curve. (e) Cross-sectional view of the nanowire showing the dislocation nucleation in two equivalent $[110]\{111\}$ slip systems. (f) Schematic of the FCC unit cell showing the activation of the two equivalent $[110]\{111\}$ slip systems, for tensile loading along $[110]$ direction.

The atomic configuration of the AgNW immediately after the load peak is shown in Fig. 5.4(b). Each dislocation nucleation site on the surface usually breeds two Shockley partial dislocations of the $\frac{a}{6}\langle 112\rangle$ type (where a denotes the lattice constant). Such symmetric

nucleation arises because, for the $\langle 110 \rangle$ loading there are two equivalent $\langle 110 \rangle \{ 111 \}$ slip systems that are activated simultaneously, as shown schematically in Fig. 5.4(f). The Shockley partials glide towards the core of the AgNW as marked in Fig. 5.4(b) and as shown in Fig. 5.4(e); they are subsequently blocked by the TBs. This is understandably the unit dislocation process that contributes to the macroscopic hardening of the AgNW. As the applied load increases, the obstructed Shockley partial can further cross-slip across the TB into the adjacent twin variant, leaving a sessile dislocation at the TB as circled in Fig. 5.4(c). These nucleation-transmission events of partial dislocations are repeated so as to produce a chain of 3D stacking defects, each of which extends across five twin variants centered around the nanowire axis, as shown in Fig. 5.4(d). Filleter *et al.* [148] named each such defect, a stacking-fault-decahedron, owing to the 10 faces that it possesses.

The above MD results reveal the mechanism of TB-mediated hardening in the five-fold twinned AgNW. However, the corresponding stress-strain curve in Fig. 5.4(a) does not capture the strain hardening response as observed in our experiments (Fig. 5.2(c)). Such discrepancy reflects a common shortcoming of the MD stress-strain curve when the model nanowire used is pristine and free of defects. The absence of the pre-existing defects results in a high yield stress due to elastic overshooting, which is followed by a sharp load drop (Fig. 5.4(a)) due to spatially uniform nucleation of many dislocations nearly at the same time. Moreover, the high stress at yield tends to drive the dislocations to bypass the TB without contributing to hardening. Hence the MD results in Fig. 5.4, and in the past works [148-150] as well, are representative of the whisker-like behavior [131], instead of the hardening of five-fold twinned AgNWs as measured in experiments.

5.3.2 Strain hardening and size effect

In order to study the hardening behavior by MD, we introduced pre-existing defects in the simulated five-fold twinned AgNWs. This was achieved by first loading the AgNW and then unloading it after yielding. During unloading, the majority of dislocations in the five twin variants are annihilated at the free surface, creating surface steps and ledges, while a few of them are retained within the nanowire bulk due to the blocking by the TBs. The strain at unloading was kept the same for AgNWs of various diameters, in order to produce comparable densities of defects. These surface defects have lower nucleation stresses than the pristine part of the nanowire. In other words, surface defects break the axial symmetry of the 'pristine' five-fold twinned AgNW by introducing a statistical distribution to the source strengths of surface dislocations. Such symmetry breaking in the 'defective' AgNW promotes sequential, spatially non-uniform dislocation nucleation under loading, as opposed to collective, uniform nucleation in the 'pristine' AgNW. For a given diameter, the defect density could be controlled by unloading at various strain levels during the post-yield deformation.

Fig. 5.5(a) shows the tensile stress-strain curves for the 'defective' AgNWs of diameters 10.8 nm and 15 nm, respectively. Interestingly both AgNWs exhibit the hardening behaviors, consistent with the experimental observations (Fig. 5.2(c)).

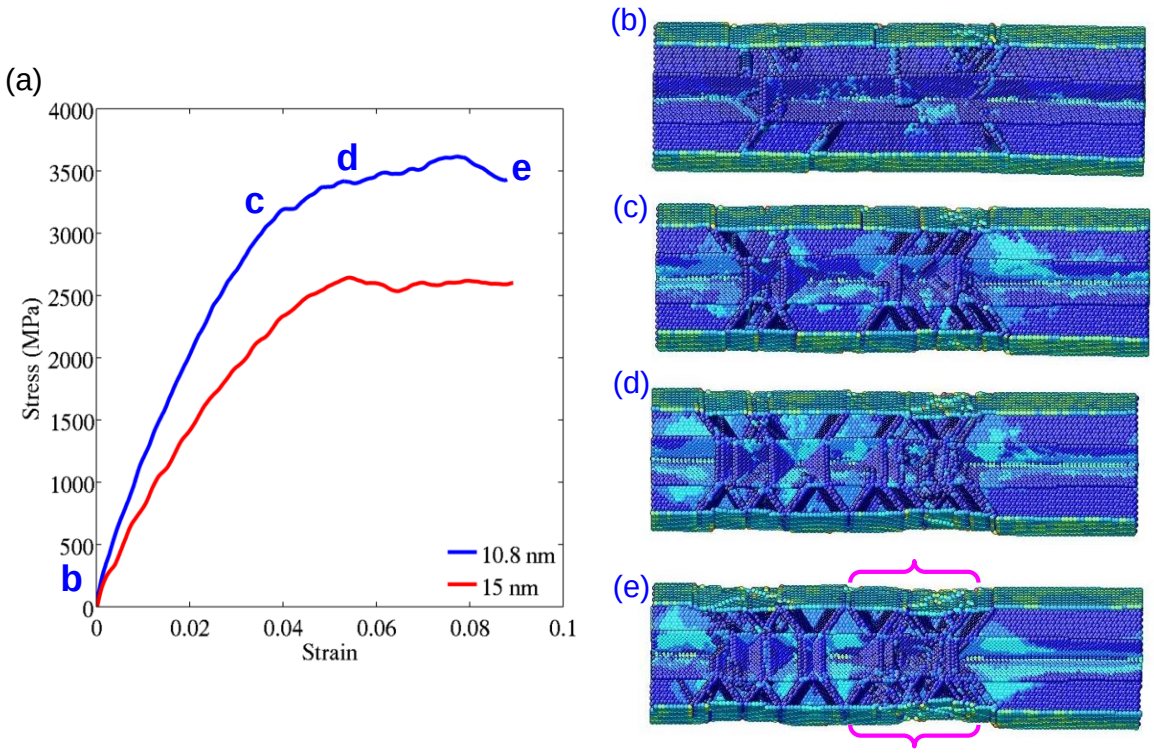

Fig. 5.5 Size-effected hardening behavior. (a) Stress-strain curves for the tensile loading of 'defective' Ag NWs of 10.8 nm and 15nm diameter, respectively. (b-d) Atomistic configurations of the 10.8 nm diameter NW at various strain levels as marked in Fig. 5.5(a).

Significant hardening in 'defective' AgNWs contrasts with the negligible hardening in the pristine five-fold twinned AgNWs in Fig. 5.4(a), thus demonstrating the important effect of statistical variation of source strengths of surface dislocations. In addition, our MD simulations also show very limited hardening in pre-strained single-crystalline AgNWs with pre-existing defects (see Fig. 5.6 below); in this case the nucleated dislocations are easily annihilated at the surface due to the lack of stable hardening obstacles. This comparison confirms the unique role of the vertical twin boundaries in the macroscopic hardening of the five-fold twinned AgNW, otherwise not exhibited by its single-crystalline counterpart.

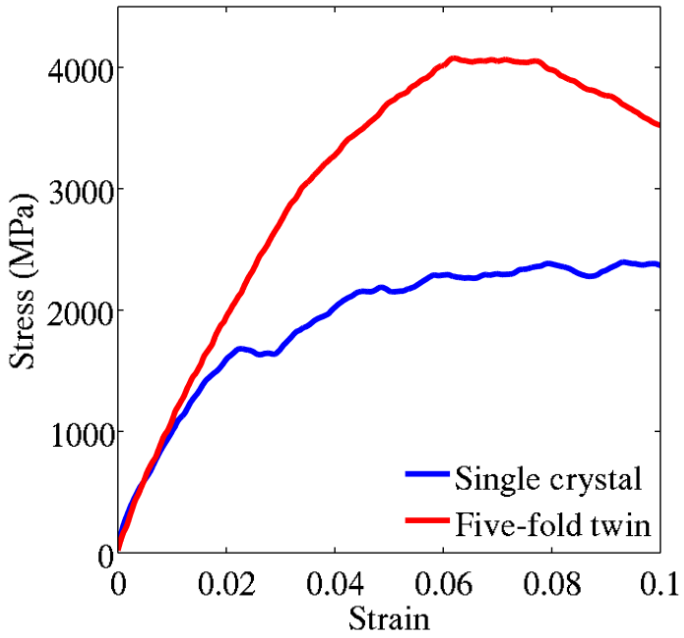

Fig. 5.6 Stress-strain curves. 'Defective', single crystalline [111] AgNW of 6.4 nm diameter, compared with a 'defective' five-fold twinned AgNW of 6.4 nm diameter.

To further understand the atomistic mechanisms underlying the macroscopic hardening in 'defective' five-fold twinned AgNWs, Fig. 5.5(b-d) show the [001] side sectional view of the 10.8 nm diameter AgNW at various strain levels, as marked in Fig. 5.5(a). Clearly, the zero stress state (Fig. 5.5(b)) contains pre-existing defects on the surface and within the nanowire, unlike the pristine five-fold twinned AgNW in Fig. 5.4(b). The initial non-linear stress-strain response is primarily governed by dislocation nucleation at the surface sources with low activation stress; Fig. 5.5(c) shows the surface-nucleated dislocations inside the deformed AgNW. However, the rate of surface nucleation and the resultant rate of stress relaxation are still relatively low. Moreover, the nucleated dislocations are mostly blocked by TBs, resulting in the back stress to resist against the continued operation of surface dislocation sources. As a result, the pronounced strain hardening ensues. When the tensile load increases to around point **d**, the rate of surface dislocation nucleation becomes high and the TB-obstructed

dislocations can often cross-slip into adjacent twin variants (Fig. 5.5(d)), so that the hardening rate (i.e., the slope of the stress-strain curve) is drastically reduced. At point **e** the dislocation activity starts to be confined into a narrow portion of the AgNW that subsequently leads to necking and ductile failure, as marked in Fig. 5.5(e).

The simulated stress-strain curves in Fig. 5.5(a) also capture the size/diameter dependent strength and hardening in five-fold twinned AgNWs, consistent with the experimental results in Fig. 5.2(c). Namely, thinner AgNWs achieve higher strength and more hardening that leads to higher ductility. Since TBs in the five-fold twinned AgNW play a similar role of obstructing dislocations as grain boundaries in bulk polycrystalline metals, the size-dependent strength in AgNWs can be attributed to the characteristic smaller-is-stronger size effect in the nanoscale. Specifically, as the diameter of the AgNW decreases, the effective distance between the surface dislocation source and the TB decreases. Such size reduction can lead to strong interactions between the TBs and surface dislocation sources, which are facilitated by the back stresses generated by the TB-obstructed dislocations, as discussed earlier. Hence, the higher strength in the smaller AgNW can be attributed to the relatively high stresses required to sustain the operation of surface dislocation sources, which is also responsible for the high hardening rate in the smaller AgNW. The high hardening rate can delay the onset of necking, thereby promoting the tensile ductility [29], which is consistent with both the experimental and MD results.

5.3.3 Necking and fracture

The final stage of tensile deformation of five-fold twinned AgNWs involved the onset and growth of necks. Such localized deformation eventually concentrated to one neck, leading to the fracture of the AgNW. Fig. 5.7 shows the necking behavior of two AgNWs with the respective initial diameters of 6.4 nm and 10.8 nm, close to their failure point. Both AgNWs are 34.7 nm long. Interestingly, the smaller wire in Fig. 5.7(a) exhibits several local necks along its length, while the larger wire in Fig. 5.7(c-d) exhibits only a single neck. The development of multiple necks in the smaller wire indicates that the growth of the neck can become difficult owing to the local hardening induced by the TBs. Consequently, the plastic deformation tends to be delocalized, resulting in multiple necks. Such multiple-necking mode in five-fold twinned AgNWs has been observed by Filleter *et al.* [148] in experiments. They measured the number and the length of the necks (which they termed as 'plastic zones') as a function of the AgNW diameter and found that the number of necks decreased and the length of the neck increased with nanowire diameter. Our MD results lend a direct proof for the size-dependent multiple necking behavior.

As mentioned earlier, the AgNW failed by necking at one of the necks in both the experiment and MD. Fig. 5.7(d) shows the post-mortem TEM image of the fracture surface. The rounded fracture surface is characteristic of the ductile rupture resulting from the dislocation shear induced thinning of the AgNW.

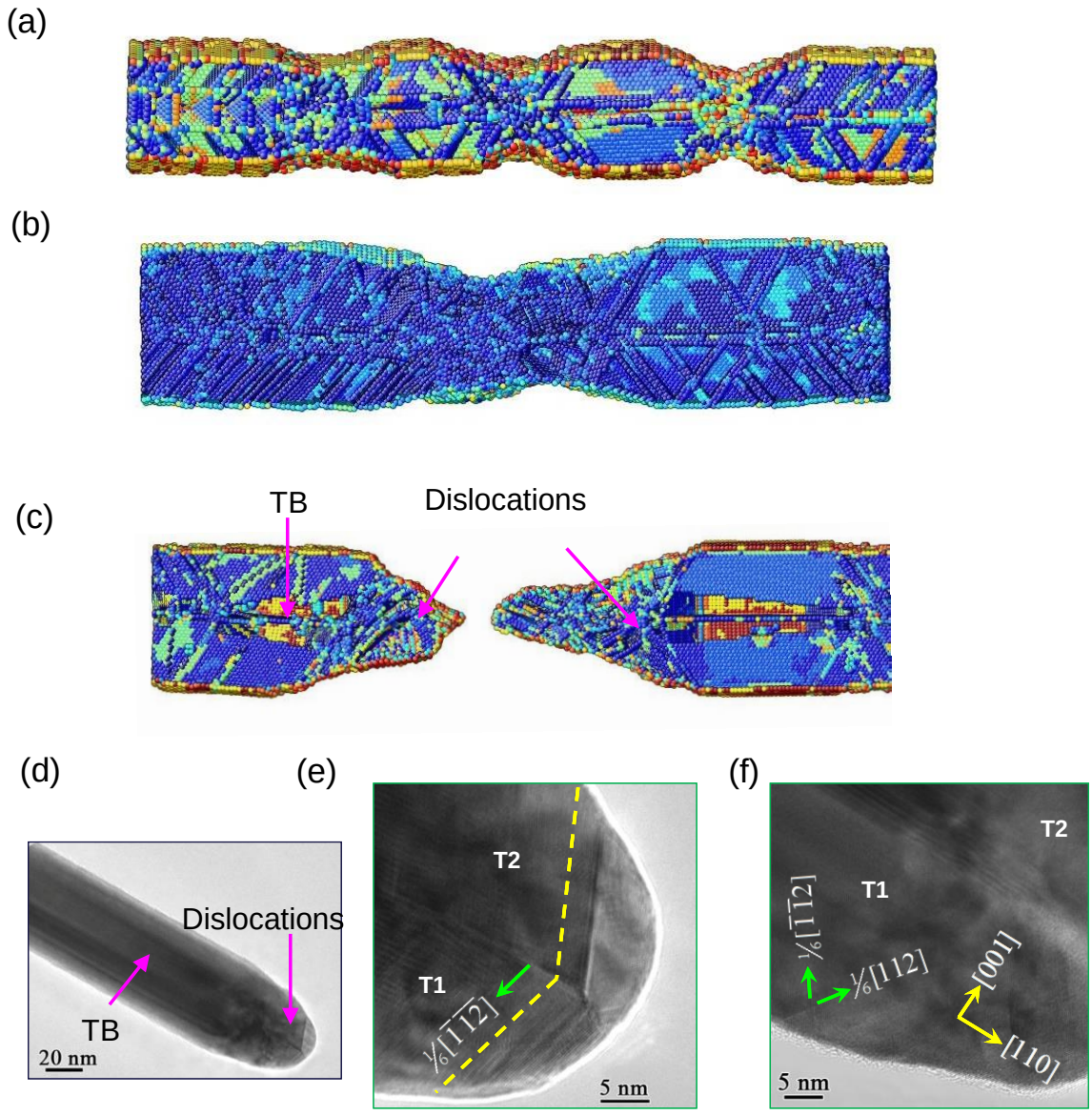

Fig. 5.7 Deformation via multiple necking and ductile failure. (a) 6.4 nm diameter NW. (b) 10.8 nm diameter NW. (c) TEM image of the forest dislocations seen at the failure surface. (d) MD image of the surface showing the forest dislocations. (e) TEM image showing the cross slip of the Shockley partial across the TB. (f) TEM image showing dislocation activity in the two equivalent $[110]\{111\}$ slip systems.

This is in contrast to the flat brittle-like fracture surface reported by Filleter *et al.* [148] Fig. 5.7(e) shows that a high density of dislocations can be seen near the fracture surface, while the portions of the nanowire away from the fracture surface have a lower dislocation density. This is consistent with our MD result in Fig. 5.7(c). High-resolution

TEM imaging of the failure surface also revealed direct evidence for the cross-slip of the Shockley partials at the TB (Fig. 5.7(e)), as observed in our MD simulations (Fig. 5.4(b-d)). Fig. 5.7(f) shows the slip activity in the two equivalent $[110]\{111\}$ slip systems, as revealed by MD in Fig. 5.4(e-f). These results demonstrate the direct correlation between our experimental and MD results.

5.3.4 Role of pre-existing defects

Recall that our MD results in Fig. 5.5(a) depicting hardening were based on the simulations of 'defective' five-fold twinned AgNWs, while the MD results in Fig. 5.4(a) shows that 'pristine' AgNWs do not exhibit hardening. Such a difference indicates that plastic deformation in AgNW is strongly dependent on the density of pre-existing defects. The critical role of pre-existing defects on the plasticity of nanostructures have previously been underscored in the studies of deformation of pre-strained Au nanopillars [157] , single-crystalline Au nanowhiskers [140] and Cu nanowires [136]. Essentially, the strain hardening behavior in the deformation experiment at a fixed loading rate is controlled by the interplay between the elastic strain rate (tends to increase the stress) and the plastic strain rate (tends to lower the stress), the latter of which is dictated by the dislocation nucleation rate in small-volume materials.

In order to understand the hardening behavior of the AgNW as a function of the density of the pre-existing defects, we simulated three samples (diameter of 10.8 nm) with different initial pre-existing defect densities, as shown in Fig. 5.8. The desired defect densities ρ were achieved by varying the strain level at which the nanowire was unloaded. The tensile stress-strain curves for these three AgNWs are compared in Fig.

5.8(a), with the corresponding [100] side sectional views of the initial states shown in Fig. 5.8(b-d). The stress-strain curves show that the AgNW with the smaller defect density (Fig. 5.8(b)) hardens more and achieves higher ultimate tensile strength than the other two AgNWs with higher defect densities (Fig. 5.8(c & d)). The AgNW with the least defect density produces the least amount of surface dislocations to plastically relax the system. As a result, the stress in this AgNW is the largest, when the same tensile strain is attained in three AgNWs.

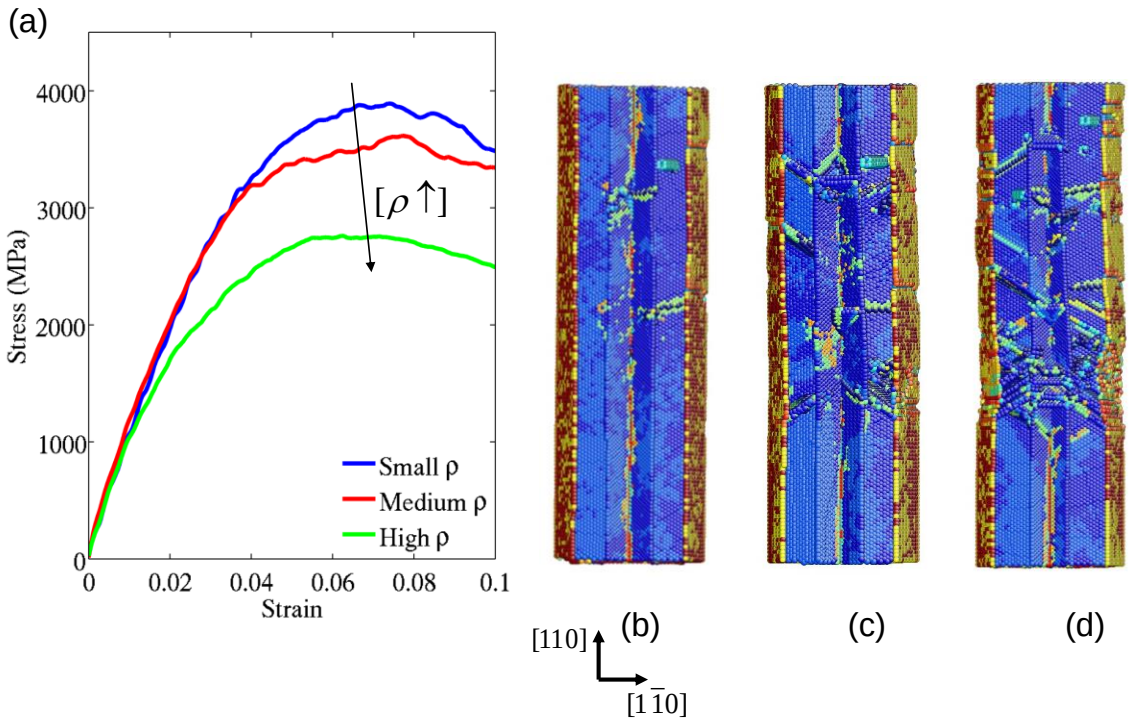

Fig. 5.8 Effect of pre-existing defects. (a) Stress-strain curves for three nanowire specimens of small, medium and high defect densities. (b-d) [100]side sectional views of the three specimens, 'small ρ', 'medium ρ' and 'high ρ', respectively, showing their pre-existing defects .

This result underscores the critical role of pre-existing defect density in influencing the hardening behavior and the ultimate tensile strength of the five-fold twinned AgNW. Finally, we note that because of the applied high rate in MD (~ 10^7 s^{-1} to 10^9 s^{-1}) the

defect density in our simulated 'defective' AgNW has to be high enough to generate a large number of dislocations to plastically relax the stress, so as to avoid the elastic overshooting in the 'pristine' AgNW. However, the required pre-existing defect density can be much lower in our laboratory experiments at low strain rates (~ 10^{-3}/s).

5.4 Conclusions

We have studied the unique strain hardening behavior of five-fold twinned AgNWs using a combined experimental-computational approach. Both our experiments and MD stimulations showed the strain hardening in five-fold twinned AgNWs, not exhibited by single-crystalline nanowires or other nanostructures. Smaller wires hardened significantly and achieved higher ultimate tensile strength than the larger ones. Such a hardening response and size effect were shown to be caused by the effective obstruction of surface nucleated dislocations by twin boundaries. Our MD simulations further revealed the important role of the statistical variation of source strengths of dislocations in the confined volume of nanostructures. Overall, the work in this chapter reveals the mechanistic underpinnings of strain hardening in metallic nanostructures by coherent twin boundaries and points to possible routes of enhancing the tensile ductility by engineering the internal interfaces and defects. The knowledge gained can be applied to further study the interactions of twin boundaries with irradiation-induced point and line defects.

CHAPTER 6

CONCLUSIONS

This thesis presents the atomistic modeling and atomistically informed coarse-grained modeling of irradiation damage in metals. We began our work by developing an atomistically informed crystal plasticity modeling framework that can predict macroscopic mechanical behavior by taking into account the atomistic level physics of deformation. To this end we conducted molecular dynamics simulations to explore the rate limiting plasticity mechanism of screw dislocation motion. Then we conducted 3D nudged elastic band calculations to determine the kinetics of dislocation motion and obtain material parameters that is informed into a coarse-grained crystal plasticity model. Tensile test simulations were performed using the crystal plasticity model within a finite element framework and the temperature and rate dependence of the flow stress was determined and compared with the experimental results from literature, so as to demonstrate the efficacy of our model. Secondly we investigated the plasticity mechanisms in irradiated metals. Towards that, we studied the interaction between screw dislocation and self interstitial atoms that are typically found in irradiated atmospheres. We discovered that the self interstitial atoms could be absorbed into the screw dislocation core and modified its core structure to form a specific structure called the three-kink dislocation that had kinetics different from the normal screw dislocation. By comparing the kinetics of normal screw dislocation and the 3-kink dislocation we were able to obtain a new understanding on the experimentally observed irradiation induced hardening and softening phenomena. Our atomistic modeling and atomistically informed crystal plasticity modeling framework provide significant potentials for studying a wealth of

thermally activated crystal plasticity mechanisms that critically govern the material behavior in various practical situations.

In this thesis, we also studied the formation of stacking fault tetrahedra in gold nanocrystals and specifically in non-irradiated conditions. We discover this deformation induced formation of SFT with the help of high resolution *in situ* TEM experiments and molecular dynamics simulations. We were able to account for the entire dynamics of the formation, evolution and destruction of the SFT, strongly controlled by the surface nucleation and interaction of dislocations inside the gold nanocrystal. This finding provided novel scientific reasons for the formation and evolution of staking fault tetrahedron in non-irradiated conditions, which otherwise has been considered to be purely an irradiation induced defect. Lastly we studied the role of nanoscale interfaces in plasticity toward understanding their resistance to irradiation damage. To this end we studied stress-strain and hardening behavior of silver nanowires with a specific five-fold twinned internal microstructure. We conducted molecular dynamics simulations on five-fold twinned silver nanowires of various sizes and defect structures, so as to evaluate their effects on the hardening behavior of the same. With the help of tensile testing within an SEM, we were able to compare our simulations results with the experimental results for the size effected hardening of the silver nanowires. These atomistic studies in close collaboration with experimental works, holds practical potential for predicting the macroscopic mechanical behavior of materials under irradiated conditions.

Overall the atomistic and crystal plasticity studies in this thesis provide novel mechanistic insights into the plasticity of metals under unirradiated and irradiated

conditions, that holds promising potential for developing irradiation resistant materials for ensuring safety of future nuclear reactors.

REFERENCES

[1] de la Rubia TD, Zbib HM, Khraishi TA, Wirth BD, Victoria M, Caturla MJ. Multiscale modelling of plastic flow localization in irradiated materials. NATURE 2000;406:871-4.

[2] Odette GR, Lucas GE. Embrittlement of nuclear reactor pressure vessels. JOM-J Miner Met Mater Soc 2001;53:18-22.

[3] Lee HJ, Wirth BD. Molecular dynamics simulation of dislocation-void interactions in BCC Mo. J Nucl Mater 2009;386-88:115-8.

[4] Ghoniem NM, Busso EP, Kioussis N, Huang HC. Multiscale modelling of nanomechanics and micromechanics: an overview. Philosophical Magazine 2003;83:3475-528.

[5] Wirth BD, Bulatov V, de la Rubia TD. Atomistic simulation of stacking fault tetrahedra formation in Cu. J Nucl Mater 2000;283:773-7.

[6] Zinkle SJ, Matsukawa Y. Observation and analysis of defect cluster production and interactions with dislocations. J Nucl Mater 2004;329:88-96.

[7] Zinkle SJ, Maziasz PJ, Stoller RE. DOSE DEPENDENCE OF THE MICROSTRUCTURAL EVOLUTION IN NEUTRON-IRRADIATED AUSTENITIC STAINLESS-STEEL. J Nucl Mater 1993;206:266-86.

[8] Luft A. MICROSTRUCTURAL PROCESSES OF PLASTIC INSTABILITIES IN STRENGTHENED METALS. Prog Mater Sci 1991;35:97-204.

[9] Bullough R, Willis JR. STRESS-INDUCED POINT DEFECT-DISLOCATION INTERACTION AND ITS RELEVANCE TO IRRADIATION CREEP. Philosophical Magazine 1975;31:855-61.

[10] Bullough R. Radiation damage and point defects. Philosophical Magazine 2013:1-12.

[11] Vitek V. Non-planar Dislocation Cores: A Ubiquitous Phenomenon Affecting Mechanical Properties of Crystalline Materials. In: Hirth JP, editor. Dislocations in Solids. Amsterdam: North-Holland; 2008. p. 441-514.

[12] Odette GR, Wirth BD, Bacon DJ, Ghoniem NM. Multiscale-multiphysics modeling of radiation-damaged materials: Ebrittlement of pressure-vessel steels. MRS Bull 2001;26:176-81.

[13] Vineyard GH. Frequency Factors and Isotope Effects in Solid State Rate Processes. Journal of Physics and Chemistry of Solids 1957;3:121-7.

[14] Zhu T, Li J, Yip S. Atomistic reaction pathway sampling: The nudged elastic band method and nanomechanics applications. In: Espinosa HD, Bao G, editors. Nano and Cell Mechanics: John Wiley & Sons; 2013. p. 313-38.

[15] Zhu T, Li J, Samanta A, Leach A, Gall K. Temperature and strain-rate dependence of surface dislocation nucleation. Phys Rev Lett 2008;100.

[16] Asenjo A, Jaafar M, Carrasco E, Rojo JM. Dislocation mechanisms in the first stage of plasticity of nanoindented Au(111) surfaces. Physical Review B 2006;73:075431.

[17] Argon AS. Strengthening mechanisms in crystal plasticity. New York: Oxford Unversity Press Inc.; 2008.

[18] Weinberger CR, Boyce BL, Battaile CC. Slip planes in bcc transition metals. International Materials Reviews 2013;58:296-314.

[19] Seeger A. On the Theory of the Low-Temperature Internal Friction Peak Observed in Metals. Philos Mag 1956;1:651-62.

[20] Chaussidon J, Fivel M, Rodney D. The glide of screw dislocations in bcc Fe: Atomistic static and dynamic simulations. Acta Mater 2006;54:3407-16.

[21] Groger R, Bailey AG, Vitek V. Multiscale modeling of plastic deformation of molybdenum and tungsten: I. Atomistic studies of the core structure and glide of 1/2 < 111 > screw dislocations at 0 K. Acta Mater 2008;56:5401-11.

[22] Groger R, Racherla V, Bassani JL, Vitek V. Multiscale modeling of plastic deformation of molybdenum and tungsten: II. Yield criterion for single crystals based on atomistic studies of glide of 1/2 < 111 > screw dislocations. Acta Mater 2008;56:5412-25.

[23] Koester A, Ma AX, Hartmaier A. Atomistically informed crystal plasticity model for body-centered cubic iron. Acta Mater 2012;60:3894-901.

[24] Chen ZM, Mrovec M, Gumbsch P. Atomistic aspects of 1/2 < 1 1 1 > screw dislocation behavior in alpha-iron and the derivation of microscopic yield criterion. Modelling and Simulation in Materials Science and Engineering 2013;21:055023.

[25] Bassani JL, Ito K, Vitek V. Complex macroscopic plastic flow arising from non-planar dislocation core structures. Materials Science and Engineering A 2001;319:97-101.

[26] Gilbert MR, Queyreau S, Marian J. Stress and temperature dependence of screw dislocation mobility in alpha-Fe by molecular dynamics. Physical Review B 2011;84:174103.

[27] Domain C, Monnet G. Simulation of screw dislocation motion in iron by molecular dynamics simulations. Physical Review Letters 2005;95:215506.

[28] Jonsson H, G. Mills, K. W. Jacobsen. Nudged elastic band method for finding minimum energy paths of transitions In B J Berne, G Ciccotti, and D F Coker, editors, Classical and Quantum Dynamics in Condensed Phase Simulations 1998: 385–404.

[29] Zhu T, Li J. Ultra-strength Materials. Progress in Materials Science 2010;55:710-57.

[30] Groger R, Vitek V. Multiscale modeling of plastic deformation of molybdenum and tungsten. III. Effects of temperature and plastic strain rate. Acta Mater 2008;56:5426-39.

[31] Ngan AHW, Wen M. Atomistic simulation of energetics of motion of screw dislocations in bcc Fe at finite temperatures. Computational Materials Science 2002;23:139-45.

[32] Gordon PA, Neeraj T, Li Y, Li J. Screw dislocation mobility in BCC metals: the role of the compact core on double-kink nucleation. Modelling and Simulation in Materials Science and Engineering 2010;18:085008.

[33] Proville L, Rodney D, Marinica MC. Quantum effect on thermally activated glide of dislocations. Nature Materials 2012;11:845-9.

[34] Mendelev MI, Han S, Srolovitz DJ, Ackland GJ, Sun DY, Asta M. Development of new interatomic potentials appropriate for crystalline and liquid iron. Philos Mag 2003;83:3977-94.

[35] Gordon PA, Neeraj T, Mendelev MI. Screw dislocation mobility in BCC Metals: a refined potential description for alpha-Fe. Philos Mag 2011;91:3931-45.

[36] Ventelon L, Willaime F. Core structure and Peierls potential of screw dislocations in alpha-Fe from first principles: cluster versus dipole approaches. Journal of Computer-Aided Materials Design 2007;14:85-94.

[37] Weinberger CR, Tucker GJ, Foiles SM. Peierls potential of screw dislocations in bcc transition metals: Predictions from density functional theory. Physical Review B 2013;87:054114.

[38] Yalcinkaya T, Brekelmans WAM, Geers MGD. BCC single crystal plasticity modeling and its experimental identification. Modelling and Simulation in Materials Science and Engineering 2008;16:085007.

[39] Weinberger CR, Battaile CC, Buchheit TE, Holm EA. Incorporating atomistic data of lattice friction into BCC crystal plasticity models. International Journal Of Plasticity 2012;37:16-30.

[40] Tang M, Kubin LP, Canova GR. Dislocation mobility and the mechanical response of BCC single crystals: A mesoscopic approach. Acta Mater 1998;46:3221-35.

[41] Patra A, McDowell DL. Crystal plasticity-based constitutive modelling of irradiated bcc structures. Philos Mag 2012;92:861-87.

[42] Kocks UF, Argon AS, Ashby MF. Thermodynamics And Kinetics Of Slip. Progress In Materials Science 1975;19:1-281.

[43] Keh AS. Work hardening and deformation sub-structure in iron single crystals deformed in tension at 298 degrees K. Philos Mag 1965;12:9-30.

[44] Kuramoto E, Aono Y, Kitajima K. Thermally Activated Slip Deformation of High-Purity Iron Single-Crystals between 4.2-K and 300-K. Scripta Metallurgica 1979;13:1039-42.

[45] Zhu T, Li J, Yip S. Atomistic study of dislocation loop emission from a crack tip. Physical Review Letters 2004;93:025503.

[46] Zhu T, Li J, Lin X, Yip S. Stress-dependent molecular pathways of silica-water reaction. Journal of the Mechanics and Physics of Solids 2005;53:1597-623.

[47] Zhu T, Li J, Samanta A, Kim HG, Suresh S. Interfacial plasticity governs strain rate sensitivity and ductility in nanostructured metals. Proceedings of the National Academy of Sciences of the USA 2007;104:3031-6.

[48] Zhu T, Li J, Samanta A, Leach A, Gall K. Temperature and strain-rate dependence of surface dislocation nucleation. Physical Review Letters 2008;100:025502.

[49] Ackland GJ, Bacon DJ, Calder AF, Harry T. Computer simulation of point defect properties in dilute Fe-Cu alloy using a many-body interatomic potential. Philos Mag A-Phys Condens Matter Struct Defect Mech Prop 1997;75:713-32.

[50] Johnson RA, Oh DJ. Analytic Embedded Atom Method Model for Bcc Metals. Journal of Materials Research 1989;4:1195-201.

[51] Li J. AtomEye: an efficient atomistic configuration viewer. Modelling and Simulation in Materials Science and Engineering 2003;11:173-7.

[52] Plimpton S. Fast Parallel Algorithms For Short-Range Molecular-Dynamics. Journal Of Computational Physics 1995;117:1-19.

[53] Henkelman G, Uberuaga BP, Jonsson H. A climbing image nudged elastic band method for finding saddle points and minimum energy paths. Journal of Chemical Physics 2000;113:9901-4.

[54] Asaro RJ, Needleman A. Overview no. 42 Texture development and strain hardening in rate dependent polycrystals. Acta Metallurgica 1985;33:923-53.

[55] Kalidindi SR, Bronkhorst CA, Anand L. Crystallographic texture evolution in bulk deformation processing of fcc metals. Journal of the Mechanics and Physics of Solids 1992;40:537-69.

[56] Kothari M, Anand L. Elasto-viscoplastic constitutive equations for polycrystalline metals: Applications to tantalum. Journal of the Mechanics and Physics of Solids 1998;46:51-83.

[57] Seeger A. Why anomalous slip in body-centred cubic metals? Materials Science And Engineering A 2001;319:254-60.

[58] Vitek V. Core structure of screw dislocations in body-centred cubic metals: relation to symmetry and interatomic bonding. Philos Mag 2004;84:415-28.

[59] Caillard D. Kinetics of dislocations in pure Fe. Part II. In situ straining experiments at low temperature. Acta Mater 2010;58:3504-15.

[60] Conrad H. Effect of Temperature on Yield and Flow Stress of Bcc Metals. Philos Mag 1960;5:745-51.

[61] Hill TL. An Introduction to Statistical Thermodynamics. New York., Dover. 1986.

[62] Wei Q, Cheng S, Ramesh KT, Ma E. Effect of nanocrystalline and ultrafine grain sizes on the strain rate sensitivity and activation volume: fcc versus bcc metals. Materials Science and Engineering a-Structural Materials Properties Microstructure and Processing 2004;381:71-9.

[63] Brunner D, Diehl J. Strain-Rate and Temperature-Dependence of the Tensile Flow-Stress of High-Purity Alpha-Iron above 250-K (Regime I) Studied by Means of Stress-Relaxation Tests. Phys Status Solidi A-Appl Res 1991;124:155-70.

[64] Suzuki H. Motion of dislocations in body-centered cubic crystals. Dislocation Dynamics, 1968;A. R. Rosenfeld, G. T. Hahn, A. L. Bement, and R. I. Jaffee, p. 679. New York: McGraw-Hill.

[65] Groger R, Vitek V. Explanation of the discrepancy between the measured and atomistically calculated yield stresses in body-centred cubic metals. Philosophical Magazine Letters 2007;87:113-20.

[66] Kang K, Bulatov VV, Cai W. Singular orientations and faceted motion of dislocations in body-centered cubic crystals. Proceedings of the National Academy of Sciences of the United States of America 2012;109:15174-8.

[67] Bulatov VV, Yip S, Argon AS. Atomic Modes of Dislocation Mobility in Silicon. Philos Mag A-Phys Condens Matter Struct Defect Mech Prop 1995;72:453-96.

[68] Dorn JE, Rajnak S. Nucleation of Kink Pairs + Peierls Mechanism of Plastic Deformation. Transactions of the Metallurgical Society of Aime 1964;230:1052-&.

[69] Caillard D. An in situ study of hardening and softening of iron by carbon interstitials. Acta Mater 2011;59:4974-89.

[70] Hirth JP, Lothe J. Theory of Dislocations. Wiley, New York 1982.

[71] Okazaki K. Solid-solution hardening and softening in binary iron alloys. Journal of Materials Science 1996;31:1087-99.

[72] Sato A, Mifune T, Meshii M. IRRADIATION SOFTENING IN PURE IRON SINGLE-CRYSTALS. Phys Status Solidi A-Appl Res 1973;18:699-709.

[73] Caillard D. A TEM in situ study of alloying effects in iron. I-Solid solution softening caused by low concentrations of Ni, Si and Cr. Acta Mater 2013;61:2793-807.

[74] Caillard D. A TEM in situ study of alloying effects in iron. II-Solid solution hardening caused by high concentrations of Si and Cr. Acta Mater 2013;61:2808-27.

[75] Hayward E, Deo C, Uberuaga BP, Tome CN. The interaction of a screw dislocation with point defects in bcc iron. Philos Mag 2012;92:2759-78.

[76] Brunner D, Diehl J. The effect of atomic lattice defects on the softening phenomena of high-purity alpha-iron. Phys Status Solidi A-Appl Res 1997;160:355-72.

[77] Narayanan S, McDowell DL, Zhu T. Crystal plasticity model for BCC iron atomistically informed by kinetics of correlated kinkpair nucleation on screw dislocation. Journal of the Mechanics and Physics of Solids 2014;65:54-68.

[78] Marian J, Cai W, Bulatov VV. Dynamic transitions from smooth to rough to twinning in dislocation motion. Nature Materials 2004;3:158-63.

[79] Caillard D. Kinetics of dislocations in pure Fe. Part I. In situ straining experiments at room temperature. Acta Mater 2010;58:3493-503.

[80] Makii K, Tsutsumi T, Aono Y, Kuramoto E. UNDERSTANDING OF IRRADIATION SOFTENING IN ALPHA-IRON FROM THE VIEWPOINT OF THE DIRECT INTERACTION BETWEEN A SCREW DISLOCATION AND SELF INTERSTITIAL ATOMS UNDER STRESS. Mater Trans JIM 1989;30:505-15.

[81] Louchet F, Viguier B. Ordinary dislocations in gamma-TiAl: cusp unzipping, jog dragging and stress anomaly. Philos Mag A-Phys Condens Matter Struct Defect Mech Prop 2000;80:765-79.

[82] Takamura S, Kitajima K, Abe H, Okuda S. TEMPERATURE AND ORIENTATION DEPENDENCES OF IRRADIATION SOFTENING IN IRON SINGLE-CRYSTALS. Scripta Metallurgica 1977;11:597-602.

[83] Vanoni F, Groh P, Moser P. FAST-NEUTRON RADIATION SOFTENING AND RADIATION ANNEAL HARDENING IN IRON AT LOW-TEMPERATURE. Scripta Metallurgica 1972;6:777-&.

[84] Hirth JP, Lothe J. Theory of Dislocations. New York: Wiley; 1982.

[85] Lu K, Lu L, Suresh S. Strengthening Materials by Engineering Coherent Internal Boundaries at the Nanoscale. Science 2009;324:349-52.

[86] Kiritani M. Story of stacking fault tetrahedra. Materials Chemistry and Physics 1997;50:133-8.

[87] Silcox J, Hirsch PB. Direct observations of defects in quenched gold. Philosophical Magazine 1959;4:72-89.

[88] Clarebrough LM. Stacking-fault tetrahedra in annealed f.c.c. metals and alloys. Philosophical Magazine 1974;30:1295-312.

[89] Coene W, Bender H, Amelinckx S. High resolution structure imaging and image simulation of stacking fault tetrahedra in ion-implanted silicon. Philosophical Magazine A 1985;52:369-81.

[90] Loretto MH, Clarebrough LM, Segall RL. Stacking-fault tetrahedra in deformed face-centred cubic metals. Philosophical Magazine 1965;11:459-65.

[91] Loretto MH, Pavey A. The formation of intrinsic stacking-fault tetrahedra in deformed F.C.C. alloys. Philosophical Magazine 1968;17:553-9.

[92] Kojima S, Satoh Y, Taoka H, Ishida I, Yoshiie T, Kiritani M. Confirmation of vacancy-type stacking fault tetrahedra in quenched, deformed and irradiated face-centred cubic metals. Philosophical Magazine A 1989;59:519-32.

[93] Kiritani M, Yasunaga K, Matsukawa Y, Komatsu M. Plastic Deformation of Metal Thin Films without Involving Dislocations and Anomalous Production of Point Defects. Radiation Effects and Defects in Solids 2002;157:3-24.

[94] Kiritani M. Dislocation-free plastic deformation under high stress. Materials Science and Engineering: A 2003;350:1-7.

[95] Wirth BD, Bulatov V, Diaz de la Rubia T. Atomistic simulation of stacking fault tetrahedra formation in Cu. J Nucl Mater 2000;283-287, Part 2:773-7.

[96] Matsukawa Y, Osetsky YN, Stoller RE, Zinkle SJ. Destruction processes of large stacking fault tetrahedra induced by direct interaction with gliding dislocations. J Nucl Mater 2006;351:285-94.

[97] Martinez E, Marian J, Arsenlis A, Victoria M, Perlado JM. A dislocation dynamics study of the strength of stacking fault tetrahedra. Part I: interactions with screw dislocations. Philosophical Magazine 2008;88:809-40.

[98] Lee HJ, Wirth BD. Molecular dynamics simulation of the interaction between a mixed dislocation and a stacking fault tetrahedron. Philosophical Magazine 2009;89:821-41.

[99] Matsukawa Y, Osetsky YN, Stoller RE, Zinkle SJ. Mechanisms of stacking fault tetrahedra destruction by gliding dislocations in quenched gold. Philosophical Magazine 2008;88:581-97.

[100] Niewczas M, Hoagland RG. Molecular dynamics studies of the interaction of a/6 ⟨ 112⟩ Shockley dislocations with stacking fault tetrahedra in copper. Part I: Intersection of SFT by an isolated Shockley. Philosophical Magazine 2009;89:623-40.

[101] Szelestey P, Patriarca M, Kaski K. Computational study of a screw dislocation interacting with a stacking-fault tetrahedron. Modelling and Simulation in Materials Science and Engineering 2005;13:541.

[102] Robach JS, Robertson IM, Lee HJ, Wirth BD. Dynamic observations and atomistic simulations of dislocation–defect interactions in rapidly quenched copper and gold. Acta Mater 2006;54:1679-90.

[103] Matsukawa Y, Osetsky YN, Stoller RE, Zinkle SJ. The collapse of stacking-fault tetrahedra by interaction with gliding dislocations. Materials Science and Engineering: A 2005;400-401:366-9.

[104] Osetsky YN, Rodney D, Bacon DJ. Atomic-scale study of dislocation–stacking fault tetrahedron interactions. Part I: mechanisms. Philosophical Magazine 2006;86:2295-313.

[105] Uberuaga BP, Hoagland RG, Voter AF, Valone SM. Direct Transformation of Vacancy Voids to Stacking Fault Tetrahedra. Phys Rev Lett 2007;99:135501.

[106] Wang H, Xu DS, Yang R, Veyssière P. The formation of stacking fault tetrahedra in Al and Cu: I. Dipole annihilation and the nucleation stage. Acta Mater 2011;59:1-9.

[107] Wang H, Xu DS, Yang R, Veyssière P. The formation of stacking fault tetrahedra in Al and Cu: III. Growth by expanding ledges. Acta Mater 2011;59:19-29.

[108] Uchic MD, Dimiduk DM, Florando JN, Nix WD. Sample Dimensions Influence Strength and Crystal Plasticity. Science 2004;305:986-9.

[109] Zhu T, Li J. Ultra-strength materials. Progress in Materials Science 2010;55:710-57.

[110] Zhu T, Li J, Samanta A, Leach A, Gall K. Temperature and Strain-Rate Dependence of Surface Dislocation Nucleation. Physical Review Letters 2008;100:025502.

[111] Zheng H, Cao AJ, Weinberger CR, Huang JY, Du K, Wang JB, et al. Discrete plasticity in sub-10-nm-sized gold crystals. Nature Communications 2010;1:144.

[112] Wang J, Sansoz F, Huang J, Liu Y, Sun S, Zhang Z, et al. Near-ideal theoretical strength in gold nanowires containing angstrom scale twins. Nat Commun 2013;4:1742.

[113] Nix WD, Lee S-W. Micro-pillar plasticity controlled by dislocation nucleation at surfaces. Philosophical Magazine 2011;91:1084-96.

[114] Oh SH, Legros M, Kiener D, Dehm G. In situ observation of dislocation nucleation and escape in a submicrometre aluminium single crystal. Nat Mater 2009;8:95-100.

[115] Chrobak D, Tymiak N, Beaber A, Ugurlu O, Gerberich WW, Nowak R. Deconfinement leads to changes in the nanoscale plasticity of silicon. Nat Nano 2011;6:480-4.

[116] Wang C, Hu Y, Lieber CM, Sun S. Ultrathin Au Nanowires and Their Transport Properties. Journal of the American Chemical Society 2008;130:8902-3.

[117] Plimpton S. Fast Parallel Algorithms for Short-Range Molecular Dynamics. Journal of Computational Physics 1995;117:1-19.

[118] Grochola G, Russo SP, Snook IK. On fitting a gold embedded atom method potential using the force matching method. The Journal of Chemical Physics 2005;123:204719-7.

[119] Mishin Y, Mehl MJ, Papaconstantopoulos DA, Voter AF, Kress JD. Structural stability and lattice defects in copper: Ab initio, tight-binding, and embedded-atom calculations. Physical Review B 2001;63:224106.

[120] Matsukawa Y, Zinkle SJ. One-Dimensional Fast Migration of Vacancy Clusters in Metals. Science 2007;318:959-62.

[121] Arakawa K, Ono K, Isshiki M, Mimura K, Uchikoshi M, Mori H. Observation of the One-Dimensional Diffusion of Nanometer-Sized Dislocation Loops. Science 2007;318:956-9.

[122] Wirth BD. How Does Radiation Damage Materials? Science 2007;318:923-4.

[123] Kuhlmann-Wilsdorf D. The growth and annealing of stacking fault tetrahedra. Acta Metallurgica 1965;13:257-70.

[124] Lu Y, Huang JY, Wang C, Sun S, Lou J. Cold welding of ultrathin gold nanowires. Nat Nano 2010;5:218-24.

[125] Mordehai D, Rabkin E, Srolovitz DJ. Pseudoelastic Deformation during Nanoscale Adhesive Contact Formation. Phys Rev Lett 2011;107:096101.

[126] Egerton RF, Li P, Malac M. Radiation damage in the TEM and SEM. Micron 2004;35:399-409.

[127] Jose-Yacaman M, Gutierrez-Wing C, Miki M, Yang D-Q, Piyakis K, Sacher E. Surface diffusion and coalescence of mobile metal nanoparticles. The Journal of Physical Chemistry B 2005;109:9703-11.

[128] Deng C, Sansoz F. Near-Ideal Strength in Gold Nanowires Achieved through Microstructural Design. ACS Nano 2009;3:3001-8.

[129] Demkowicz MJ, Hoagland RG, Hirth JP. Interface Structure and Radiation Damage Resistance in Cu-Nb Multilayer Nanocomposites. Phys Rev Lett 2008;100:136102.

[130] Bi Z, Uberuaga BP, Vernon LJ, Aguiar JA, Fu E, Zheng S, et al. Role of the interface on radiation damage in the SrTiO3/LaAlO3 heterostructure under Ne2+ ion irradiation. Journal of Applied Physics 2014;115:-.

[131] Brenner SS. TENSILE STRENGTH OF WHISKERS. Journal of Applied Physics 1956;27:1484-91.

[132] Greer JR, Nix WD. Nanoscale gold pillars strengthened through dislocation starvation. Physical Review B 2006;73:245410.

[133] Greer JR, De Hosson JTM. Plasticity in small-sized metallic systems: Intrinsic versus extrinsic size effect. Prog Mater Sci 2011;56:654-724.

[134] Park HS, Gall K, Zimmerman JA. Deformation of FCC nanowires by twinning and slip. Journal of the Mechanics and Physics of Solids 2006;54:1862-81.

[135] Kiener D, Minor AM. Source Truncation and Exhaustion: Insights from Quantitative in situ TEM Tensile Testing. Nano Letters 2011;11:3816-20.

[136] Peng C, Zhan Y, Lou J. Size-dependent fracture mode transition in copper nanowires. Small 2012;8:1889-94.

[137] Peng C, Zhong Y, Lu Y, Narayanan S, Zhu T, Lou J. Strain rate dependent mechanical properties in single crystal nickel nanowires. Applied Physics Letters 2013;102.

[138] Liang WW, Zhou M, Ke FJ. Shape memory effect in Cu nanowires. Nano Letters 2005;5:2039-43.

[139] Seo JH, Yoo Y, Park NY, Yoon SW, Lee H, Han S, et al. Superplastic Deformation of Defect-Free Au Nanowires via Coherent Twin Propagation. Nano Letters 2011;11:3499-502.

[140] Sedlmayr A, Bitzek E, Gianola DS, Richter G, Moenig R, Kraft O. Existence of two twinning-mediated plastic deformation modes in Au nanowhiskers. Acta Mater 2012;60:3985-93.

[141] Wang L, Liu P, Guan P, Yang M, Sun J, Cheng Y, et al. In situ atomic-scale observation of continuous and reversible lattice deformation beyond the elastic limit. Nat Commun 2013;4:2413.

[142] Zhu T, Gao HJ. Plastic deformation mechanism in nanotwinned metals: An insight from molecular dynamics and mechanistic modeling. Scripta Materialia 2012;66:843-8.

[143] Deng C, Sansoz F. Enabling Ultrahigh Plastic Flow and Work Hardening in Twinned Gold Nanowires. Nano Letters 2009;9:1517-22.

[144] Wang J, Sansoz F, Huang J, Liu Y, Sun S, Zhang Z, et al. Near-ideal theoretical strength in gold nanowires containing angstrom scale twins. Nature Communications 2013;4:1742.

[145] Lu L, Chen X, Huang X, Lu K. Revealing the Maximum Strength in Nanotwinned Copper. Science 2009;323:607-10.

[146] Jang DC, Li XY, Gao HJ, Greer JR. Deformation mechanisms in nanotwinned metal nanopillars. Nature Nanotechnology 2012;7:594-601.

[147] Zhu Y, Qin QQ, Xu F, Fan FR, Ding Y, Zhang T, et al. Size effects on elasticity, yielding, and fracture of silver nanowires: In situ experiments. Physical Review B 2012;85:045443.

[148] Filleter T, Ryu S, Kang K, Yin J, Bernal RA, Sohn K, et al. Nucleation-Controlled Distributed Plasticity in Penta-twinned Silver Nanowires. Small 2012;8:2986-93.

[149] Cao AJ, Wei YG. Atomistic simulations of the mechanical behavior of fivefold twinned nanowires. Physical Review B 2006;74:214108.

[150] Leach AM, McDowell M, Gall K. Deformation of top-down and bottom-up silver nanowires. Advanced Functional Materials 2007;17:43-53.

[151] Monk J, Hoyt JJ, Farkas D. Metastability of multitwinned Ag nanorods: Molecular dynamics study. Physical Review B 2008;78:024112.

[152] Lucas M, Leach AM, McDowell MT, Hunyadi SE, Gall K, Murphy CJ, et al. Plastic deformation of pentagonal silver nanowires: Comparison between AFM nanoindentation and atomistic simulations. Physical Review B 2008;77:245420.

[153] Zhu Y, Xu F, Qin QQ, Fung WY, Lu W. Mechanical Properties of Vapor-Liquid-Solid Synthesized Silicon Nanowires. Nano Letters 2009;9:3934-9.

[154] Williams PL, Mishin Y, Hamilton JC. An embedded-atom potential for the Cu-Ag system. Modelling and Simulation in Materials Science and Engineering 2006;14:817-33.

[155] Sun YG, Gates B, Mayers B, Xia YN. Crystalline silver nanowires by soft solution processing. Nano Letters 2002;2:165-8.

[156] Wiley B, Sun YG, Xia YN. Synthesis of silver nanostructures with controlled shapes and properties. Accounts of Chemical Research 2007;40:1067-76.

[157] Lee S-W, Han SM, Nix WD. Uniaxial compression of fcc Au nanopillars on an MgO substrate: The effects of prestraining and annealing. Acta Mater 2009;57:4404-15.